

DISSERTATION

STEADY STATE HOPF MODE INTERACTION IN ANISOTROPIC SYSTEMS

Submitted by

Jennifer Maple

Department of Mathematics

In partial fulfillment of the requirements

For the Degree of Doctor of Philosophy

Colorado State University

Fort Collins, Colorado

Summer 2013

Doctoral Committee:

Advisor: Iuliana Oprea

Co-Advisor: Gerhard Dangelmayr

Patrick Shipman

Steven Fassnacht

ABSTRACT

STEADY STATE HOPF MODE INTERACTION IN ANISOTROPIC SYSTEMS

A paradigm example of pattern formation in anisotropic extended systems is the electroconvection of nematic liquid crystals, due to its easily accessible control parameters and the variety of patterns near onset. Some of the patterns observed are oblique and normal rolls which can be stationary or traveling, and more complex structures such as worms, defects and spatiotemporal complexity, including spatiotemporal intermittency and chaos, can occur, see e.g., Dennin et al, *Science* 272, 1996. During electroconvection experiments on the nematic liquid crystal mixture Phase V, a mode interaction between oblique stationary rolls and normal traveling rolls has been observed by Acharya et al, *Int. J. Mol. Sci.* 12, 448, 2011; a system of four globally coupled Ginzburg Landau equations for slowly varying spatiotemporal amplitudes of ideal roll patterns governing the dynamics of anisotropic systems close to the experimentally observed codimension-two point has been set up, two equations for the steady oblique rolls and two for the normal traveling rolls. This dissertation pursues a theoretical and numerical study of the patterns predicted by this system of globally coupled Ginzburg Landau equations.

Acharya et al presented a bifurcation analysis of the normal form that follows from the Ginzburg Landau system by ignoring slow variations. The basic solutions of the normal form are two types of pure mode solutions corresponding to ideal oblique stationary and normal traveling rolls, respectively, and superpositions of pure mode solutions, which are referred to as mixed mode solutions. Acharya et al distinguished two cases for the bifurcations of these solutions. In one case the mixed mode solution is stable and a continuous transition between the steady oblique rolls and the normal traveling rolls is predicted. For the other case, the mixed mode solution is unstable and bistability occurs between the steady oblique rolls and the normal traveling rolls.

In the present work, a numerical code was developed to simulate the spatiotemporal system of globally-coupled, complex Ginzburg-Landau equations using a pseudo-spectral method. The simulations of the system resulted in patterns that were consistent with the normal form analysis. Steady oblique and normal traveling rolls were found numerically. A region of bistability of the

steady oblique rolls and normal traveling rolls was found numerically, and a continuous transformation between the two primary branches via a stable mixed mode branch has been observed when the main bifurcation parameter is varied. Mixed mode solutions have been found that involved either amplitudes of steady rolls aligned in two different (“zig” and “zag”) directions, or amplitudes of two counter-propagating normal traveling rolls, for parameter values near the primary instabilities and when the initial conditions favored their appearance, and a bifurcation diagram showing the occurrence of steady state, steady oblique rolls, normal traveling rolls, mixed mode solutions, as well as bistability of the steady oblique rolls and normal traveling rolls has been obtained numerically.

TABLE OF CONTENTS

ABSTRACT.....		i
1	Introduction	1
1.1	Overview	1
1.2	Pattern Formation in Dissipative Systems.....	2
1.2.1	Couette-Taylor Flow.....	3
1.2.2	Rayleigh-Bénard Convection	6
1.2.3	Nematic Electroconvection	9
1.3	Symmetry and Equivariance	14
2	Mathematical Approaches to Pattern Formation.....	18
2.1	Mode Interactions	19
2.1.1	Generic Instabilities.....	19
2.1.2	Generic Mode Interaction.....	20
2.2	Derivation of the One-Dimensional Ginzburg-Landau Equation	22
2.3	Derivation of the Two-Dimensional Ginzburg-Landau Equations.....	29
2.4	Globally Coupled Ginzburg-Landau Equations for the WEM	33
3	Bifurcation Analysis of the Normal Form	37
3.1	Normal Form.....	37
3.2	Bifurcation Diagrams.....	39
4	Numerical Simulations	45
4.1	Numerical Implementation.....	46
4.2	Numerically Observed Patterns	49
4.2.1	Case I: Theoretical Bistability.....	53
4.2.2	Case II: Theoretically Stable Mixed Mode Solution.....	65
4.3	Bifurcation Diagram in the (c_r, ϕ) plane.....	98

4.4 Consistency of Numerical and Theoretical Results	99
5 Conclusions and Further Work.....	105
References	107
Appendix A Coutte-Taylor Example.....	112

1 Introduction

1.1 Overview

Pattern formation in extended systems is a major branch of applied mathematics and physics which contributes to various areas such as biology, chemistry, and engineering. Various mathematical models and numerous experiments devoted to the study of the mechanism generating patterns have given this topic a long history of findings and conjectures [21, 32, 12, 25, 38].

A stationary or an oscillatory instability, caused by the variation of a parameter, are the two generic ways in which a basic, spatiotemporally uniform state of a physical system loses stability. A theory of Turing instability was developed by Turing to explain the formation of stationary patterns on animals' skins as a result of chemical interactions with different diffusion rates [41]. Physicists investigated several fluid systems experimentally such as Rayleigh-Bénard convection or Taylor-Couette flow where they found organized patterns such as rolls and hexagons as well as disorganized patterns [7].

The degree of organization or symmetry in a pattern is an important feature to describe patterns. The steady state patterns, such as animals' skins, are described by spatial symmetry and moving patterns, such as in thermal convection and animal gaits, use space-time symmetry. Symmetries of the dynamical system can be used to investigate the nature of the pattern-formation mechanism. However, the patterns which lack symmetry and are chaotic in space and time are difficult to characterize using symmetry alone.

In [8, 36, 21, 16, 24] and references therein, a number of experimental and analytical studies of steady - oscillatory mode interaction in isotropic pattern forming systems, such as Taylor-Couette flow, Rayleigh-Bénard convection, and convection in binary mixtures have been reported. Renardy et al, in [36], explored mode interactions in Taylor-Couette flow of an upper convected Maxwell liquid. They studied the governing amplitude equations for

both a Hopf/steady state and a Hopf/Hopf mode interaction and described the stability of the resulting bifurcated solutions. The bifurcated solutions, none of which were found to be stable, resulted from the ‘pure’ modes, Taylor vortices for the steady state and ribbons and spirals for the Hopf mode.

Fujimura and Renardy [21] looked into a two-layer Bénard problem. They focused on the case when a pair of Hopf modes and a steady mode are simultaneously at criticality. Two possible solutions which were found to be unstable were a steady solution and traveling waves. However, a region of stable mixed standing waves was found as well.

In this work, we will consider physical systems posed in an extended two-dimensional domain which exhibit a steady-state/Hopf mode interaction. We will perform a quantitative analysis of this mode interaction through a bifurcation analysis of the associated ODE normal form and the numerical simulations of the Ginzburg-Landau system derived in [1].

In section 2, we review the derivation of the Ginzburg-Landau equations in one and two dimensions. This section includes the globally coupled Ginzburg-Landau equations for the steady-Hopf mode interaction case, followed by an overview of steady and oscillatory instabilities and mode interactions. Section 3 presents a theoretical study of the normal form of the globally coupled Ginzburg-Landau equations, including a theoretical bifurcation diagram. In section 4, numerical simulations of the globally coupled Ginzburg-Landau equations are discussed and compared with the theoretical results from section 3. Finally, section 5 contains a summary of the results and some possible extensions of the numerical analysis.

1.2 Pattern Formation in Dissipative Systems

The theory of pattern formation in dissipative systems has its origin in the observation of organized flow patterns in fluids. In this context, a bifurcation is a structural change in an observed flow when one or more parameters are progressively varied. When the bifurcation parameter crosses a critical value, a flow with certain symmetries may lose some of these symmetries, or a steady flow may become time dependent (which is also a symmetry breaking,

since the new flow is no longer invariant under shifts in time). A bifurcation occurs for instance when a branch of steady or time-periodic solutions (as function of parameter) loses its local uniqueness, in other words, it intersects another branch of different solutions and the crossing point is called the bifurcation point. The analysis of such bifurcations is the main tool for the understanding of the mechanism of pattern formation and appearance of complicated dynamics in fluid flows [8].

1.2.1 Couette-Taylor Flow

In Couette-Taylor experiments a viscous incompressible fluid is confined between two concentric rotating cylinders. In theoretical studies, e.g. [8], the cylinders are usually assumed to be infinitely extended, i.e. the fluid fills the domain $\mathcal{Q} = \Sigma \times \mathbb{R}$, where Σ denotes the cross section of the cylinders as shown in Figure 1. In cylindrical coordinates, (r, θ, z) , the cross section Σ is defined by $R_1 < r < R_2$, $\theta \in \mathbb{T}^1$, where \mathbb{T}^1 denotes the circle $\mathbb{R}/2\pi\mathbb{Z}$ and R_1 and R_2 denote the inner and outer radii of the cylinders respectively. The flow is

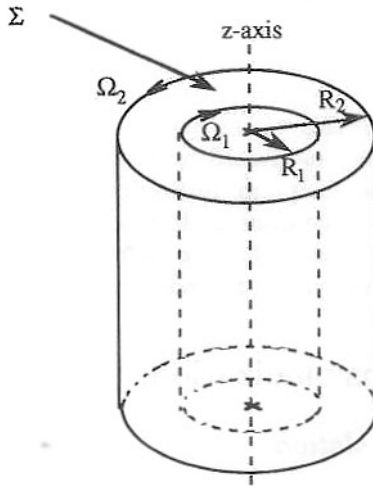


Figure 1: The geometry of the problem, from [8].

described by the Navier-Stokes equations on \mathcal{Q} ,

$$\begin{aligned} \frac{\partial V}{\partial t} + (V \cdot \nabla)V + \frac{1}{\rho} \nabla \rho &= \nu \Delta V + f \\ \nabla \cdot V &= 0 \end{aligned} \tag{1}$$

where ρ is the constant density, ν is the kinematic viscosity, p is the pressure, V is the velocity vector of fluid particles, f is the density of external forces per unit of mass, ∇ is the gradient, $\nabla \cdot$ is the divergence, and Δ is the Laplace operator. The functions V and p depend on (x, t) , with $x \in \mathcal{Q}$ often written $x = (y, z)$, $y \in \Sigma$ and $z \in \mathbb{R}$. The components of $V(x, t)$ are (v_r, v_θ, v_z) in cylindrical coordinates. The no-slip boundary conditions for fluid particles on the cylinders are expressed as $v_r = v_z = 0$ and $v_\theta = \Omega_j R_j$ at $r = R_j$, $j = 1, 2$ where Ω_j , $j = 1, 2$ respectively denote the angular velocities of the inner and outer cylinders [8].

A rich variety of patterns occur in Taylor-Couette experiments. The patterns have a degree of spatial and temporal symmetry. Also, as Ω_1 is increased patterns become more complicated, breaking more symmetries in space and time, leading to a turbulent regime which contains large-scale structures with many symmetries [8].

Couette flow is the exact solution of (1) which has the form of a pure azimuthal flow (ie. streamlines are concentric circles) and is seen when $\Omega_2 - \Omega_1$ is not too large [8]. If the outer cylinder is fixed and the inner cylinder is rotated at an angular velocity Ω_1 , then an instability occurs for Ω_1 exceeding a value Ω_{1c} according to Taylor [8].

Taylor's investigation used the idealization introduced above that the cylinders were of infinite length and with given nonzero axial periodicity [8]. The first instability he found occurred via a stationary and axisymmetric disturbance of the Couette flow. The value of Ω_{1c} found was close to the 'experimental' value and the predicted pattern of the solution associated with this type of disturbance was similar to the one observed in the experiment. The flow is called Taylor vortex flow and is a superposition of horizontal vortices of length exactly equal to half of the axial period of the basic disturbance, as seen in Figure 2a. The flow is axisymmetric, periodic along the axis of the cylinders and stationary.

When both cylinders are rotated, in opposite directions, rich 'routes' to turbulence are observed [8]. When the cylinders are co-rotating and Couette flow becomes unstable, Taylor

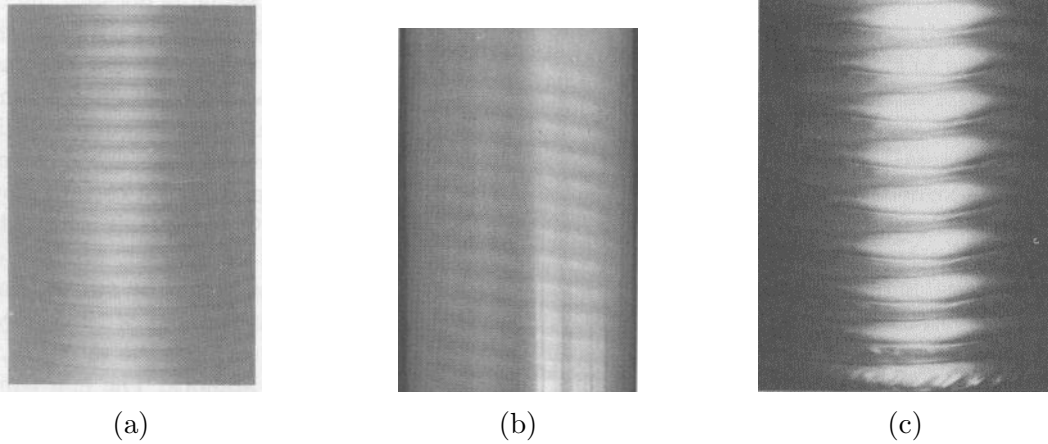


Figure 2: (a) Taylor vortex flow. (b) Spiral flow. (c) Wavy vortex flow, [8].

vortices are usually observed in experiments. Spiral flow, seen in Figure 2b, is usually the first instability observed when the cylinders are counter rotating [8].

Couette flow and Taylor vortex flow are stationary flows, while spiral flow and wavy vortex flow in Figure 2b-c are time periodic and assume the form of rotating waves. Spiral flow is also a traveling wave in the direction of the axis of the cylinders [8].

When the Reynolds number $R = R_1 \Omega_1 d / \nu$ is increased, more complicated spatio-temporal patterns are observed in the mode interaction regime. Some of them, such as the wavy vortex flow, Figure 2c, or the interpenetrating spirals, have been observed close to primary bifurcation curves. This stimulated theoreticians to explore such regimes by looking at higher codimension bifurcation points on the primary bifurcation curve [8], such as those leading to steady state-steady state, steady state-Hopf, or Hopf-Hopf mode interactions.

Additional parameters which are allowed to vary will be necessary to look at these higher codimension bifurcation points [8]. The basic parameter is the average angular velocity, $\Omega = 1/2(\Omega_1 + \Omega_2)$. Depending on Ω , Couette flow can lose stability by either an eigenvalue crossing the imaginary axis at zero with axisymmetric eigenvectors (azimuthal wave number $m = 0$) or by a pair of purely imaginary eigenvalues with nonzero azimuthal wave number for the eigenmodes [8]. Both wavy vortex flow and twisted vortices are mixed mode solutions consisting of stationary and time-periodic modes. These solutions can be studied analytically

near a mode interaction point where both instabilities occur simultaneously when a second parameter is fixed to a critical value. The analysis of this mode interaction is explored further in Appendix A.

1.2.2 Rayleigh-Bénard Convection

One of the most comprehensively studied nonequilibrium fluid systems in both experimental and theoretical aspects is the Rayleigh-Bénard convection. In this experiment a viscous fluid is placed between two flat horizontal plates. Heat conductors for the plates maintain the lower plate at a temperature above the upper plate temperature. The temperature difference, ΔT , leads to the fluid near the bottom plate expanding and being less dense than the fluid near the top plate. Assuming the density ρ depends linearly on the temperature, the fluid from the bottom tends to rise due to the buoyancy force. For sufficiently small ΔT the fluid remains at rest and heat is transported only by conduction from the bottom plate to the top one. When the temperature difference ΔT is strong enough to overcome the resistance effects due to viscosity, convection sets in resulting in various kinds of Rayleigh-Bénard convective patterns.

The Rayleigh number,

$$R = \frac{\alpha g \Delta T d^3}{\kappa \nu}, \quad (2)$$

is one control parameter and is the dimensionless ratio of the destabilizing buoyancy force to the stabilizing dissipative force, where α is the thermal expansion coefficient for the fluid, g is the acceleration of gravity, ν is the kinematic viscosity, κ is the thermal diffusivity, and d is the plate separation distance. Another dimensionless parameter, the Prandtl number,

$$\sigma = \frac{\nu}{\kappa}, \quad (3)$$

represents the ratio of the two dampening mechanisms acting on the fluid, viscosity and thermal conductivity.

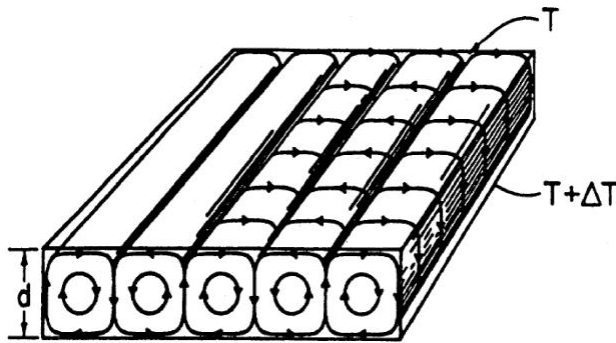


Figure 3: Schematic representation of the idealized roll pattern from Rayleigh-Bénard convection, from [10].

When R is slightly above the critical value R_c , convective rolls are observed. The growth of the pattern is limited due to the convective flow which transports part of the heat, thus decreasing the temperature gradient and the buoyancy force; these nonlinear effects force the fluid to settle down to a certain level and convective rolls are formed with diameters close to the separation distance d as illustrated in Figure 3.

Superpositions of rolls forming hexagons or squares can develop from other instabilities and parameters of the experiment [2]. Hexagons, rolls, and squares, as shown in Figure 4, are found in physical experiments above onset in different geometries.

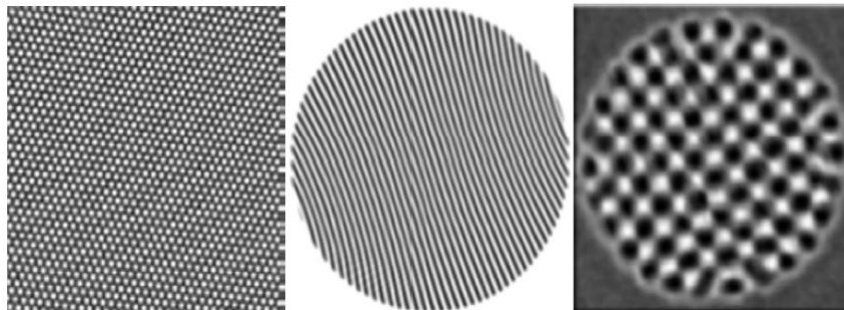


Figure 4: Hexagonal, roll, and square patterns from Rayleigh-Bénard convection in different geometries, from [2].

Increasing R further above the critical value R_c results in the convection patterns possibly becoming complex in space and time leading to spatio temporal complexity and chaos (STC). Factors that STC depends on are the size of system, the Rayleigh number, the Prandtl

number, and the geometry of the experimental devices [2, 10]. As the spatial extent increases more degrees of freedom of the STC become important.



Figure 5: Two examples of STC from Rayleigh-Bénard convection under different conditions. (b) from [26] and (a) from [30].

Two examples of STC are shown in Figure 5. In Figure 5a it is shown a complex pattern formed experimentally exhibiting the coexistence of domains of rolls of more or less uniform orientation when a horizontal fluid is rotated about a vertical axis [26]. Another type of experimentally observed STC, spiral-defect chaos, consisting of moving, rotating spirals and other defects in the roll structure is shown in Figure 5b [30]. The defects have modest lifetime and drift about irregularly, and new defects are constantly created as old ones disappear.

A similar case to explore is where the space between the plates is filled by two fluids with different thermal and mechanical properties. Bifurcations from the rest state, in which the temperature profile in each fluid is linear, have been studied in [21] and steady-Hopf mode interaction has been observed. The destabilizing mechanism is the temperature difference. Depending on the stratification in the fluid properties, the presence of two liquids and an interface introduces other destabilizing or stabilizing mechanisms [21]. The possible bifurcating solutions are standing rolls and traveling rolls according to Ruelle [37]. Both are unstable if either is subcritical and one of them is stable if both are supercritical. An aspect of the

interaction of Hopf and steady modes is that they may be subcritical and yet give birth to a mixed mode which is stable in some parameter range. While choosing a stratification in the thermal conductivities to stabilize the interface and choosing a Rayleigh number that is not too far from the onset of the one-fluid problem, so as to destabilize the bulk modes, the situation where a pair of Hopf modes with wavenumber α and a steady mode at wavenumber 2α are simultaneously at criticality was investigated in [21]. The interfacial mode and the least stable bulk mode combine to form a complex conjugate pair which reaches criticality at wavenumber α under these competing mechanisms. A small adverse density difference forces the steady mode to reach criticality at 2α and surface tension effectively stabilizes shorter waves [21].

1.2.3 Nematic Electroconvection

Electroconvection in nematic liquid crystals has been the testing system for many experimental studies and theoretical predictions for pattern formation in spatially extended systems, [28, 4, 5], due to the wide variety of pattern formation phenomena that occur in the system. It is also the primary example in the study of anisotropic dissipative structures. In electroconvection, a charge carrying fluid is sandwiched between two electrode glass plates across which an electric potential difference is applied. The molecules of nematic liquid crystals are on average locally oriented along a preferred direction, called the director, unlike ordinary isotropic fluids such as in Rayleigh-Bénard convection. The system is favored experimentally for its easily accessible control parameters, namely the amplitude and frequency of the applied voltage, short time scales, and high aspect ratio. An electrohydrodynamic instability combined with a transition from the uniform state to a variety of patterns can occur when the applied voltage is above a critical value [28]. Depending on the frequency, at onset periodic patterns of normal or oblique convective rolls are typically observed. Transitions take place either to complex spatio-temporal states, induced by defects, or to more complicated quasi-periodic patterns when the voltage is increased.

A unique reduced mathematical description for nematic electroconvection through four amplitudes associated with two counter propagating pairs of traveling waves in two oblique directions, whose dynamics are governed by corresponding Ginzburg-Landau amplitude equations, and that takes into account the anisotropy, results in four critical wave vectors with nonzero angles with respect to the director. Zig rolls refer to one pair of traveling waves in one oblique direction, and the traveling waves in the other oblique direction are referred to as zag rolls. Experimental observation of a variety of patterns was reported in [17, 19, 18]. One of the patterns is an alternating-wave pattern seen in Figure 6 [19], which results from a superposition of zig and zag standing waves, where one standing wave is one quarter of cycle out of phase with the other. A second pattern is STC for a different set of control parameters where spatial demodulation is performed to generate amplitudes of the zig and zag waves in Figure 7 [17].

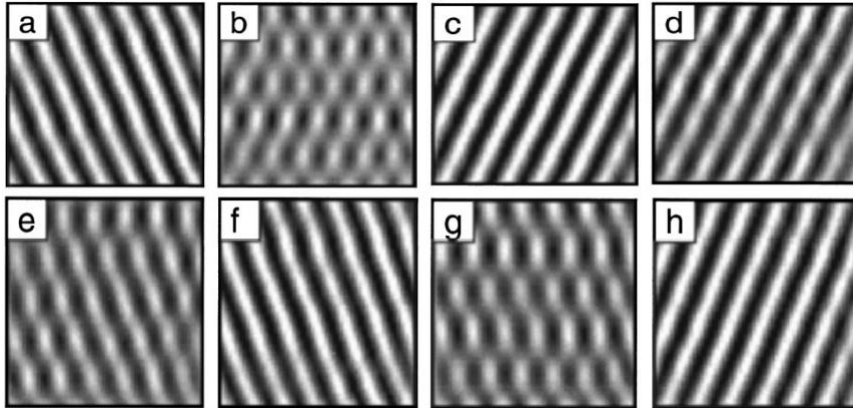


Figure 6: A time series of a pattern alternating between zig and zag rolls in nematic electroconvection, from [19].

The weak electrolyte model (WEM) has been developed to model the electroconvection (EC) in nematic liquid crystals [40]. The WEM is a particular case of an axially anisotropic, dissipative system with two extended dimensions (x, y) . In such systems the axial anisotropy induces reflection and translation invariance in both extended directions, thus the underlying symmetry group is $E(1) \times E(1)$ which compactifies to $O(2) \times O(2)$ if periodic boundary conditions are imposed [32]. The WEM is an extension of the standard model [6] by includ-

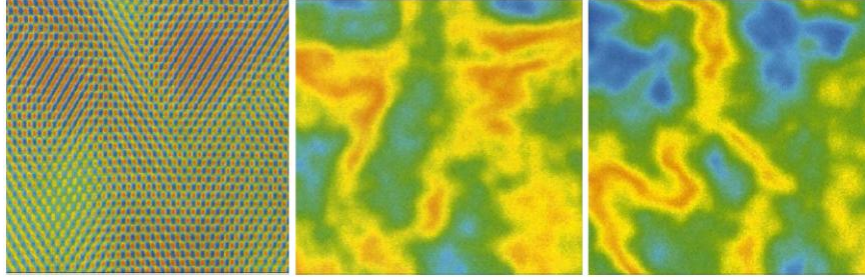


Figure 7: Left: an example of STC in nematic electroconvection. The maxima and minima are mapped to blue and red, respectively. Middle: the envelope of the zig rolls. Right: the envelope of the zag rolls, from [17].

ing the slow dissociation-recombination process of the charge carrying ions and the ohmic behavior replaced by the dynamics of two species of oppositely charged mobile ions. It provides a basis for understanding the Hopf bifurcation which predicts the travelling wave patterns observed experimentally, as was studied in [12, 29, 43]. Above the critical value of the applied voltage an electrohydrodynamic instability combines with a transition from the uniform state to show a variety of patterns such as stationary and travelling rolls and complex spatiotemporal structures (worms, defects, and spatiotemporal chaos). As shown in Figure 8, so far there has been fair agreement between the analysis of the WEM and experiments, but more accurate numerical computation for other parameters and other types of instabilities are necessary to test the validity of the WEM [12]. At onset, the WEM can

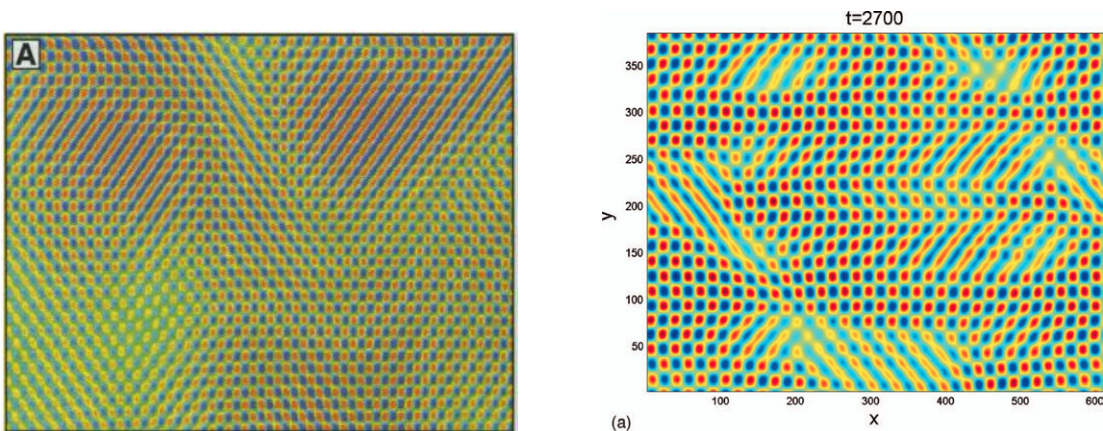


Figure 8: On the left, a zig-zag chaos pattern seen experimentally [17]. On the right, a pattern computed numerically [33].

show an oscillatory or stationary instability either of which can lead to oblique or normal

rolls depending on the parameters. This allows for the occurrence of steady-oscillatory mode interactions.

Physicists at Kent State University studied the nematic mixture Phase V in the standard planar EC geometry, and observed a discontinuous jump in the Hopf frequency from zero (stationary state) to over 20 rad/sec as the driving frequency is increased along the threshold curve [1]. Measurements of the wave vector components also exhibit an abrupt jump in their values at the oblique stationary to normal traveling transition regime. The stationary oblique (OS), Figure 9a, and normal traveling (NT), Figure 9b, patterns during electroconvection were recorded using shadowgraph technique [35]. This experimentally observed steady oblique - Hopf normal traveling behavior can be understood through a straightforward consideration of the relevant amplitude equations near this codimension-2 bifurcation point.

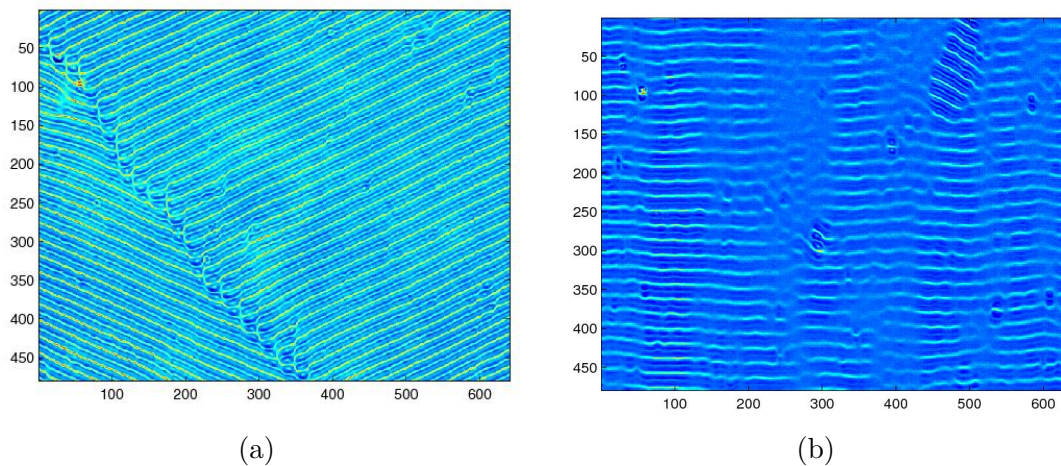


Figure 9: (a) Experimentally observed stationary oblique rolls. (b) Experimentally observed normal traveling rolls.

In recent experiments in a box with large aspect ratios, a jump in the Hopf frequency from zero to over 20 rad/sec was observed experimentally as the driving (AC) frequency was increased above a critical value [1], meaning that there were oblique stationary rolls at lower frequencies and normal traveling rolls at higher frequencies. The critical AC frequency and the corresponding electroconvective threshold voltage determine the mode interaction

point [1], further implying that the mode interaction is caused by the same minimal voltage for two neutral stability surfaces. The two fixed parameters imply that we are dealing with a codimension-two bifurcation point with a discontinuity in the Hopf frequency, wave numbers, and roll angle [1]. This stationary-Hopf mode interaction can be modeled by four two-dimensional anisotropic Ginzburg-Landau equations to describe the time evolution of the amplitudes [1].

The minimum of a neutral stability surface in (V, p^2, q^2) -space determines the critical onset voltage where V is the applied voltage and p, q are the horizontal and vertical wave numbers [1]. Let $V_s(p^2, q^2, \omega_0)$ be the stationary neutral stability surface with minimum $V_{sc}(\omega_0) = V_s(p_{sc}^2, q_{sc}^2, \omega_0)$, where ω_0 is the circular frequency of the applied ac-voltage. Also, let $V_o(p^2, q^2, \omega_0)$ to be the oscillatory neutral stability surface with minimum $V_{oc}(\omega_0) = V_o(p_{oc}^2, q_{oc}^2, \omega_0)$ and Hopf frequency $\omega_H(\omega_0)$ at criticality [1]. Experimentally normal traveling rolls were observed leading to $q_{oc}(\omega_0) = 0$ and at the critical value of the AC frequency $V_{oc}(\omega_{oc}) = V_{sc}(\omega_{oc})$ [1]. Also, $V_{oc}(\omega_0) > V_{sc}(\omega_0)$ if $\omega_0 < \omega_{oc}$ and $V_{oc}(\omega_0) < V_{sc}(\omega_0)$ if $\omega_0 > \omega_{oc}$. From this we deduce that the critical wave numbers at onset are $(p_{sc}(\omega_0), q_{sc}(\omega_0))$ for $\omega_0 < \omega_{oc}$ and $(p_{oc}(\omega_0), 0)$ for $\omega_0 > \omega_{oc}$. The codimension-two mode interaction point, $\omega_0 = \omega_{oc}$, is determined by setting $V = V_{sc}(\omega_{oc}) = V_{oc}(\omega_{oc})$, and is associated with the normal traveling rolls frequency $\omega_H(\omega_{oc})$ [1]. A jump is expected in both the horizontal and vertical critical wave numbers since there is no relation between the locations of the minima on the two neutral stability surfaces [1]. Two transition scenarios are possible, either it is a continuous transition via a stable mixed mode branch or a region with bistability and an unstable mixed mode branch leading to a hysteretic transition. The experiments do not yet provide evidence which of the two scenarios is present in the physical system. Further experiments and a thorough analysis of the recorded patterns is necessary to discriminate between the two scenarios. The next step in the theoretical analysis of the mode interaction is a numerical study of the patterns predicted by the globally coupled Ginzburg Landau equations. The two

normal form scenarios described lead to somewhat different spatiotemporal patterns which will hopefully provide further criteria allowing to distinguish between them in experiments.

In Section 3 we will describe and study analytically the Ginzburg-Landau equations in detail, and in Section 4 we will describe their numerical simulations in the case of mode interactions.

1.3 Symmetry and Equivariance

The spontaneous breaking of the symmetry leads to pattern formation [10]. The concept of a symmetry of a dynamical system and the concept of a symmetry of a pattern, which is a solution of the governing equations of the dynamical system, in terms of equivariant theory are required to formalize pattern formation from a symmetry point of view [9, 22, 23]. To simplify the discussion, we consider here finite dimensional dynamical systems. The extension to infinite dimensional dynamical systems including systems of PDEs such as (1) is straightforward, but requires additional technical considerations that are not relevant from a symmetry perspective.

Let the dynamical system in \mathbb{R}^n be written as

$$\frac{dx}{dt} = f(x, \lambda), \quad (4)$$

where the smooth vector field $f : \mathbb{R}^n \times \mathbb{R}^r \rightarrow \mathbb{R}^n$ depends on a set of parameters $\lambda \in \mathbb{R}^r$.

Also, assume γ is an $n \times n$ invertible matrix. Define a symmetry of a dynamical system as

Definition 1 *The invertible $n \times n$ matrix γ is a symmetry of (4) if for every solution $x(t) \in \mathbb{R}^n$ of (4), $\gamma x(t)$ is also a solution.*

Both γ^{-1} and $\gamma\delta$ satisfy Definition 1 if γ and δ are invertible matrices satisfying Definition 1. Thus, the set of symmetries of a dynamical system forms a group. Now, extend the concept of a symmetry in Definition 1 from a matrix to an abstract group element by representation theory and call an element γ of a group Γ a symmetry of the dynamical system (4) if there is

a representation T_γ acting on \mathbb{R}^n such that the matrix T_γ satisfies the hypothesis of Definition 1 (for ease of notation write $\gamma x \equiv T_\gamma x$).

However, a more useful condition than Definition 1 is needed to determine whether a group element γ is a symmetry of a dynamical system (4). Suppose $y(t) = \gamma x(t)$ is another solution of (4) then

$$\dot{y}(t) = f(y(t)) = f(\gamma x(t)) \quad (5)$$

and

$$\dot{y}(t) = \gamma \dot{x}(t) = \gamma f(x(t)). \quad (6)$$

Thus,

$$f(\gamma x(t)) = \gamma f(x(t)) \quad (7)$$

for all solutions $x(t)$ of (4). Since solutions exist for any arbitrary initial conditions this is equivalent to

$$f(\gamma x) = \gamma f(x) \text{ for all } x \in \mathbb{R}^n. \quad (8)$$

This gives equivariance.

Definition 2 (Γ -equivariance) *Let Γ act on \mathbb{R}^n and let $f : \mathbb{R}^n \times \mathbb{R}^r \rightarrow \mathbb{R}^n$ in (4). Then f is Γ -equivariant and Γ is a symmetry group for (4) if $f(\gamma x, \lambda) = \gamma f(x, \lambda)$ for all $\gamma \in \Gamma$, $x \in \mathbb{R}^n$.*

Next, we need to formalize the notion of the symmetry of a pattern created in an equivariant dynamical system. In a finite dimensional setting, a pattern is defined as an element x in the vector space \mathbb{R}^n in which (4) is posed. The symmetry of the pattern x is a group element σ from Γ in definition 2 such that $\sigma x = x$. The set of all such σ 's also preserves a group structure and the resulting group is known as the isotropy subgroup of x , as defined in Definition 3.

Definition 3 (Isotropy subgroup) *Let $v \in \mathbb{R}^n$. The isotropy subgroup of v is*

$$\Sigma_v = \{\sigma \in \Gamma : \sigma v = v\}. \quad (9)$$

A pattern's isotropy subgroup can provide useful information. Using all isotropy subgroups of the system a technique for finding solutions with specific symmetries can be developed. In order to classify different isotropy subgroups we need the following definition.

Definition 4 (Group orbit) *Let $x \in \mathbb{R}^n$ and $\gamma \in \Gamma$. The group orbit of x is*

$$\Gamma x = \{\gamma x : \gamma \in \Gamma\}. \quad (10)$$

From Definition 4, the conjugacy property, $\Sigma_{\gamma x} = \gamma \Sigma_x \gamma^{-1}$, is apparent. This leads to the isotropy subgroup of γx being a conjugate subgroup of the isotropy subgroup of x . One considers conjugate isotropy subgroups to be different realizations of the same symmetry and classifies patterns in terms of conjugacy classes of isotropy subgroups, by which we mean the set of all conjugates of a given isotropy subgroup. The relations between different conjugacy classes are defined by containment. We define the following abstract structure to formalize this concept.

Definition 5 (Conjugacy classes) *Let $H = \{H_i\}$ and $K = \{K_j\}$ be two conjugacy classes of isotropy subgroups of Γ . Define a partial ordering \leq on the set of such conjugacy classes by*

$$H \leq K \Leftrightarrow H_i \subseteq K_j \quad (11)$$

for some representatives H_i, K_j . The isotropy lattice of Γ in its action on \mathbb{R}^n is the set of all conjugacy classes of isotropy subgroups, partially ordered by \leq .

The isotropy lattice classifies all possibilities for a pattern to break symmetry and can be arranged in a hierarchy with the property that smaller isotropy subgroups correspond to breaking more symmetries. Using the structure of the isotropy lattice for a given symmetry

group, a systematic method to search for patterns with any possible symmetries is given in the following definition.

Definition 6 (Fixed-point subspace) *Let $\Sigma \subseteq \Gamma$ be a subgroup. The fixed-point subspace of Γ is*

$$Fix(\Sigma) = \{v \in \mathbb{R}^n : \sigma v = v, \forall \sigma \in \Sigma\}. \quad (12)$$

The following theorem is important to the development of the theory of equivariant dynamics.

Theorem 1 *Let $f : \mathbb{R}^n \rightarrow \mathbb{R}^n$ be Γ -equivariant and let $\Sigma \subseteq \Gamma$ be a subgroup. Then*

$$f(Fix(\Sigma)) \subseteq Fix(\Sigma). \quad (13)$$

Theorem 1 implies that the dynamics of a pattern with isotropy subgroup Σ is restricted to the subspace $Fix(\Sigma)$. Therefore to seek a pattern from a dynamical system with isotropy subgroup Σ , we restrict the search to the subspace $Fix(\Sigma)$. The searching problem is posed in a space of lower dimension and ought to be simpler, unless $Fix(\Sigma)$ is the whole space \mathbb{R}^n . The larger Σ is, the smaller is the dimension of $Fix(\Sigma)$. We can start with the largest subgroups in the lattice of isotropy subgroups and work down the lattice systematically to determine patterns of the system with successively lower symmetries. This means working from the larger isotropy subgroups down to the smaller ones.

2 Mathematical Approaches to Pattern Formation

Systems of Ginzburg Landau equations are commonly used to describe pattern formation in spatially extended, dissipative systems. The equations govern the evolution of slowly varying envelopes of periodic spatiotemporal patterns determined by a linear stability analysis of a basic, homogeneous solution of a system of PDEs. The stationary bifurcation in systems with one extended spatial direction (one dimensional systems) leads to a standard real one-dimensional Ginzburg Landau equation for a single envelope of a spatially periodic, but temporally constant plane wave pattern. The Hopf bifurcation in one dimensional systems requires two envelopes for two counterpropagating traveling waves. The basic patterns are now periodic in space and time. It is complicated further by the group velocity of these waves being finite and energy being transported fast, thus the waves interact on average rather than locally in space. This leads to two globally coupled Ginzburg Landau equations for the envelopes of the two traveling waves. In the two dimensional Hopf bifurcation case the linear stability analysis leads to two pairs of counterpropagating waves in two oblique directions. This means that there are four possible basic wave patterns, thus four envelopes are needed to describe the instability. The finite group velocities lead to a system of four globally coupled Ginzburg Landau equations for the envelopes. The four complex Ginzburg-Landau equations derived in [15] are used to study evolution of traveling envelopes arising in a weakly nonlinear analysis of the WEM equations. A comprehensive bifurcation analysis of the WEM demonstrating the existence of a primary Hopf instability involving four oblique rolls was pursued in [12, 13].

2.1 Mode Interactions

2.1.1 Generic Instabilities

The solutions of a system of differential equations can change depending on the parameters. A small change in the parameter commonly leads to a small change in the behavior of the solutions. Near certain critical parameter values, a small change in the parameter can lead to a qualitative change in the long-term behavior of the solutions. The parameter values where such a change occurs are called a bifurcation points [39]. Consider the following equation

$$\frac{dz}{dt} = F(z, R), \quad (14)$$

where $z \in \mathbb{R}^n$, $t \in \mathbb{R}$, R represents the bifurcation parameters, and $F \in C^k(\mathbb{R}^n, \mathbb{R}^n)$ for a large enough integer k . The points z^* where $F(z^*, R) = 0$ are the equilibrium points of the system.

A local bifurcation occurs when the Jacobian matrix, $DF = \left(\frac{\partial F_i(z, R)}{\partial z_j} \right)_{i,j=1,\dots,n}$, evaluated at an equilibrium has eigenvalues on the imaginary axis [23]. As R is increased, the first eigenvalues with zero real part are called ‘critical’ eigenvalues. The surface where a critical eigenvalue has zero real part is a neutral stability surface in the parameter space. A steady state/stationary bifurcation occurs when the critical eigenvalue is zero. A Hopf/oscillatory bifurcation occurs when there is a pair of nonzero purely imaginary critical eigenvalues.

‘Modes’ commonly refers to the eigenfunctions corresponding to the eigenvalues of the Jacobian matrix [23]. A mode is stable if the real part of the eigenvalue is negative and unstable if the real part is positive. When the eigenvalue is positive the eigenfunction ‘increases’ without bound, in contrast when the eigenvalue is negative the eigenfunction is bounded.

A single local bifurcation that depends on one parameter is called a codimension-one bifurcation. Thus, two local bifurcations occurring simultaneously is called a (local) codimension-two bifurcation or mode interaction [23]. The two modes involved in mode

interactions are usually coupled by the nonlinear terms, which often combines the behaviors of the two modes to create more complicated behavior than is expected from them separately [23].

2.1.2 Generic Mode Interaction

For a linear stability analysis of a system of nonlinear PDEs for field variables $U(t, \mathbf{x})$, the PDEs are separated into linear, $L(\nabla, R, \mu)$, and nonlinear, N , parts

$$\frac{\partial U}{\partial t} = L(\nabla, R, \mu)U + N(\nabla, U, R, \mu), \quad (15)$$

where R is the main bifurcation parameter, such as the Rayleigh number in Rayleigh Bénard convection, and μ is another parameter (e.g. a material parameter). Also, let $\mathbf{x} = (x, z)$, with the horizontal (x) direction infinitely extended, $-\infty < x < \infty$, while the vertical (z) direction is bounded, $0 < z < d$.

The ansatz $U(t, \mathbf{x}) = e^{\sigma t} e^{ikx} U_k(z)$ is used to transform the linearized equation of (15) to the eigenvalue problem,

$$L(ik, \partial_z, R, \mu)U_k = \sigma(k, R, \mu)U_k. \quad (16)$$

A countable set of eigenvalues, $\sigma_m(k, R, \mu)$ with $m = 1, 2, \dots$, results from z being bounded.

Since, in general,

$$\sigma_m(k, R, \mu) = \sigma_{mr}(k, R, \mu) + i\omega_m(k, R, \mu), \quad (17)$$

the mode $e^{ikx} U_k(z)$ is neutrally (or marginally) stable if $\sigma_m(k, R, \mu) = 0$. Assuming this equation can be solved for R for each m , $R = R_m(k, \mu)$, we have for fixed μ a countable set of neutral stability curves $R_m(k, \mu)$ in the (k, R) -plane. Typically, each of these curves has a minimum R_{mc} at a wave number $k_{mc}(\mu)$, $R_{mc}(\mu) = R_m(k_{mc}(\mu), \mu)$. The instability of the basic state ($U = 0$) sets in when R exceeds the lowest of these minima, i.e. for

R below this value $\sigma_{mr} < 0$ for all m and k and the basic state is asymptotically stable. Assuming that the lowest minimum occurs for $m = 1$, the “onset value” or “critical value” of R is $R_c(\mu) = R_{c1}(\mu)$ and the corresponding wave number is referred to as the “critical wave number”, $k_c(\mu) = k_{c1}(\mu)$. The neutral stability curve $R_1(k, \mu)$ for fixed μ is sketched in Figure 10. The type of instability at R_c can be stationary ($\omega_1(k_c, \mu) = 0$) or oscillatory

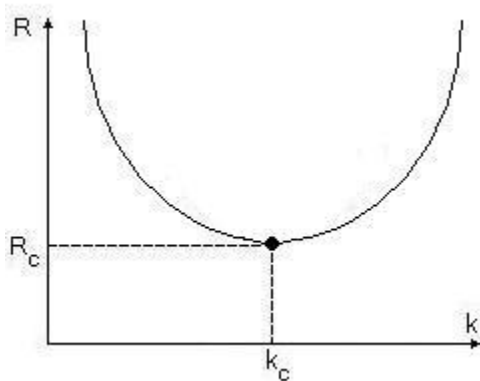


Figure 10: Neutral Stability curve either stationary or oscillatory.

($\omega_1(k_c, \mu) \neq 0$).

If μ is varied, the minima $R_{mc}(\mu)$ vary as well, and it may happen for a critical value, μ_c , of μ that two minima, say R_{c1} and R_{c2} , coincide with $R_{mc} > R_{1c} = R_{2c}$ for $m > 2$. This gives rise to a codimension-two linear mode interaction as illustrated in Figure 11.

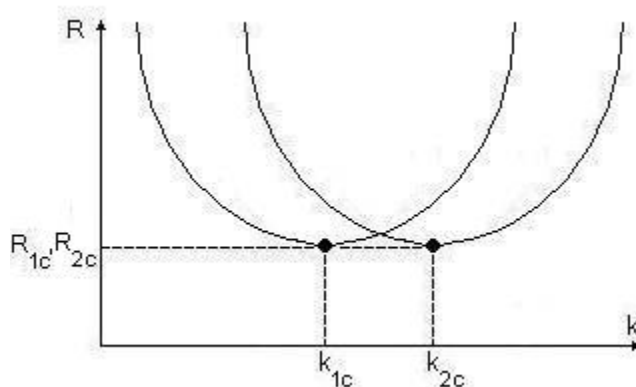


Figure 11: Neutral Stability curves either stationary or oscillatory at a mode interaction.

There are three types of codimension-two linear mode interactions:

- (i) Steady-state/steady-state mode interaction which has two stationary bifurcations,
- (ii) Steady-state/Hopf mode interaction which has one stationary bifurcation and one oscillatory bifurcation, and
- (iii) Hopf/Hopf mode interaction which has two oscillatory bifurcations [22].

The usual multiple bifurcation phenomenon is that of steady-state/steady-state mode interactions, which is when two different stationary modes simultaneously bifurcate from a trivial solution of an evolution equation. This mode interaction may occur, for example, in reaction-diffusion equations [11]. Both steady-state/Hopf and Hopf/Hopf mode interaction can occur for different parameters in viscoelastic Taylor-Couette flow [36]. We present in Appendix A the derivation of amplitude equations in the case of the interaction of an axisymmetric mode and a nonaxisymmetric mode. Boussinesq magnetoconvection also shows steady-state/Hopf mode interaction under specific conditions [16].

The steady-state/Hopf interaction is the one of interest and has been studied in various systems [1, 8]. An example of an anisotropic system exhibiting steady state-Hopf mode interaction is the electroconvection of the nematic mixture Phase V [1]. Previously, the Phase V sample was sandwiched in a “channel” (thin cell in one direction) and exhibited a transition from traveling to stationary normal rolls at the critical frequency. One-dimensional Ginzburg-Landau equations sufficed to describe the amplitudes.

Following is an overview of the Ginzburg Landau equations in one and two dimensions.

2.2 Derivation of the One-Dimensional Ginzburg-Landau Equation

To derive the Ginzburg-Landau equations, we begin with a linear stability analysis of a nonlinear PDE for field variables $U(t, \mathbf{x})$. As in Section 2.1.2, the PDE is separated into a linear, $L(\nabla, R)$, and a nonlinear, N , part

$$\frac{\partial U}{\partial t} = L(\nabla, R)U + N(\nabla, U, R), \quad (18)$$

where here we consider only one bifurcation parameter, R .

In the case of a one-dimensional stationary bifurcation, we let $\mathbf{x} = (x, z)$ with the horizontal (x) direction infinitely extended, $-\infty < x < \infty$, while the vertical (z) direction is bounded, $0 < z < d$. The ansatz $U(t, \mathbf{x}) = e^{\sigma t} e^{ikx} U_k(z)$ leads again to the eigenvalue problem,

$$L(ik, \partial_z, R)U_k = \sigma(k, R)U_k, \quad (19)$$

with a countable set of eigenvalues, $\sigma_m(k, R)$, $m = 1, 2, \dots$. For R below a critical R_c , all eigenvalues have negative real parts. At the onset of instability, $R = R_c$, a single eigenvalue, σ_1 , has zero real part. This eigenvalue is referred to as the critical eigenvalue.

Since we are dealing with a stationary bifurcation, the critical eigenvalue $\sigma(k, R) \equiv \sigma_1(k, R)$ is real and the neutral stability curve is defined by

$$\sigma(k, R) = 0. \quad (20)$$

Usually the equation (20) has a smooth solution called the stationary neutral stability curve, $R = R_s(k)$, with a minimum $R_c = R_s(k_c)$ at a ‘critical’ wave number k_c . The critical eigenvalue $\sigma(k, R)$ is negative below this curve and positive above it. Thus, below this curve the basic solution is stable. For $R - R_c \sim \epsilon^2$, where ϵ is small and $R > R_c$, there is a band of linearly unstable wave numbers, k , around k_c for which $\sigma(k, R) > 0$ [20].

The minimum R_c , of $R_s(k)$, is also attained at $-k_c$ when the governing PDE is invariant under the reflection operation $x \rightarrow -x$. Thus, when $R = R_c$ the linearized PDE, $\frac{\partial U}{\partial t} = LU$, has the non-decaying, temporally constant and spatially periodic solution

$$U(\mathbf{x}) = U_c(z)e^{\pm ik_c x} \quad (21)$$

where $U_c = U_{k_c}$ is the critical vertical mode. Near (k_c, R_c) the eigenvalue $\sigma(k, R)$ can be expanded as

$$\sigma(k, R) = \alpha(R - R_c) + d(k - k_c)^2 + \dots \quad (22)$$

where $\alpha = (\frac{\partial \sigma}{\partial R})_c$ and $d = \frac{1}{2}(\frac{\partial^2 \sigma}{\partial k^2})_c$ and the subscript c means the expression is evaluated at (k_c, R_c) . For the solution of the linearized problem we make the ansatz

$$U(t, \mathbf{x}) = A(t, x)e^{ik_c x}U_c(z) + cc \quad (23)$$

where cc denotes the complex conjugate expression and $A(t, x)$ is a small and slowly varying complex amplitude. We then use the relationship $ik \leftrightarrow \frac{\partial}{\partial x}$ to derive the linear PDE for A from σ . With (22) truncated at the quadratic term, this gives

$$\frac{\partial A}{\partial t} = \lambda A + d \frac{\partial^2 A}{\partial x^2} \quad (24)$$

with $\lambda = \alpha(R - R_c)$ [20]. Using a weakly nonlinear analysis, this equation can be extended to a nonlinear equation for A whose solutions correspond to asymptotic solutions of the original PDE (18) via (23). The symmetries of (18) restrict the symmetries of this equation. The translation invariance of (18) requires the invariance of the PDE for A against phase shift transformation, $A \rightarrow e^{ik_c \xi} A$. The reflection $x \rightarrow -x$ gives $e^{ik_c x} \rightarrow e^{-ik_c x}$. The reflection invariance of (18) requires the invariance of the PDE for A against $A \rightarrow \bar{A}$ (where the bar denotes complex conjugate). Under these symmetry operations, the only invariant nonlinear term up to cubic order is $a|A|^2 A$ with a real parameter a [20]. Thus up to cubic order the nonlinear extension of the PDE for A is

$$\frac{\partial A}{\partial t} = \lambda A + d \frac{\partial^2 A}{\partial x^2} + a|A|^2 A. \quad (25)$$

Considering only values of R slightly above R_c , we rescale the PDE (25) using $X = \epsilon x$, $T = \epsilon^2 t$, and $A = \epsilon B$. This results in

$$\frac{\partial B}{\partial T} = \Lambda B + d \frac{\partial^2 B}{\partial X^2} + a|B|^2 B \quad (26)$$

where $\Lambda = \alpha(R - R_c)/\epsilon^2$ is the rescaled bifurcation parameter. Since it has real coefficients, (26) is called the ‘‘real Ginzburg-Landau equation’’. The nonlinear coefficient a is uniquely determined by the quadratic and cubic terms of N [20]. If $a < 0$ the solutions of (26) are bounded and evolve toward a stationary solution and the bifurcation is called supercritical. On the other hand, if $a > 0$ the solutions may grow without bound and the bifurcation is called subcritical. In the supercritical case, the main property of the solutions manifold of (26) is many kink-like stationary solutions, which induce wave number jumps in the solution of the original PDE [20].

The case of a one-dimensional Hopf bifurcation is similar except that the critical eigenvalue is complex,

$$\sigma(k, R) = \sigma_r(k, R) + i\omega(k, R). \quad (27)$$

This means that $\sigma_r(k, R) = 0$ defines the oscillatory neutral stability curve. The critical frequency is the frequency at the minimum of the neutral stability curve, $\omega_c = \omega(k_c, R_c)$. A pair of counterpropagating traveling wave solutions,

$$U(t, \mathbf{x}) = e^{i\omega t} e^{\pm ik_c x} U_c(z), \quad (28)$$

is possible at criticality of the linearized problem. Two small and slowly varying complex envelopes, A_l and A_r , for left and right traveling waves must be introduced to describe the non-decaying solutions of the linearized problem,

$$U(t, \mathbf{x}) = e^{i\omega_c t} (A_l(t, x) e^{ik_c x} + A_r(t, x) e^{-ik_c x}) U_c(z) + cc. \quad (29)$$

Expanding $\sigma(k, R)$ about (k_c, R_c) leads to the PDE-system for A_l, A_r . The complex σ expansion is

$$\sigma(k, R) = i\omega_c + \alpha(R - R_c) + iv(k - k_c) + d(k - k_c)^2 + \dots \quad (30)$$

with the critical group velocity, $v = (\partial\omega/\partial k)_c$, and α and d defined as in stationary case. However, while v is real, α and d are usually complex. Due to the v -term, the expansion about $(-k_c, R_c)$,

$$\sigma(k, R) = i\omega_c + \alpha(R - R_c) - iv(k - k_c) + d(k - k_c)^2 + \dots, \quad (31)$$

is slightly different. Translating the critical eigenvalue into a differential operator leads to linear equations for A_l and A_r . The equation for A_l comes from the expansion about k_c and the equation for A_r comes from the expansion about $-k_c$,

$$\begin{aligned} \frac{\partial A_l}{\partial t} - v \frac{\partial A_l}{\partial x} &= \alpha(R - R_c) + d \frac{\partial^2 A_l}{\partial x^2} \\ \frac{\partial A_r}{\partial t} + v \frac{\partial A_r}{\partial x} &= \alpha(R - R_c) + d \frac{\partial^2 A_r}{\partial x^2}. \end{aligned} \quad (32)$$

These equations can be extended to nonlinear equations for solutions of the full PDE and the form of the equations is found again through symmetry considerations. Translation, $x \rightarrow x + \xi$, causes opposite phase shifts for the two envelopes,

$$(A_l, A_r) \rightarrow (e^{ik_c\xi} A_l, e^{-ik_c\xi} A_r). \quad (33)$$

Reflection, $x \rightarrow -x$, flips the envelopes,

$$(A_l, A_r) \rightarrow (A_r, A_l). \quad (34)$$

Since the basic patterns are time dependent and the original PDE is also time translation invariant, the invariance caused by $t \rightarrow t + \tau$ leads to

$$(A_l, A_r) \rightarrow (e^{i\omega_c\tau} A_l, e^{i\omega_c\tau} A_r). \quad (35)$$

The terms $(|A_l|^2 A_l, |A_r|^2 A_r)$ and $(|A_r|^2 A_l, |A_l|^2 A_r)$ are the only terms up to cubic order that are invariant under the operations (33)-(35) [20]. This leads to the nonlinear extension of (32) having the form

$$\begin{aligned} \frac{\partial A_l}{\partial t} - v \frac{\partial A_l}{\partial x} &= \alpha(R - R_c) + d \frac{\partial^2 A_l}{\partial x^2} + (a|A_l|^2 + b|A_r|^2)A_l \\ \frac{\partial A_r}{\partial t} + v \frac{\partial A_r}{\partial x} &= \alpha(R - R_c) + d \frac{\partial^2 A_r}{\partial x^2} + (a|A_r|^2 + b|A_l|^2)A_r \end{aligned} \quad (36)$$

with two complex coefficients a and b [27].

Unfortunately (36) can not be directly rescaled. Since if x is rescaled by $X = \epsilon x$, the first and second x -derivatives in (36) are of different orders. A way around this is to notice the terms on the left hand side are defined by first order wave operators. Because $\partial A/\partial t \mp v \partial A/\partial x = 0$ has the solution $A = f(x \pm vt)$, we can let $\xi_{\pm} = \epsilon(x/v \pm t)$ and $T = \epsilon^2 t$ which are of order ϵ . The expansions

$$\begin{aligned} A_l(t, x) &= \epsilon B_l(\xi_+, T) + \epsilon^2 C_l(\xi_+, \xi_-, T) + \dots \\ A_r(t, x) &= \epsilon B_r(\xi_-, T) + \epsilon^2 C_r(\xi_+, \xi_-, T) + \dots \end{aligned} \quad (37)$$

are then substituted into (36). Because of the first order of wave operators, the equations are automatically satisfied at order $O(\epsilon^2)$. At order $O(\epsilon^3)$, we have the equation

$$-2 \frac{\partial C_r}{\partial \xi_-} = -\frac{\partial B_l}{\partial T} + \Lambda B_l + D \frac{\partial^2 B_l}{\partial \xi_+^2} + (a|B_l|^2 + b|B_r|^2)B_l \quad (38)$$

with $\Lambda = \alpha(R - R_c)/\epsilon^2$ and $D = d/v^2$. The condition that this equation has a bounded solution, C_r , requires that the average on the right hand side vanishes. The argument for C_l is similar. The system of equations for B_l, B_r is then obtained as

$$\begin{aligned}\frac{\partial B_l}{\partial T} &= \left(\Lambda + D \frac{\partial^2}{\partial \xi_+^2} + a|B_l|^2 + b \langle |B_r(T, \zeta)|^2 \rangle \right) B_l \\ \frac{\partial B_r}{\partial T} &= \left(\Lambda + D \frac{\partial^2}{\partial \xi_-^2} + a|B_r|^2 + b \langle |B_l(T, \zeta)|^2 \rangle \right) B_r\end{aligned}\quad (39)$$

where the bracket denotes the average over ζ

$$\langle f(\zeta) \rangle = \lim_{L \rightarrow \infty} \frac{1}{2L} \int_{-L}^L f(\zeta) d\zeta. \quad (40)$$

The pair of equations (39) is the system of globally coupled Ginzburg Landau equations introduced by Knobloch and deLuca [27]. If spatial (ξ_+, ξ_-) dependence is ignored (39) reduces to the ODE-system

$$\begin{aligned}\frac{\partial B_l}{\partial T} &= (\Lambda + a|B_l|^2 + b|B_r|^2) B_l \\ \frac{\partial B_r}{\partial T} &= (\Lambda + a|B_r|^2 + b|B_l|^2) B_r.\end{aligned}\quad (41)$$

The system (41) is known as the normal form for a Hopf bifurcation with $O(2)$ -symmetry.

The non-transient solutions, for generic a, b , are of the form

- $(B_l, B_r) = B e^{i\Omega t} (1, 1)$ corresponding to standing waves and
- $B e^{i\Omega t} (1, 0)$ and $B e^{i\Omega t} (0, 1)$ corresponding to left and right traveling waves.

Substituting the solution ansatz into (41) gives the frequency Ω and the amplitude B . In the framework of the ODE-system (41), the stability of these solutions can be classified in terms of the real parts of a and b [27].

2.3 Derivation of the Two-Dimensional Ginzburg-Landau Equations

In what follows we will describe the derivation of the globally coupled Ginzburg Landau equations in two dimensions for an extended system that is reflection invariant about the x - and y -axis. We start by looking at the Hopf bifurcation for the PDE (18) in a three dimensional layer,

$$\mathbf{x} = (x, y, z), \quad -\infty < x, y < \infty, \quad 0 < z < d. \quad (42)$$

Now we assume that (18) is reflection invariant about the x - and y -axes and anisotropic (i.e. not rotationally invariant).

The Fourier transformed eigenvalue problem for the linearized PDE is

$$L(i\mathbf{k}, \partial_z, R)U_{\mathbf{k}} = \sigma U_{\mathbf{k}} \quad (43)$$

and depends on two horizontal wave numbers $\mathbf{k} = (p, q)$. As in the previous one dimensional Hopf bifurcation case, we assume there is a complex critical eigenvalue

$$\sigma(p, q, R) = \sigma_r(p, q, R) + i\omega(p, q, R). \quad (44)$$

The neutral stability surface $R = R_h(p, q)$ in the three dimensional (p, q, R) -space is defined by $\sigma_r(p, q, R) = 0$. Suppose $\sigma_r < 0$ for $R < R_h$ and $R_h(p, q)$ has a minimum R_c which identifies the onset of instability of the basic state. Because the system has two reflection invariances, the p -axis and q -axis are symmetry axes of the neutral stability surface $R = R_h$. Also, the minimum is either at the origin, on a symmetry axis, or off both symmetry axes. We will consider only the case where the minimum is not on a symmetry axis. Thus, there are four minima at $(\pm p_c, \pm q_c)$ with p_c, q_c both nonzero because of the reflection invariances.

The derivation of the Ginzburg Landau equations is similar to the one dimensional case. The linearized system has four traveling wave solutions in four oblique directions when $R = R_c$. Thus the solution slightly above the instability threshold, R_c , can be represented

as

$$U(t, \mathbf{x}) = e^{i\omega_c t} \left(A_1(t, x, y)e^{i(p_c x + q_c y)} + A_2(t, x, y)e^{i(-p_c x + q_c y)} + \right. \\ \left. A_3(t, x, y)e^{i(-p_c x - q_c y)} + A_4(t, x, y)e^{i(p_c x - q_c y)} \right) U_c(z) + cc \quad (45)$$

with four slowly varying complex envelopes A_1, A_2, A_3, A_4 [14]. In order to find the form of the linear part of the equations for these envelopes, the critical eigenvalue is expanded about (p_c, q_c, R_c) ,

$$\sigma(p, q, R) = i\omega_0 + \alpha(R - R_c) + iv_x \delta p + iv_y \delta q + d_{20} \delta p^2 + d_{11} \delta p \delta q + d_{02} \delta q^2 + \dots \quad (46)$$

where $\delta p = p - p_c$ and $\delta q = q - q_c$. The parameters, $\alpha, d_{20}, d_{11}, d_{02}$, are usually complex but the two critical group velocities are real. Translating the expansion of σ about (p_c, q_c) into a differential operator in physical space leads to the linear part of the equation for A_1 .

The symmetry invariance of the original system is used to determine the nonlinear terms. Translations of x, y, t and reflections of x, y induce the following operations on the envelopes in two dimensions

- $x \rightarrow x + \xi$: $(A_1, A_2, A_3, A_4) \rightarrow (e^{ip_c \xi} A_1, e^{-ip_c \xi} A_2, e^{-ip_c \xi} A_3, e^{ip_c \xi} A_4)$,
- $y \rightarrow y + \eta$: $(A_1, A_2, A_3, A_4) \rightarrow (e^{iq_c \eta} A_1, e^{iq_c \eta} A_2, e^{-iq_c \eta} A_3, e^{-iq_c \eta} A_4)$,
- $t \rightarrow t + \tau$: $(A_1, A_2, A_3, A_4) \rightarrow e^{i\omega_c \tau} (A_1, A_2, A_3, A_4)$,
- $x \rightarrow -x$: $(A_1, A_2, A_3, A_4) \rightarrow (A_2, A_1, A_4, A_3)$, and
- $y \rightarrow -y$: $(A_1, A_2, A_3, A_4) \rightarrow (A_4, A_3, A_2, A_1)$.

There are five independent cubic terms and no quadratic terms which are invariant under these operations.

Combining the linear part taken from the expansion of σ with the nonlinear terms found using symmetry considerations leads to the equation for A_1 becoming

$$\frac{\partial A_1}{\partial t} - v_x \frac{\partial A_1}{\partial x} - v_y \frac{\partial A_1}{\partial y} = \left(\lambda + d_{20} \frac{\partial^2}{\partial x^2} + d_{11} \frac{\partial^2}{\partial x \partial y} + d_{02} \frac{\partial^2}{\partial y^2} + \sum_{i=1}^4 a_i |A_i|^2 \right) A_1 + a_5 A_2 \bar{A}_3 A_4. \quad (47)$$

Applying the reflections $(x, y) \rightarrow (-x, y)$, $(x, y) \rightarrow (-x, -y)$, and $(x, y) \rightarrow (x, -y)$ to equation (47) gives the equations for A_2, A_3, A_4 respectively [14].

Since equation (47) involves first and second order spatial derivatives, we need to note that the first order derivative terms form the spatial part of a first order wave operator applied to A_1 . This leads to again introducing slowly varying wave variables

$$\xi_{\pm} = \epsilon \left(\frac{x}{v_x} \pm t \right), \quad \eta_{\pm} = \epsilon \left(\frac{y}{v_y} \pm t \right) \quad (48)$$

and the time $T = \epsilon^2 t$ to deal with the wave operator. These variables are related by

$$\xi_+ + \xi_- = \eta_+ + \eta_- = \epsilon t, \quad (49)$$

thus they are not independent.

The expanded version of $A_1(t, x, y)$ is

$$A_1(t, x, y) = \epsilon B_1(T, \xi_+, \eta_+) + \epsilon^2 C_1(T, \xi_+, \eta_+, \xi_-) + \dots \quad (50)$$

The equations for A_2, A_3, A_4 are similarly expanded with

$$B_2 = B_2(T, \xi_+, \eta_-), \quad B_3 = B_3(T, \xi_-, \eta_-), \quad B_4 = B_4(T, \xi_-, \eta_+). \quad (51)$$

Substituting these expansions into (47) yields an equation of the form

$$-2 \frac{\partial C_1}{\partial \xi_-} = F(A_1, A_2, A_3, A_4). \quad (52)$$

Since C_1 must be bounded the average of F with respect to ξ_- needs to vanish, which leads to an equation for B_1 . Finding equations for B_2, B_3, B_4 from the expansion for A_2, A_3, A_4 is similar. The explicit form of the resulting coupled system is

$$\begin{aligned} \frac{\partial B_1}{\partial T} &= (\Lambda + \mathcal{D}(\partial_{\xi_+}, \partial_{\eta_+}) + a_1 |B_1|^2 + a_2 \langle |B_2(T, \zeta, \eta_+)|^2 \rangle \\ &\quad + a_3 \langle |B_3(T, \zeta - \xi_+, \zeta - \eta_+)|^2 \rangle + a_4 \langle |B_4(T, \xi_+, \zeta)|^2 \rangle) B_1 \\ &\quad + a_5 \langle B_2(T, \zeta - \xi_+, \eta_+) \bar{B}_3(T, \zeta - \xi_+, \zeta - \eta_+) B_4(T, \xi_+, \zeta - \eta_+) \rangle, \\ \frac{\partial B_2}{\partial T} &= (\Lambda + \mathcal{D}(\partial_{\xi_-}, \partial_{\eta_+}) + a_1 |B_2|^2 + a_2 \langle |B_1(T, \zeta, \eta_+)|^2 \rangle \\ &\quad + a_3 \langle |B_4(T, \zeta - \xi_-, \zeta - \eta_+)|^2 \rangle + a_4 \langle |B_3(T, \xi_-, \zeta)|^2 \rangle) B_2 \\ &\quad + a_5 \langle B_1(T, \zeta - \xi_-, \eta_+) \bar{B}_4(T, \zeta - \xi_-, \zeta - \eta_+) B_3(T, \xi_-, \zeta - \eta_+) \rangle, \\ \frac{\partial B_3}{\partial T} &= (\Lambda + \mathcal{D}(\partial_{\xi_-}, \partial_{\eta_-}) + a_1 |B_3|^2 + a_2 \langle |B_4(T, \zeta, \eta_-)|^2 \rangle \\ &\quad + a_3 \langle |B_1(T, \zeta - \xi_-, \zeta - \eta_-)|^2 \rangle + a_4 \langle |B_2(T, \xi_-, \zeta)|^2 \rangle) B_3 \\ &\quad + a_5 \langle B_4(T, \zeta - \xi_-, \eta_-) \bar{B}_1(T, \zeta - \xi_-, \zeta - \eta_-) B_2(T, \xi_-, \zeta - \eta_-) \rangle, \\ \frac{\partial B_4}{\partial T} &= (\Lambda + \mathcal{D}(\partial_{\xi_+}, \partial_{\eta_-}) + a_1 |B_4|^2 + a_2 \langle |B_3(T, \zeta, \eta_-)|^2 \rangle \\ &\quad + a_3 \langle |B_2(T, \zeta - \xi_+, \zeta - \eta_-)|^2 \rangle + a_4 \langle |B_1(T, \xi_+, \zeta)|^2 \rangle) B_4 \\ &\quad + a_5 \langle B_3(T, \zeta - \xi_+, \eta_-) \bar{B}_2(T, \zeta - \xi_+, \zeta - \eta_-) B_1(T, \xi_+, \zeta - \eta_-) \rangle. \end{aligned} \quad (53)$$

The second order differential operator, \mathcal{D} , is defined by

$$\mathcal{D}(\partial_\xi, \partial_\eta) = D_{20} \partial_\xi^2 + D_{11} \partial_x i \partial_\eta + D_{02} \partial_\eta^2 \quad (54)$$

Table 1: Different patterns of solutions.

Name	Description	(B_1, B_2, B_3, B_4)
<i>TW</i>	oblique traveling wave	$Be^{i\Omega t}(1, 0, 0, 0)$
<i>TR_y</i>	traveling rectangle in the <i>y</i> -direction	$Be^{i\Omega t}(1, 1, 0, 0)$
<i>TR_x</i>	traveling rectangle in the <i>x</i> -direction	$Be^{i\Omega t}(1, 0, 0, 1)$
<i>SW</i>	oblique standing wave	$Be^{i\Omega t}(1, 0, 1, 0)$
<i>SR</i>	standing rectangle	$Be^{i\Omega t}(1, 1, 1, 1)$
<i>AW</i>	alternating wave	$Be^{i\Omega t}(1, i, 1, i)$

with rescaled coefficients

$$D_{20} = \frac{d_{20}}{v_x^2}, \quad D_{11} = \frac{d_{11}}{v_x v_y}, \quad D_{02} = \frac{d_{02}}{v_y^2}. \quad (55)$$

The brackets denotes the average with respect to ζ as before.

Ignoring the dependence on the wave variables reduces (53) to the ODE-system

$$\begin{aligned} \frac{dB_1}{dT} &= (\Lambda + a_1|B_1|^2 + a_2|B_2|^2 + a_3|B_3|^2 + a_4|B_4|^2) + a_5 B_2 \bar{B}_3 B_4, \\ \frac{dB_2}{dT} &= (\Lambda + a_1|B_2|^2 + a_2|B_1|^2 + a_3|B_4|^2 + a_4|B_3|^2) + a_5 B_1 \bar{B}_4 B_3, \\ \frac{dB_3}{dT} &= (\Lambda + a_1|B_3|^2 + a_2|B_4|^2 + a_3|B_1|^2 + a_4|B_2|^2) + a_5 B_4 \bar{B}_1 B_2, \\ \frac{dB_4}{dT} &= (\Lambda + a_1|B_4|^2 + a_2|B_3|^2 + a_3|B_2|^2 + a_4|B_1|^2) + a_5 B_3 \bar{B}_2 B_1. \end{aligned} \quad (56)$$

The system (56) is referred to as the normal form for a Hopf bifurcation with $O(2) \times O(2)$ -symmetry. It has been studied in [38, 42, 29]. For generic values of the coefficients (56), it has the six basic non-transient types of solutions in the Table 1. The frequency Ω and the amplitude B follow by substituting the solution into (56) and the stability can be classified in terms of the coefficients a_i .

2.4 Globally Coupled Ginzburg-Landau Equations for the WEM

The constitutive equations which form the weak electrolyte model (WEM) are derived from the Navier-Stokes equation for an anisotropic electrically conduction fluid, the conser-

vation of charge, Poisson's law, and a partial differential equation for the conductivity [32]. A weakly nonlinear analysis at the onset is particularly useful since the WEM equations for a fully three-dimensional numerical simulation are complicated [32].

The superposition of oblique-steady and normal-traveling modes represented by

$$\begin{aligned} \mathbf{u}(t, x, y, z) = & \epsilon(Ae^{ip_{sc}x}U_{s+}(z) + Be^{-ip_{sc}x}U_{s-}(z))e^{iq_{sc}y} + \\ & \epsilon(Ce^{ip_{oc}x}U_{o+}(z) + De^{-ip_{oc}x}U_{o-}(z))e^{i\omega_{Hc}t} + cc + O(\epsilon^2) \end{aligned} \quad (57)$$

describes the dynamics of patterns above threshold. The field variables of the WEM (velocities, electric potential, director, conductivity) are represented by \mathbf{u} , ϵ is a small parameter such that $\epsilon^2 \sim |V/V_c - 1|$, $U_{s\pm}(z)$ and $U_{o\pm}(z)$ are vertical critical modes, and cc is the complex conjugate expression [32]. The slowly varying complex envelopes of the oblique-stationary (OS) rolls, A and B , and the counter-propagating normal traveling (NT) rolls, C and D , are functions of a slow time $T = \epsilon^2 t$ and slow space variables. The amplitudes A and B depend on $(\xi, \eta) = (\epsilon x, \epsilon y)$. The amplitudes C and D depend on (ξ_+, η) and (ξ_-, η) when $\xi_{\pm} = \epsilon(x \pm v_c t)$ where v_c is the critical group velocity derived from the oscillatory neutral surface at criticality [32].

The main objective of this work is to study the system of four globally coupled complex Ginzburg-Landau equations introduced in [1] to model the steady-oblique/normal-Hopf interaction observed experimentally. The four equations are

$$\begin{aligned} A_T &= (\Lambda_1 + D(\partial_{\xi}, \partial_{\eta}) - |A|^2 - a|B|^2 + c \langle |C|^2 \rangle + \bar{c} \langle |D|^2 \rangle) A, \\ B_T &= (\Lambda_1 + D(-\partial_{\xi}, \partial_{\eta}) - |B|^2 - a|A|^2 + c \langle |D|^2 \rangle + \bar{c} \langle |C|^2 \rangle) B, \\ C_T &= (\Lambda_2 + i\Omega + D_0(\partial_{\xi_+}, \partial_{\eta}) - b_1|C|^2 - b_2|D|^2 + d \langle |A|^2 + |B|^2 \rangle) C, \\ D_T &= (\Lambda_2 + i\Omega + D_0(\partial_{\xi_-}, \partial_{\eta}) - b_1|D|^2 - b_2|C|^2 + d \langle |A|^2 + |B|^2 \rangle) D. \end{aligned} \quad (58)$$

The solutions of (58) are complex envelopes $A(T, \xi, \eta)$, $B(T, \xi, \eta)$, $C(T, \xi_+, \eta)$, and $D(T, \xi_-, \eta)$. For our numerical computation we chose periodic boundary conditions in (ξ, η) , (ξ_+, η) , (ξ_-, η) of periods L in both variables. The average which appears in (58) is

$$\langle |f|^2 \rangle = \frac{1}{L} \int_0^L |f|^2 d\tilde{\xi}, \quad (59)$$

where $\tilde{\xi} = \xi, \xi_+, \xi_-$. The coefficients are $a \in \mathbb{R}$, $a > 1$, $\Omega \in \mathbb{R}$, $b_1, b_2, c, d \in \mathbb{C}$, and $b_{2r} > b_{1r} > 0$ to match the experimental situation [1]. The diffusion operators are

$$\begin{aligned} D(\partial_\xi, \partial_\eta) &= \partial_\xi^2 + 2\delta\partial_\xi\partial_\eta + \partial_\eta^2 \\ D_0(\partial_{\xi_\pm}, \partial_\eta) &= \alpha\partial_{\xi_\pm}^2 + \beta\partial_\eta^2 \end{aligned} \quad (60)$$

with $\delta \in \mathbb{R}$ such that $\delta^2 < 1$ and $\alpha, \beta \in \mathbb{C}$, $\alpha_r, \beta_r > 0$. The $O(1)$ “unfolding parameters” describing the deviations of the external voltage, V , and the AC frequency, ω_0 , from the codimension-two point are

$$\Lambda_1 = \lambda - b_s\mu, \quad \Lambda_2 + i\Omega = a_0\lambda - b_0\mu, \quad (61)$$

where

$$\epsilon^2\lambda = \frac{V}{V_c} - 1, \quad \epsilon^2\mu = \frac{\omega_0}{\omega_{0c}} - 1, \quad (62)$$

with $b_s \in \mathbb{R}$ and $a_0, b_0 \in \mathbb{C}$. The patterns are generated by

$$\begin{aligned} U(t, x, y) &= A(\epsilon^2 t, \epsilon x, \epsilon y) e^{i(p_c x + q_c y)} + B(\epsilon^2 t, \epsilon x, \epsilon y) e^{i(-p_c x + q_c y)} + \\ &C(\epsilon^2 t, \epsilon(x + v_c t), \epsilon y) e^{i(w_c t + k_c x)} + D(\epsilon^2 t, \epsilon(x - v_c t), \epsilon y) e^{i(w_c t - k_c x)} + \\ &cc \end{aligned} \quad (63)$$

with $0 < \epsilon \ll 1$ and $v_c, p_c, q_c, k_c > 0$. We will pursue a theoretical and numerical study of the system (58) for appropriate values of the parameters as determined from the experimental situation and a normal form analysis of (58) (see Section 4.2).

3 Bifurcation Analysis of the Normal Form

3.1 Normal Form

If spatial variations are neglected the Ginzburg-Landau system (58) in section 2.4 becomes

$$\begin{aligned}
 A_T &= (\Lambda_1 - |A|^2 - a|B|^2 + c|C|^2 + \bar{c}|D|^2)A, \\
 B_T &= (\Lambda_1 - |B|^2 - a|A|^2 + c|D|^2 + \bar{c}|C|^2)B, \\
 C_T &= (\Lambda_2 + i\Omega - b_1|C|^2 - b_2|D|^2 + d|A|^2 + d|B|^2)C, \\
 D_T &= (\Lambda_2 + i\Omega - b_1|D|^2 - b_2|C|^2 + d|A|^2 + d|B|^2)D,
 \end{aligned} \tag{64}$$

where $a \in \mathbb{R}$, $a > 1$, $\Omega \in \mathbb{R}$, $b_1, b_2, c, d \in \mathbb{C}$ with $b_{2r} > b_{1r} > 0$, and Λ_1 and Λ_2 as defined in (61) with $b_s \in \mathbb{R}$ and $a_0, b_0 \in \mathbb{C}$.

The system (64) has the following symmetries that follow by applying translations and reflections to (57):

- (i) Assuming that p_{sc}/p_{oc} is irrational, the translations $x \rightarrow x + x_0$ induce the phase shift invariances $(A, B, C, D) \rightarrow (Ae^{i\theta_1}, Be^{-i\theta_1}, Ce^{i\theta_2}, De^{-i\theta_2})$ with arbitrary $(\theta_1, \theta_2) \in [0, 2\pi) \times [0, 2\pi)$.
- (ii) The translations $y \rightarrow y + y_0$ induce the invariance $(A, B, C, D) \rightarrow (Be^{i\theta_3}, Ae^{i\theta_3}, C, D)$ with arbitrary $\theta_3 \in [0, 2\pi)$.
- (iii) The reflection $x \rightarrow -x$ induces the invariance under $(A, B, C, D) \rightarrow (B, A, D, C)$.
- (iv) The reflection $y \rightarrow -y$ induces the invariance under $(A, B, C, D) \rightarrow (\bar{A}, \bar{B}, C, D)$.
- (v) The time translation $\tau \rightarrow \tau + \tau_0$ induces the phase shift invariance $(A, B, C, D) \rightarrow (A, B, Ce^{i\theta_4}, De^{i\theta_4})$ with arbitrary $\theta_4 \in [0, 2\pi)$.

A consequence of the phase shift symmetries is that the radial parts decouple from the phases. Rewriting (64) in polar form with $A = \rho_A e^{i\psi_A}$ and likewise for B , C , and D leads to

$$\begin{aligned}
(\rho_A)_T &= (\Lambda_1 - \rho_A^2 - a\rho_B^2 + c_r\rho_C^2 + c_r\rho_D^2)\rho_A, \\
(\rho_B)_T &= (\Lambda_1 - \rho_B^2 - a\rho_A^2 + c_r\rho_D^2 + c_r\rho_C^2)\rho_B, \\
(\rho_C)_T &= (\Lambda_2 - b_{1r}\rho_C^2 - b_{2r}\rho_D^2 + d_r\rho_A^2 + d_r\rho_B^2)\rho_C, \\
(\rho_D)_T &= (\Lambda_2 - b_{1r}\rho_D^2 - b_{2r}\rho_C^2 + d_r\rho_A^2 + d_r\rho_B^2)\rho_D
\end{aligned} \tag{65}$$

and

$$\begin{aligned}
(\psi_A)_T &= c_i(\rho_C^2 - \rho_D^2), \\
(\psi_B)_T &= c_i(\rho_D^2 - \rho_C^2), \\
(\psi_C)_T &= \Omega - b_{1i}\rho_C^2 - b_{2i}\rho_D^2 + d_i\rho_A^2 + d_i\rho_B^2, \\
(\psi_D)_T &= \Omega - b_{1i}\rho_D^2 - b_{2i}\rho_C^2 + d_i\rho_A^2 + d_i\rho_B^2.
\end{aligned} \tag{66}$$

Possible patterns that could be observed in this system are steady oblique rolls (OS), stationary rectangles (RS), traveling waves (TW), and standing waves (SW).

If $C = D = 0$ or $A = B = 0$, the system (64) decouples as follows:

- $C = D = 0$ gives the ODE system for the steady-oblique solutions

$$\begin{aligned}
A_T &= (\Lambda_1 - |A|^2 - a|B|^2)A, \\
B_T &= (\Lambda_1 - |B|^2 - a|A|^2)B,
\end{aligned} \tag{67}$$

where $\Lambda_1, a \in \mathbb{R}$ and $a > 1$.

- $A = B = 0$ gives the ODE system for the normal-Hopf solutions

$$\begin{aligned} C_T &= (\Lambda_2 + i\Omega - b_1|C|^2 - b_2|D|^2)C, \\ D_T &= (\Lambda_2 + i\Omega - b_1|D|^2 - b_2|C|^2)D, \end{aligned} \tag{68}$$

where $\Lambda_2, \Omega \in \mathbb{R}$ and $b_1, b_2 \in \mathbb{C}$ with $b_{2r} > b_{1r} > 0$.

These decoupled systems are similar/identical to the amplitude equations found when looking at the Hopf bifurcation with $O(2)$ -symmetry in Couette-Taylor flow. The system (64) bears a marked similarity to the non-resonant case in [34, 31, 36] and the systems discussed in [38, 12]. For clarity in the comparisons below our parameters and coefficients will be underlined. The parameters and coefficients in the non-resonant case in [34, 31] are $\sigma, \mu, A, B, C, D, P, S, U, V$. By identifying $\sigma \rightarrow \underline{\Lambda}_1, \mu \rightarrow \underline{\Lambda}_2 + i\underline{\Omega}, A \rightarrow -1, B \rightarrow -\underline{a}, C \rightarrow \underline{c}, D \rightarrow \underline{\bar{c}}, P \rightarrow \underline{d}, S \rightarrow \underline{d}, U \rightarrow -\underline{b}_1, V \rightarrow -\underline{b}_2$ the non-resonant systems [34, 31] become identical to (64). The restriction to the non-resonant case in [36] is similar.

3.2 Bifurcation Diagrams

The trivial solution, basic conduction state, $A = B = C = D = 0$, is stable in the region where $\Lambda_1, \Lambda_2 < 0$. It loses stability in a bifurcation when $\Lambda_1 = 0, \Lambda_2 < 0$ and when $\Lambda_1 < 0, \Lambda_2 = 0$.

At $\Lambda_1 = 0$, two types of stationary solutions bifurcate from the trivial solution [1]. These two pure mode solutions are stationary oblique (OS) rolls and stationary rectangles (RS). Both solutions are fixed points of the systems (64) and (65) in Section 3.1. The OS rolls satisfy either ρ_A or ρ_B equal to $R_o > 0$ such that $R_o^2 = \Lambda_1$, and all other $\rho_i = 0$. The RS solution satisfies $\rho_A = \rho_B = R_{rs} > 0$, such that $R_{rs}^2 = \frac{\Lambda_1}{a+1}$, and $\rho_C = \rho_D = 0$. Only one of these solutions can be stable in a region of the (Λ_1, Λ_2) -plane.

In the case of the OS-solution, the Jacobian matrix for only ρ_A nonzero is

$$\begin{pmatrix} -2\Lambda_1 & 0 & 0 & 0 \\ 0 & \Lambda_1(1-a) & 0 & 0 \\ 0 & 0 & d\Lambda_1 + \Lambda_2 & 0 \\ 0 & 0 & 0 & d\Lambda_1 + \Lambda_2 \end{pmatrix}. \quad (69)$$

The eigenvalues determine that the conditions for the OS-solution to be stable are $a > 1$, $\Lambda_1 > 0$, and $\Lambda_2 < -d_r\Lambda_1$. The experiments support that $a > 1$ is a condition for the OS-solution to be stable. These conditions are for either ρ_A or ρ_B being the only nonzero radial part. The OS-solution exists for $\Lambda_1 > 0$ and transitions to instability on the half-line

$$(O) : d_r\Lambda_1 + \Lambda_2 = 0, \quad J(b_{1r}\Lambda_1 + c_r\Lambda_2) \geq 0 \quad (70)$$

where $J = b_{1r} - c_r d_r$. If $d_r < 0$, (O) is in the first quadrant and if $d_r > 0$, (O) is in the fourth quadrant.

The RS-solution has the Jacobian matrix

$$\begin{pmatrix} \frac{-2\Lambda_1}{a+1} & \frac{-2a\Lambda_1}{a+1} & 0 & 0 \\ \frac{-2a\Lambda_1}{a+1} & \frac{-2\Lambda_1}{a+1} & 0 & 0 \\ 0 & 0 & \frac{2d\Lambda_1}{a+1} + \Lambda_2 & 0 \\ 0 & 0 & 0 & \frac{2d\Lambda_1}{a+1} + \Lambda_2 \end{pmatrix} \quad (71)$$

with associated eigenvalues $\frac{2\Lambda_1(a-1)}{a+1}$, $-2\Lambda_1$, $\frac{2d\Lambda_1}{a+1} + \Lambda_2$, and $\frac{2d\Lambda_1}{a+1} + \Lambda_2$, leading to the stability conditions being $\Lambda_1 > 0$, $-1 < a < 1$, and $\Lambda_2(a+1) < -2d_r\Lambda_1$.

At $\Lambda_2 = 0$, two types of oscillatory solutions bifurcate from the trivial solution. These two pure mode solutions are normal traveling (NT) rolls and standing waves (SW). Both solutions are fixed points of the system (65) and periodic solutions of the system (64). The NT rolls satisfy either ρ_C or ρ_D equal to $R_n > 0$ such that $R_n^2 = \frac{\Lambda_2}{b_{1r}}$, and all other $\rho_i = 0$.

The SW solution satisfies $\rho_C = \rho_D = R_{sw} > 0$, such that $R_{sw}^2 = \frac{\Lambda_2}{b_{1r} + b_{2r}}$, and $\rho_A = \rho_B = 0$. Again, only one of these solutions can be stable in a region of the (Λ_1, Λ_2) -plane. In the case of the NT-solution, the Jacobian matrix for only ρ_C nonzero is

$$\begin{pmatrix} \Lambda_1 + \frac{c_r \Lambda_2}{b_{1r}} & 0 & 0 & 0 \\ 0 & \Lambda_1 + \frac{c_r \Lambda_2}{b_{1r}} & 0 & 0 \\ 0 & 0 & -2\Lambda_2 & 0 \\ 0 & 0 & 0 & \Lambda_2 \left(1 - \frac{b_{2r}}{b_{1r}}\right) \end{pmatrix}. \quad (72)$$

The eigenvalues that determine the conditions for the NT-solution to be stable are $0 < b_{1r} < b_{2r}$, $\Lambda_2 > 0$, and $\Lambda_1 < -\frac{c_r}{b_{1r}}\Lambda_2$. These conditions are for either ρ_C or ρ_D being the only nonzero radial part. The NT-solution exists for $\Lambda_2 > 0$ and transition to instability on the half-line

$$(N) : b_{1r}\Lambda_1 + c_r\Lambda_2 = 0, \quad J(d_r\Lambda_1 + \Lambda_2) \geq 0. \quad (73)$$

If $c_r < 0$, (N) is in the first quadrant and if $c_r > 0$, (N) is in the second quadrant.

The SW-solution has the Jacobian matrix

$$\begin{pmatrix} \Lambda_1 + \frac{2c_r\Lambda_2}{b_{1r} + b_{2r}} & 0 & 0 & 0 \\ 0 & \Lambda_1 + \frac{2c_r\Lambda_2}{b_{1r} + b_{2r}} & 0 & 0 \\ 0 & 0 & \frac{-2b_{1r}\Lambda_2}{b_{1r} + b_{2r}} & \frac{-2b_{2r}\Lambda_2}{b_{1r} + b_{2r}} \\ 0 & 0 & \frac{-2b_{2r}\Lambda_2}{b_{1r} + b_{2r}} & \frac{-2b_{1r}\Lambda_2}{b_{1r} + b_{2r}} \end{pmatrix} \quad (74)$$

with associated eigenvalues $\Lambda_1 + \frac{2c_r\Lambda_2}{b_{1r} + b_{2r}}$, $\Lambda_1 + \frac{2c_r\Lambda_2}{b_{1r} + b_{2r}}$, $\frac{2\Lambda_2(b_{2r} - b_{1r})}{b_{1r} + b_{2r}}$, and $-2\Lambda_2$, leading to the stability conditions being $\Lambda_2 > 0$, $|b_{2r}| < |b_{1r}|$, and $\Lambda_1 < -\frac{2c_r\Lambda_2}{b_{1r} + b_{2r}}$.

The mixed mode (MM) solutions branch off primary solutions in secondary bifurcations. There are four possible mixed mode solutions consisting of a primary stationary solution and a primary oscillatory solution. Using parameter restrictions we limit ourselves to the case of a superposition of OS and NT. The relevant parameters satisfy ρ_A or ρ_B nonzero and equal

to $R_o > 0$, $R_o^2 = \frac{b_{1r}\Lambda_1 + c_r\Lambda_2}{J}$, and ρ_C or ρ_D nonzero and equal to $R_n > 0$, $R_n^2 = \frac{d_r\Lambda_1 + \Lambda_2}{J}$. All combinations of two modes which result in a mixed mode solution have the same stability conditions. MM solutions are quasiperiodic solutions of the equation (64), because as seen in the phase equations

$$\begin{aligned} (\varphi_A)_T &= c_i(\rho_C^2 - \rho_D^2), \\ (\varphi_C)_T &= \Omega - b_{1i}\rho_C^2 - b_{2i}\rho_D^2 + d_i(\rho_A^2 + \rho_B^2) \end{aligned} \quad (75)$$

there are two nonzero frequencies. The two half-lines (70) and (73) define a wedge in the (Λ_1, Λ_2) -plane where the MM solution exists, as seen in figures (12). The MM solution is stable if $J > 0$ and unstable if $J < 0$.

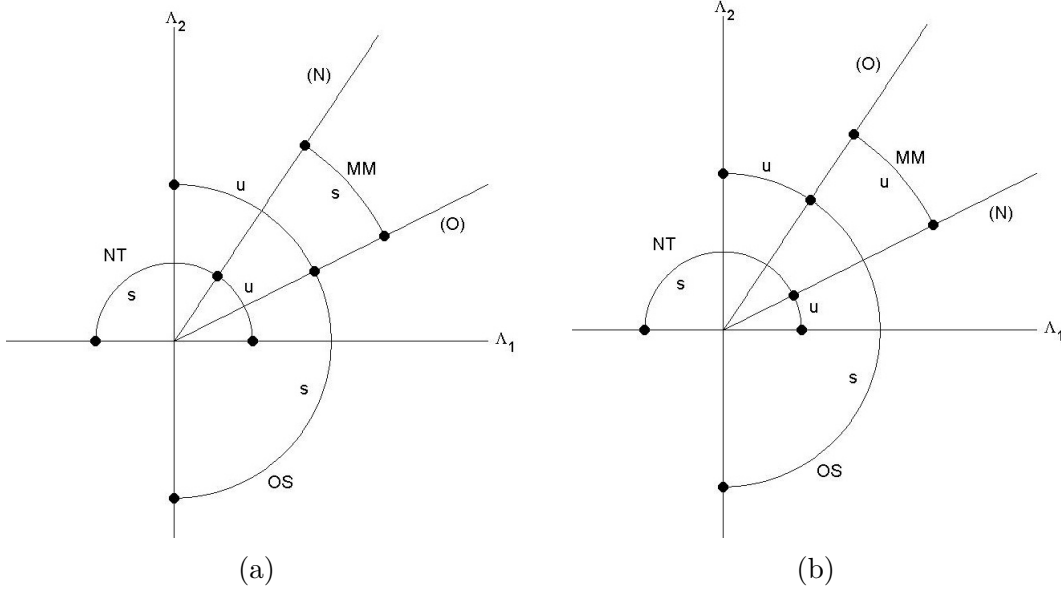


Figure 12: (a) MM solution is stable in the wedge. (b) MM solution is unstable in the wedge.

The stability diagrams (Figure 12) in the (Λ_1, Λ_2) -plane for the cases $J > 0$ and $J < 0$, with both $c_r < 0$ and $d_r < 0$ summarize the existence and stability of the OS, NT, and MM solutions. The existence domains are indicated by circle-segments, and the dots on these segments separate regions in which the solution is stable (s) and unstable (u). The trivial

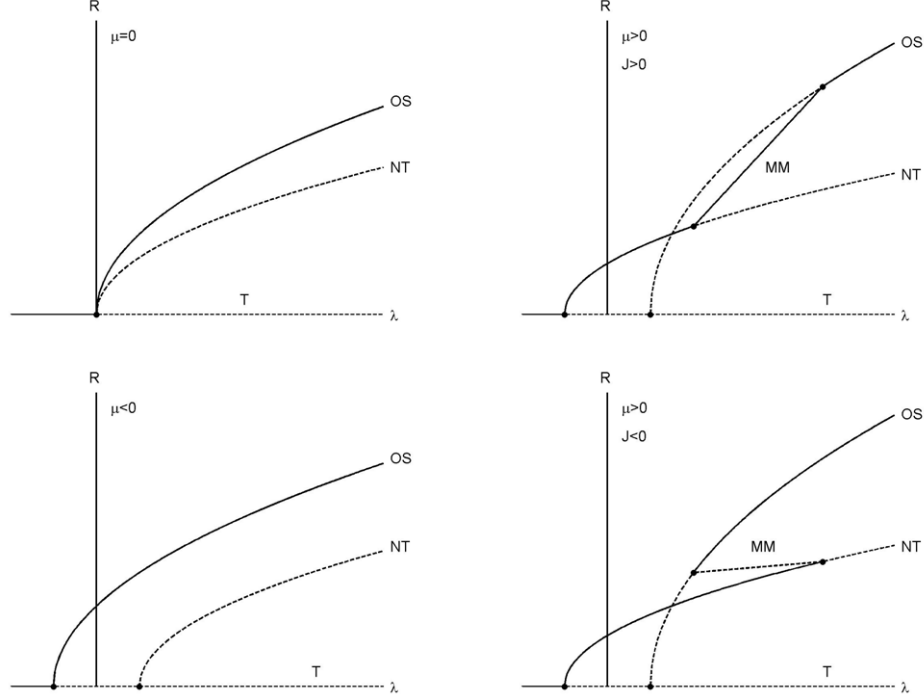


Figure 13: Bifurcation diagrams of OS, NT, and MM for $\mu = 0$, $\mu < 0$, and $\mu > 0$ with $J < 0$ and $J > 0$ and $b_{1r} > a_{0r}$.

solution is stable in the third quadrant. The primary bifurcation occur along the axes, and the secondary bifurcations occur along (70) and (73).

For $\mu = 0$, as the parameters increase from below criticality to above criticality we are traversing a straight path from the third quadrant, through the origin (mode-interaction point), to the first quadrant. This path is below the wedge in which MM exists if

$$J > 0, d_r < 0, 0 < a_{or} < -d_r, \quad (76)$$

or

$$J < 0, c_r < 0, 0 < a_{or} < -b_{1r}/c_r. \quad (77)$$

Bifurcation diagrams in the (λ, R) plane are shown for this path and the cases where $\mu < 0$ and $\mu > 0$ with $J > 0$ and $J < 0$, and $a_{or}b_s - b_{or} > 0$ in Figure 13. Stable branches are displayed as solid lines and unstable are dashed lines in the diagrams and the MM-branch

has been sketched as a straight line for simplicity. For all four diagrams, $b_{1r} > a_{or}$ leads to an intersection of the OS and NT branches for $\mu > 0$, however this does not imply a stability exchange. When $J > 0$, we have a continuous transition of stable branches, NT→MM→OS. However, for $J < 0$ we find bistability leading to hysteresis.

When the perturbed path for $\mu > 0$ crosses the (*O*) and (*N*) half-lines, the stability of the primary branches changes. These stability exchanges are combined with secondary bifurcations of MM, which connects the two bifurcation diagrams, as in the right panels of Figure 13. The amplitude R along MM is $R = \sqrt{R_o^2 + R_n^2}$. The experimental observations support the bifurcation scenarios, since in the NT-regime the OS-rolls reappear when V is further increased above the V_{oc} -threshold.

The derivation of the system of globally coupled Ginzburg Landau equations governing the dynamics of slowly varying spatiotemporal envelopes of ideal rolls patterns in anisotropic systems near the experimentally observed codimension-two point was one result of the qualitative theoretical study in [1]. Another result is the identification of the primary solution branches, their stability, and the regions in parameter space giving rise to superpositions of these solutions (mixed mode solutions) in the context of an idealized normal form description restricted to spatially uniform envelopes of ideal parameters. An important feature of the bifurcation diagrams is how the transition between two primary branches happens. Either it is a continuous transition via a stable mixed mode branch or a region with bistability and an unstable mixed mode branch leading to a hysteretic transition. The experiments do not yet provide evidence which of the two scenarios is present in the physical system. Further experiments and a thorough analysis of the recorded patterns is necessary to discriminate between the two scenarios. The next step in the theoretical analysis of the mode interaction is a numerical study of the patterns predicted by the globally coupled Ginzburg Landau equations. The two normal form scenarios described lead to somewhat different spatiotemporal patterns which will hopefully provide further criteria allowing to distinguish between them in experiments.

4 Numerical Simulations

A pseudo-spectral based code was used to simulate the globally coupled complex Ginzburg-Landau equations. The Pseudo-Spectral Method has the same underlying principles as the spectral method with regards to an orthonormal set of basis functions. The primary difference is the space in which the components of the resulting system are evaluated. The spectral method maps the PDE into Fourier space and computes the basis coefficients in this space [3]. This works well for linear partial differential equations. Many of the PDEs that occur naturally have nonlinear terms, which causes the loss of the superposition principle for solutions. The pseudo-spectral method can be applied to such problems by evaluating the linear terms in Fourier space as in the spectral method, but using collocation where the nonlinear terms are evaluated in real space and the result is transformed into Fourier space using a discrete Fourier transform. This results in multiple transformations between real and Fourier space and a technique such as the fast Fourier transform (FFT) is useful.

For problems with periodic boundary conditions and smooth solutions such as wave problems the pseudo-spectral method is particularly attractive. It is one of the most common techniques for solving the Ginzburg-Landau equations in one or two dimensions. The convergence of this method in one dimension was proved by Yisong Yang, [44], where the rate of convergence was shown to depend on the smoothness of the initial data.

In this work Matlab's routine ODE45, a fourth order Runge-Kutta method with variable time step, was used in time while a pseudo-spectral based method was used in space. The use of the spectral method is attractive since the functions are two-periodic and the spatial derivatives can then be turned into scalar multiplication of the Fourier coefficients.

There were M^2 Fourier modes used in the simulation. Four $M \times M$ random, complex matrices in physical space were used as the initial condition, one for each amplitude (A, B, C, D). A new set of random matrices were generated for each run of the simulation. Next, each

of the four grid point values were converted into Fourier modes through a two-dimensional Fourier transform. Each matrix was then vectorized by taking each column and adjoining it to the bottom of a growing column vector. Then the amplitude vectors were adjoined into a single column vector by adjoining the A, B, C, D vectors together in this order. This is done because ODE45 only takes in a vector. The intermediate calculations were done by reconstituting the four $M \times M$ matrices as much as necessary. The Fourier mode matrix was used to calculate the linear and derivative terms via scalar multiplication and scalar addition. The computation of the nonlinear terms was done in physical space by taking the Fourier mode matrices and calculating a two-dimensional inverse Fourier transform. These terms simplify to scalar multiplication at grid points in physical space. The average term is a sum across the rows divided by $2M$ with the resulting vector adjoined with itself appropriately to give a $M \times M$ matrix. The nonlinear terms are then summed and transformed back into Fourier space and added to the linear and derivative terms. Then the matrices are revectorized as before and fed into the ODE45 solver for the next step. A final two-dimensional inverse Fourier transform returns the amplitudes to real space. The visualization of the pattern took the resulting amplitudes and set them up according to the pattern equation (63).

4.1 Numerical Implementation

In order to apply the Spectral Method to our Ginzburg-Landau Equations, assume that A can be written as

$$A(\xi, \eta) = \sum_{k=1}^N \sum_{j=1}^N a_{kj} e^{c_k \xi + c_j \eta} \quad (78)$$

where $c_\alpha = \frac{-2\pi i(\alpha - M - 1)}{L}$ and $N = 2M + 1$, and similarly for B, C , and D . Then define the Fourier projection onto the space spanned by the mode $e^{c_k \xi + c_k \eta}$ as

$$T_F^{(kj)}[g(\xi, \eta)] = \frac{1}{L^2} \int_0^L \int_0^L g(\xi, \eta) e^{c_k \xi + c_k \eta} d\xi d\eta. \quad (79)$$

The linear term in the equation for A becomes

$$\begin{aligned}
& T_F^{(kj)}[(\Lambda_1 + \partial_\xi^2 + 2\delta\partial_\xi\partial_\eta + \partial_\eta^2)A] \\
&= \frac{1}{L^2} \int_0^L \int_0^L \sum_{\alpha=1}^N \sum_{\beta=1}^N (\Lambda_1 + c_\alpha^2 + 2\delta c_\alpha c_\beta + c_\beta^2) A_{\alpha\beta} e^{c_\alpha\xi + c_\beta\eta} e^{-c_k\xi - c_j\eta} d\xi d\eta \\
&= (\Lambda_1 + c_k^2 + 2\delta c_k c_j + c_j^2) a_{kj}
\end{aligned} \tag{80}$$

and

$$T_F^{(kj)}\left[\frac{\partial A}{\partial T}\right] = \dot{A}_{kj} \tag{81}$$

where the differentiation is assumed to be with respect to T . The linear terms in the equations for B , C , and D are similar.

If we were to continue with a spectral method for the nonlinear terms of the amplitude equation we would be forced to do multiple nested loops such as those described in the following. A nonlinear term in the equation for A becomes

$$\begin{aligned}
& T_F^{(kj)}[|B|^2 A] \\
&= \frac{1}{L^2} \int_0^L \int_0^L \left(\sum_{\alpha=1}^N \sum_{\beta=1}^N \sum_{\gamma=1}^N \sum_{\rho=1}^N \sum_{m=1}^N \sum_{n=1}^N B_{\alpha\beta} \overline{B_{\gamma\rho}} A_{mn} e^{(c_\alpha - c_\gamma + c_m)\xi} e^{(c_\beta - c_\rho + c_n)\eta} \right) e^{-c_k\xi - c_j\eta} d\xi d\eta \\
&= \sum_{\alpha=1}^N \sum_{\beta=1}^N \sum_{\gamma=1}^N \sum_{\rho=1}^N B_{\alpha\beta} \overline{B_{\gamma\rho}} A_{mn}
\end{aligned} \tag{82}$$

where $m = k + \gamma - \alpha$ and $n = j + \rho - \beta$. Similarly, the other nonlinear term becomes

$$T_F^{(kj)}[|A|^2 A] = \sum_{\alpha=1}^N \sum_{\beta=1}^N \sum_{\gamma=1}^N \sum_{\rho=1}^N A_{\alpha\beta} \overline{A_{\gamma\rho}} A_{mn} \tag{83}$$

where $m = k + \gamma - \alpha$ and $n = j + \rho - \beta$.

The average in the global term in the equation for A becomes

$$\begin{aligned}
\langle |C|^2 \rangle &= \frac{1}{L} \int_0^L \sum_{\alpha=1}^N \sum_{\beta=1}^N \sum_{\gamma=1}^N \sum_{\rho=1}^N C_{\alpha\beta} e^{c_\alpha \xi + c_\beta \eta} \overline{C_{\gamma\rho}} e^{-(c_\gamma \xi + c_\rho \eta)} d\xi \\
&= \sum_{\alpha=1}^N \sum_{\beta=1}^N \sum_{\rho=1}^N C_{\alpha\beta} \overline{C_{\alpha\rho}} e^{(c_\beta - c_\rho) \eta},
\end{aligned} \tag{84}$$

resulting in

$$\begin{aligned}
&T_F^{(kj)}[\langle |C|^2 \rangle > A] \\
&= \frac{1}{L^2} \int_0^L \int_0^L \left(\sum_{\alpha=1}^N \sum_{\beta=1}^N \sum_{\rho=1}^N C_{\alpha\beta} \overline{C_{\alpha\rho}} e^{(c_\beta - c_\rho) \eta} \right) \left(\sum_{m=1}^N \sum_{n=1}^N A_{mn} e^{c_m \xi + c_n} \right) e^{-c_k \xi - c_j \eta} d\xi d\eta \\
&= \sum_{\alpha=1}^N \sum_{\beta=1}^N \sum_{\rho=1}^N C_{\alpha\beta} \overline{C_{\alpha\rho}} A_{kn}
\end{aligned} \tag{85}$$

where $m = k$ and $n = j + \rho - \beta$. Similarly,

$$T_F^{(kj)}[\langle |D|^2 \rangle > A] = \sum_{\alpha=1}^N \sum_{\beta=1}^N \sum_{\rho=1}^N D_{\alpha\beta} \overline{D_{\alpha\rho}} A_{kn} \tag{86}$$

where $m = k$ and $n = j + \rho - \beta$. The global term in the equations for C and D are similar.

The average is

$$\begin{aligned}
\langle |A|^2 + |B|^2 \rangle &= \frac{1}{L} \int_0^L \left(\sum_{\alpha=1}^N \sum_{\beta=1}^N \sum_{\gamma=1}^N \sum_{\rho=1}^N A_{\alpha\beta} e^{c_\alpha \xi + c_\beta \eta} \overline{A_{\gamma\rho}} e^{-(c_\gamma \xi + c_\rho \eta)} \right) \\
&\quad + \left(\sum_{\alpha=1}^N \sum_{\beta=1}^N \sum_{\gamma=1}^N \sum_{\rho=1}^N B_{\alpha\beta} e^{c_\alpha \xi + c_\beta \eta} \overline{B_{\gamma\rho}} e^{-(c_\gamma \xi + c_\rho \eta)} \right) d\xi \\
&= \sum_{\alpha=1}^N \sum_{\beta=1}^N \sum_{\rho=1}^N (A_{\alpha\beta} \overline{A_{\alpha\rho}} + B_{\alpha\beta} \overline{B_{\alpha\rho}}) e^{(c_\beta - c_\rho) \eta},
\end{aligned} \tag{87}$$

leading to

$$\begin{aligned}
& T_F^{(kj)}[\langle |A|^2 + |B|^2 \rangle C] \\
&= \frac{1}{L^2} \int_0^L \int_0^L \left(\sum_{\alpha=1}^N \sum_{\beta=1}^N \sum_{\rho=1}^N (A_{\alpha\beta} \overline{A_{\alpha\rho}} \right. \\
&\quad \left. + B_{\alpha\beta} \overline{B_{\alpha\rho}}) e^{(c_\beta - c_\rho)\eta} \right) \left(\sum_{m=1}^N \sum_{n=1}^N C_{mn} e^{c_m \xi + c_n} \right) e^{-c_k \xi - c_j \eta} d\xi d\eta \\
&= \sum_{\alpha=1}^N \sum_{\beta=1}^N \sum_{\rho=1}^N (A_{\alpha\beta} \overline{A_{\alpha\rho}} + B_{\alpha\beta} \overline{B_{\alpha\rho}}) C_{kn} \tag{88}
\end{aligned}$$

where $m = k$, $n = j + \rho - \beta$, and $\beta - \rho + n - j = 0$.

Due to the long processing time required for the nested sums, a fully spectral code proved inadvisable and a pseudo-spectral code which would compute the nonlinear terms in real space was implemented.

4.2 Numerically Observed Patterns

We are interested in a systematic numerical study of the solutions of (58) in those regions where either bistability or mode interaction of the steady oblique and normal traveling rolls is theoretically possible. The mode interaction of the steady oblique and normal traveling rolls is theoretically possible and has been seen experimentally. The parameters of the system are

$$(a, b_1, b_2, c, d, \Lambda_1, \Lambda_2, \Omega, p_c, q_c, w_c, k_c, v_c, \epsilon) \tag{89}$$

and the periodicity of the solutions in the ξ, η spatial directions. In Case I, we study the region where bistability of the steady oblique and normal traveling rolls is expected from the normal form analysis. The theoretically stable mode interaction of the steady oblique and normal traveling rolls is explored in Case II. We treat this problem as a multiparametric bifurcation study. We fix all parameters except for $(c, d, \Lambda_1, \Lambda_2)$. The parameters $\Lambda_1, \Lambda_2 \in \mathbb{R}$

varied according to

$$\Lambda_1 = \cos(\phi) \text{ and } \Lambda_2 = \sin(\phi) \text{ for } \frac{-\pi}{2} \leq \phi \leq \frac{3\pi}{2}. \quad (90)$$

In order to have non-steady state patterns we need to have several active Fourier modes for at least one amplitude. The linear terms of the PDE (58),

$$\begin{aligned} A_T &= (\Lambda_1 + \partial_\xi^2 + 2\delta\partial_\xi\partial_\eta + \partial_\eta^2) A, \\ B_T &= (\Lambda_1 + \partial_\xi^2 - 2\delta\partial_\xi\partial_\eta + \partial_\eta^2) B, \\ C_T &= (\Lambda_2 + i\Omega + \alpha\partial_{\xi_+}^2 + \beta\partial_\eta^2) C, \\ D_T &= (\Lambda_2 + i\Omega + \alpha\partial_{\xi_-}^2 + \beta\partial_\eta^2) D \end{aligned} \quad (91)$$

combined with writing the amplitudes as in

$$A(\xi, \eta) = \sum_{k=1}^{2M+1} \sum_{j=1}^{2M+1} a_{kj} e^{i(c_k\xi + c_j\eta)} \quad (92)$$

where $c_\alpha = \frac{-2\pi(\alpha-M-1)}{L}$, leads to the expressions

$$\begin{aligned} \Lambda_1 - (c_k^2 + 2\delta c_k c_j + c_j^2) \\ \Lambda_1 - (c_k^2 - 2\delta c_k c_j + c_j^2) \\ \Lambda_2 - (\alpha_r c_k^2 + \beta_r c_j^2) \\ \Lambda_2 - (\alpha_r c_k^2 + \beta_r c_j^2) \end{aligned} \quad (93)$$

where $\alpha_r = \text{Re}(\alpha)$ and $\beta_r = \text{Re}(\beta_r)$. The associated Fourier modes are active when the expressions (93) are positive. Thus, we want to adjust the diffusion coefficients (δ, α, β) such

that

$$\begin{aligned}
\Lambda_1 &> (c_k^2 + 2\delta c_k c_j + c_j^2) \\
\Lambda_1 &> (c_k^2 - 2\delta c_k c_j + c_j^2) \\
\Lambda_2 &> (\alpha_r c_k^2 + \beta_r c_j^2) \\
\Lambda_2 &> (\alpha_r c_k^2 + \beta_r c_j^2)
\end{aligned} \tag{94}$$

are true for several values of (k, j) when (Λ_1, Λ_2) are positive, $\phi \in [0, \pi/2]$.

For $\phi = \{4\pi/20, 5\pi/20, 6\pi/20\}$, the diffusion coefficients were reduced to

$$\begin{aligned}
\delta &= 0.000000000001 \\
\alpha &= 0.000000000002 + 0.000000000002i \\
\beta &= 0.000000000002 - 0.000000000004i
\end{aligned} \tag{95}$$

which theoretically allows several Fourier modes to be active. Simulations showed only one to three active Fourier modes per amplitude.

A first set of numerical simulations has been done with the following fixed parameters,

$$(a, b_1, b_2, \Omega) = (1.2, 1 + 1.2i, 1.2 + i, 5), \tag{96}$$

$$p_c = q_c = w_c = k_c = v_c = 1.00 \tag{97}$$

with $\epsilon = 0.01$ and the periodicity defined as 2π in both the ξ, η spatial directions. All simulation were run with $M = 16$. The fixed diffusion coefficients were

$$(\delta, \alpha, \beta) = (0.1, 0.02 + 0.2i, 0.02 - 0.4i). \tag{98}$$

The varied parameters (c, d) were $(-2 + i, -1.5 + i)$ for Case I or $(-0.5 + i, -0.5 + i)$ for Case II. The Table 2 gives an overview of the numerically observed behavior in each wedge,

which is examined in more detail in the following two sections. For Case I, the theoretical predictions show the mixed mode solutions are unstable in the wedge and bistability of the steady oblique and normal traveling solutions was expected and found for several values of ϕ within the wedge. In this case we observe numerically the steady oblique and normal traveling waves where they are expected according to the normal form analysis. We also did not observe a steady oblique normal traveling mixed mode solution. The mixed mode solutions seen were a mix of either the two steady oblique amplitudes or the two normal traveling amplitudes.

For Case II, the choice of parameters corresponds to the case where the mixed mode solutions are stable according to the normal form analysis. Mixed mode solutions which were a superposition of a steady oblique mode and a normal traveling mode were observed numerically for values of ϕ within the wedge. As ϕ increased with the theoretical wedge, the magnitude of the A or B amplitudes decreased and the magnitude of the C and D amplitudes increased. Mixed mode solutions were observed at all the theoretical bifurcation lines. The mixed mode solutions seen at the bifurcations from the steady state were a mix of either the two steady oblique amplitudes or the two normal traveling amplitudes. At the bifurcation to the mixed mode solution within the wedge, a mixed mode consisting of either one of the steady oblique modes and both of the traveling normal modes or one of the traveling normal modes and both of the steady oblique modes was observed depending on the ‘side’ of the wedge.

Table 2: Summary of regions and numerically computed patterns for Cases I and II.

	Region	Numerically Computed Patterns
Case I	$-4\pi/20 \leq \phi \leq 3\pi/20$	Steady oblique rolls and a mixed mode solution
	$3\pi/20 < \phi < 6\pi/20$	Steady oblique rolls, traveling normal rolls, steady rectangles, and standing waves
	$6\pi/20 \leq \phi \leq 15\pi/20$	Traveling normal rolls and a mixed mode solution
Case II	$-\pi/2 < \phi \leq 2.9\pi/20$	Steady oblique rolls
	$3\pi/20 \leq \phi \leq 7\pi/20$	Mixed mode solution
	$7.1\pi/20 \leq \phi < \pi$	Traveling normal rolls
	$\phi = -\pi/2, 3\pi/2, \pi$	Mixed mode solution

The third section presents a numerically obtained bifurcation diagram in the c_r, ϕ plane. During the exploration, both bistability of the steady oblique and normal traveling solutions and stable mixed mode solutions were observed as c_r and ϕ were varied. The last section here studies the consistency of the theoretical and numerical results. Overall, the numerical behavior of the solutions agrees with the theoretical prediction.

4.2.1 Case I: Theoretical Bistability

We begin by considering the case where there is bistability of the steady oblique and normal traveling solutions for the normal form (64). Given the parameters $(c, d) = (-2 + i, -1.5 + i)$, the stability diagram, Figure 14, predicts that the steady oblique solutions will be stable for $-\pi/2 < \phi < 0.98279$ and that the normal traveling solution will be stable for $0.46365 < \phi < \pi$. These two regions overlap giving us a bistability region when $0.46365 < \phi < 0.98279$. This also means that the mixed mode solutions are unstable solutions of (64).

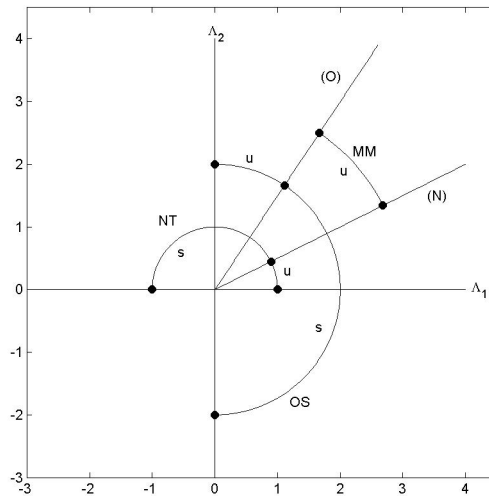


Figure 14: The stability diagram for the given parameters.

Stable steady oblique rolls, normal traveling rolls, and mixed mode solutions were found by varying the parameter ϕ and the initial conditions for the amplitudes (A, B, C, D) . In

all simulations, for a point in space the magnitudes of the (A, B, C, D) amplitudes became constant in time after some transient behavior. As ϕ was increased, the transition from a solution dominated by the A and/or B modes to one dominated by the C and/or D modes varied. This may be caused by some sensitivity to the initial conditions. The magnitude of the (A, B, C, D) amplitudes for the assorted simulations is shown in Figure 15. The magnitude of the (A, B) amplitudes, which give us the steady oblique rolls, appears to peak at about $\phi \approx 0$. The amplitudes also jump to zero for $\phi \approx 1$. The magnitude of the normal traveling rolls' associated amplitudes, (C, D) , peaks for $\phi \approx 1.5$. There is also a sudden jump in their magnitudes at $\phi \approx 0.5$.

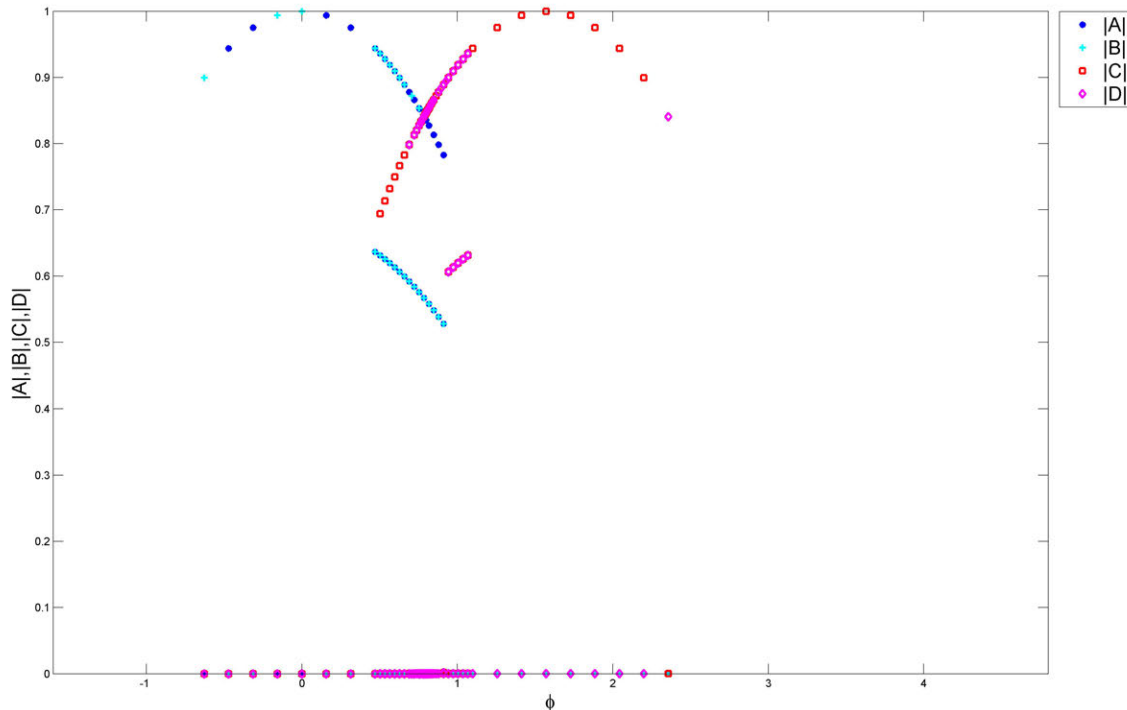


Figure 15: The magnitude of the amplitudes (A, B, C, D) for all simulations with the Case I parameters. This includes simulations with the same value for ϕ , but different initial conditions for (A, B, C, D) .

For $-4\pi/20 \leq \phi \leq 5.8\pi/20$, stable steady oblique rolls were observed consisting of (zig) stationary rolls oriented at an oblique angle to the x - and y -axes, as seen in Figure 16, or

(zag) stationary rolls oriented at an opposite oblique angle to the x - and y -axes, as seen in Figure 17. The zig steady oblique rolls occur when the B mode is dominant, Figure 18a, and the zag steady oblique rolls appear when the A mode is dominant, Figure 18b. Neither zig or zag steady oblique rolls were favored in the simulations. The pattern, U , is sinusoidal in both the x - and y -directions.

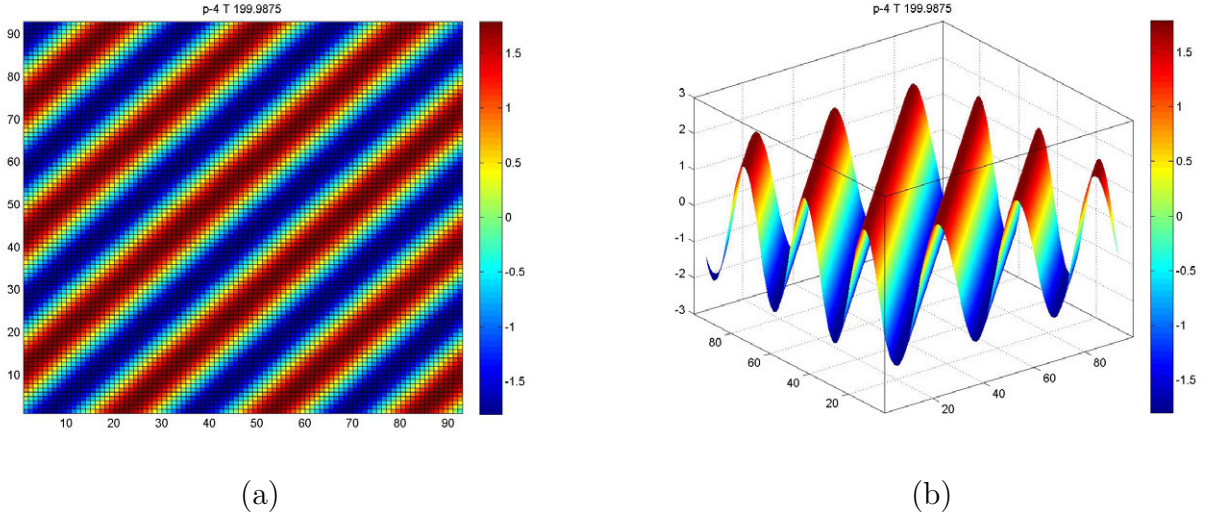
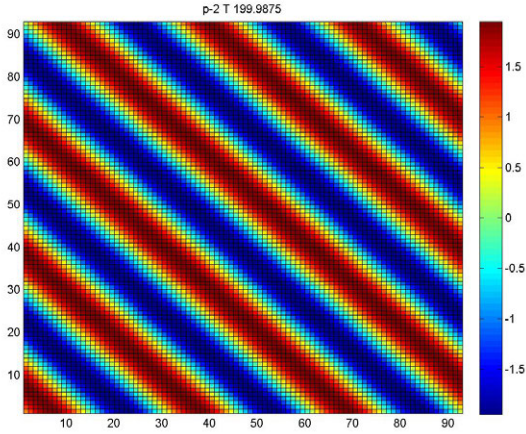


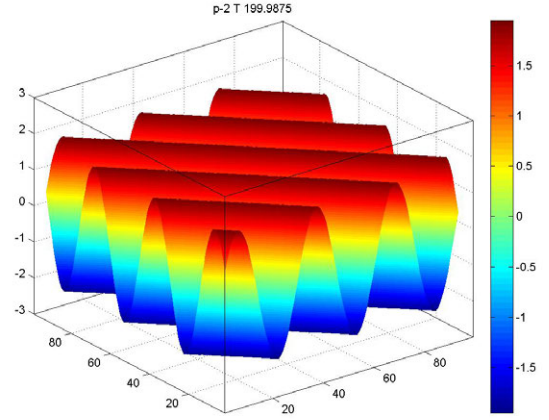
Figure 16: Zig steady oblique rolls observed when $\phi = -4\pi/20$ and $T = 199.9875$ in two (a) and three (b) dimensions. The B amplitude is dominant as seen in Figure 18a and the magnitude of the (A, B, C, D) amplitudes is $(O(10^{-11}), 0.8995, O(10^{-156}), O(10^{-156}))$.

For $3.2\pi/20 \leq \phi \leq 15\pi/20$, stable normal traveling rolls are observed and consist of rolls aligned with the y -axis traveling to the right, Figure 20, or to the left, Figure 21. The left normal traveling rolls were seen when the C mode was dominant and the right normal traveling rolls were observed when the D mode was dominant. Neither left or right traveling normal rolls were favored in the simulations. The pattern, U , is sinusoidal in the x -direction and uniform in the y -direction.

For $3.2\pi/20 \leq \phi \leq 6\pi/20$, both steady oblique and normal traveling solutions were observed to be stable and the transition between them varied, as recorded in Table 3. The columns of random initial conditions revealed that the transition between the steady oblique and normal traveling solutions is not strictly based on the parameters, since steady oblique rolls were observed for $\phi \leq 5.2\pi/20$ and the normal traveling rolls were observed for

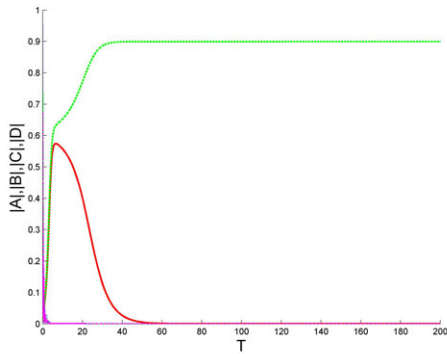


(a)

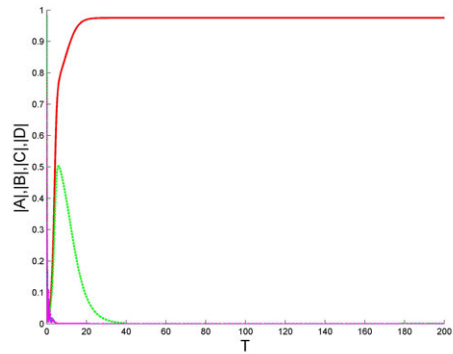


(b)

Figure 17: Zag steady oblique rolls observed when $\phi = -2\pi/20$ and $T = 199.9875$ in two (a) and three (b) dimensions. The amplitude A is the dominant amplitude as seen in Figure 18b and the magnitude of the (A, B, C, D) amplitudes is $(0.9752, O(10^{-16}), O(10^{-150}), O(10^{-150}))$.

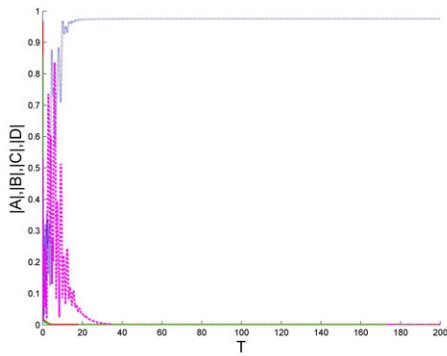


(a) Time series for $n = -4$ showing a dominant B amplitude.

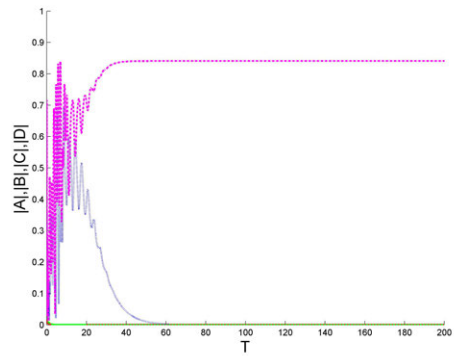


(b) Time series for $n = -2$ showing a dominant A amplitude.

Figure 18: A time series of the magnitude of the amplitudes at a specific spatial point when $\phi = n\pi/20$. The time series for the moduli of the amplitudes (A, B, C, D) is depicted as a solid red line, a dashed green line, a dotted blue line, and a dash-dot magenta line, respectively.



(a) Time series for $n = 12$ showing a dominant C amplitude.



(b) Time series for $n = 15$ showing a dominant D amplitude.

Figure 19: A time series of the magnitude of the amplitudes at a specific spatial point when $\phi = n\pi/20$. The time series for the moduli of the amplitudes (A, B, C, D) is depicted as a solid red line, a dashed green line, a dotted blue line, and a dash-dot magenta line, respectively.

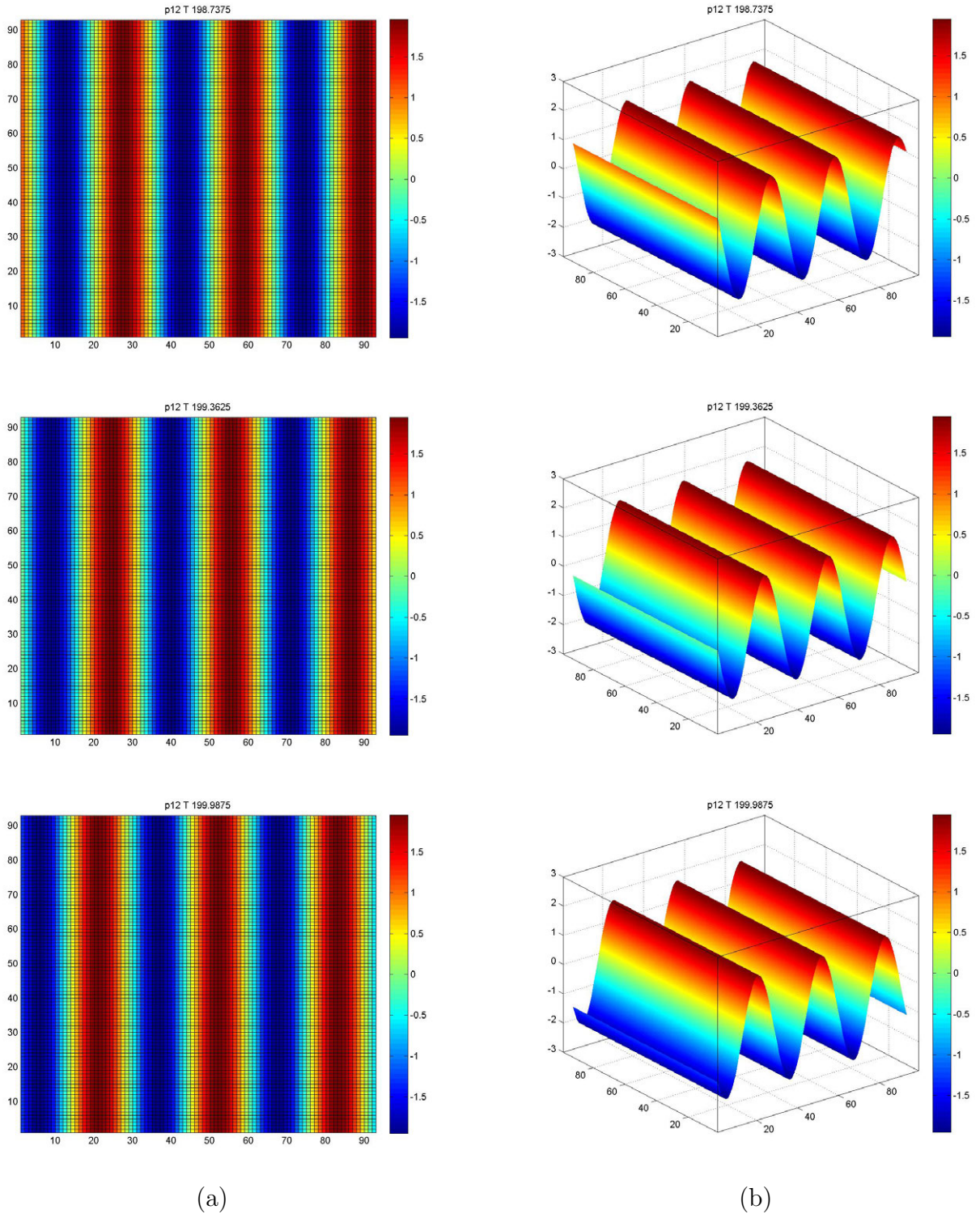


Figure 20: Left traveling normal rolls observed when $\phi = 12\pi/20$ and $T = 198.7375$ to $T = 199.9875$ in two (a) and three (b) dimensions. The C amplitude is dominant, seen in Figure 19a, and the magnitude of the (A, B, C, D) amplitudes is $(O(10^{-11}), O(10^{-191}), 0.9752, O(10^{-17}))$.

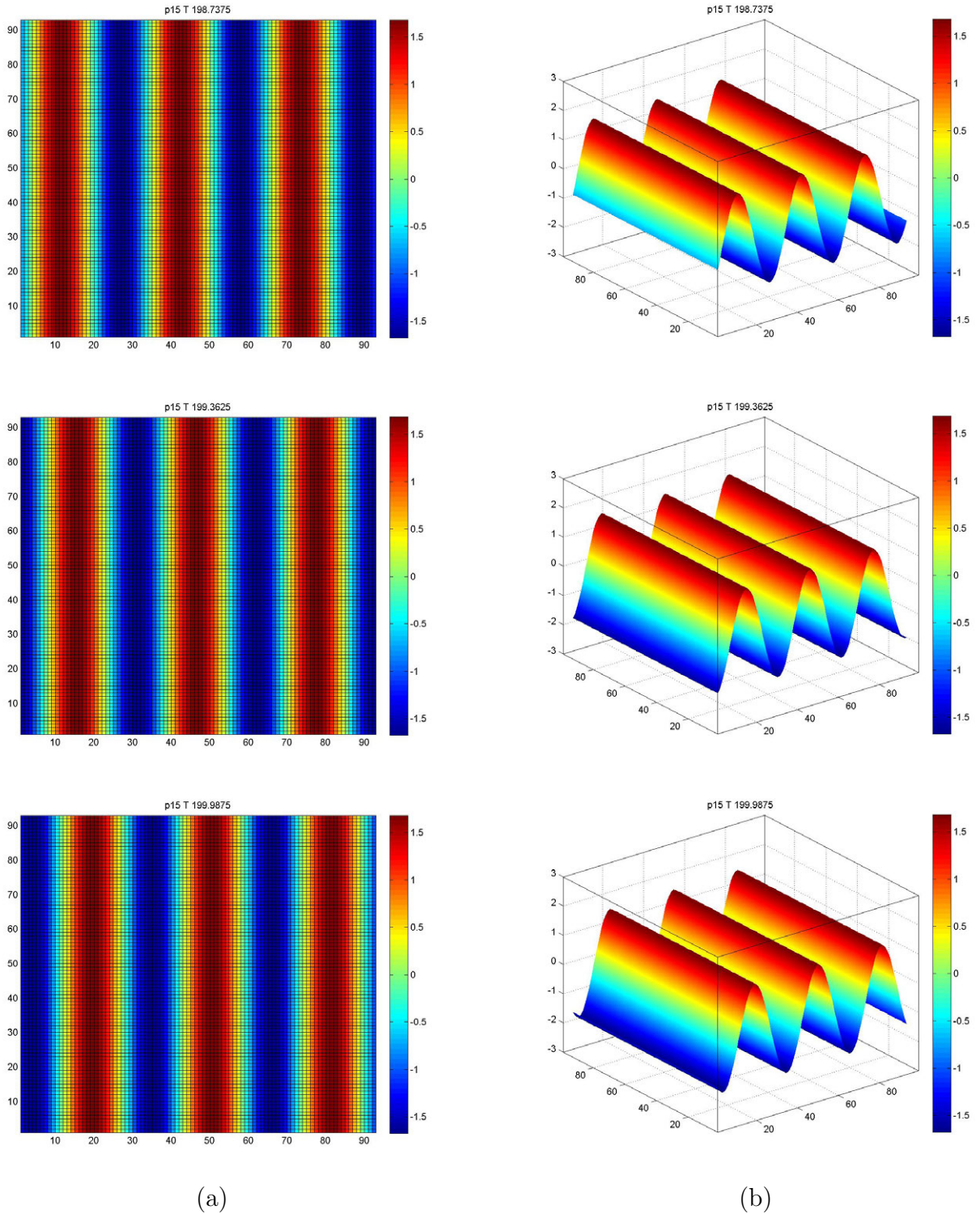


Figure 21: Right traveling normal rolls observed when $\phi = 15\pi/20$ and $T = 198.7375$ to $T = 199.9875$ in two (a) and three (b) dimensions. The amplitude D is the dominant amplitude, seen in Figure 19b, and the magnitude of the (A, B, C, D) amplitudes is $(O(10^{-11}), O(10^{-182}), O(10^{-12}), 0.8409)$.

$\phi \geq 4.7\pi/20$. Bistability of the steady oblique and normal traveling solutions was confirmed for $\phi_b = \{n\pi/20, n = 4.8, 5, 5.08, 5.2\}$. For the different ϕ_b the only changes between simulations were the initial conditions for the amplitudes which were randomly generated for each simulation, thus the observed behavior must be sensitive to the initial conditions of the amplitudes.

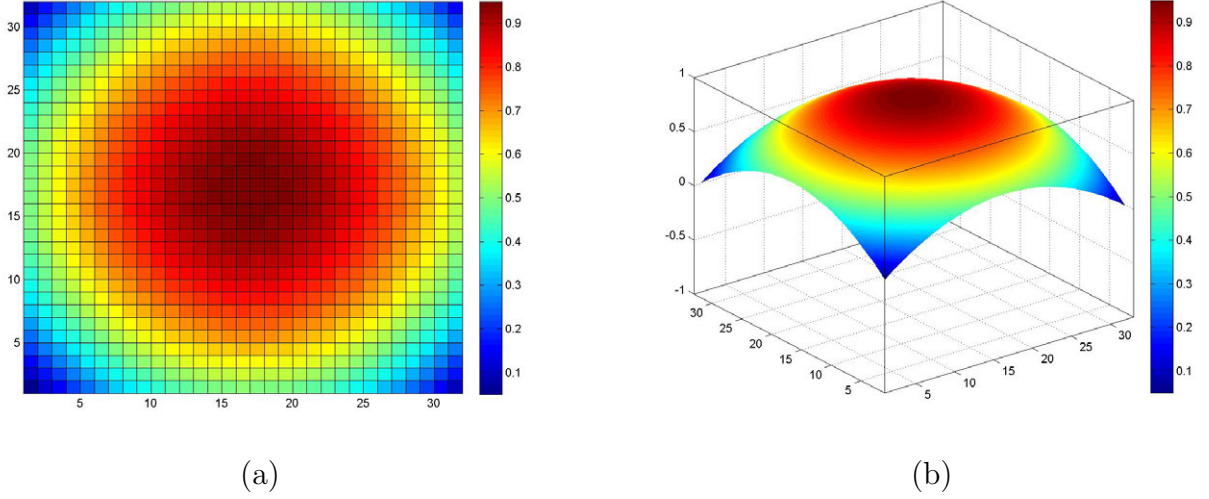
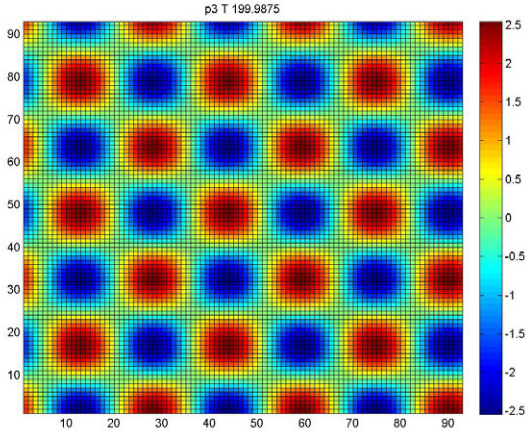


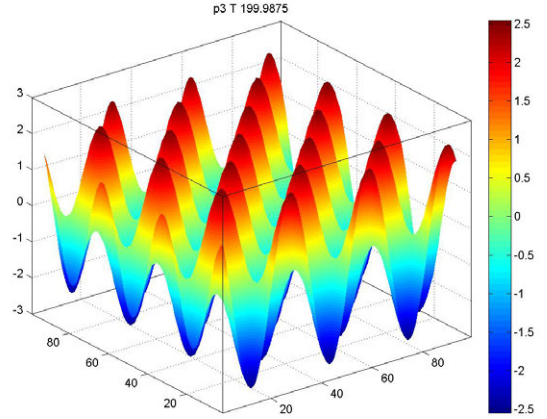
Figure 22: Initial condition used to explore the effect of a specified fixed initial conditions on the behavior of the solutions in two (a) and three (b) dimensions.

In order to explore the sensitivity to initial conditions, fixed values for (A, B, C, D) 's initial conditions, IC_j for $j = 1, \dots, 5$, used values proportional to values of the function depicted in Figure 22 while ϕ was allowed to vary over the interval $[3\pi/20, 6.8\pi/20]$. For the simulations with initial conditions IC_1 , the proportionality multiples for (A, B, C, D) amplitudes' initial conditions were $(1, -0.2, 1, -0.2)$. The initial condition IC_2 had the opposite multiples, $(-0.2, 1, -0.2, 1)$, to IC_1 for the initial conditions of the amplitudes. For both of these initial conditions, the transition between OS and NT behavior occurred between $\phi = 4.2\pi/20$ and $\phi = 4.4\pi/20$ for the given parameter values.

The IC_3 initial condition has the fixed proportionality multiples of $(1, 1, -0.2, -0.2)$ for the amplitudes (A, B, C, D) . In this case, for $3\pi/20 \leq \phi \leq 5.8\pi/20$ the patterns observed were steady rectangles, Figure 23, involving equally dominant (A, B) modes, Figure 24a.

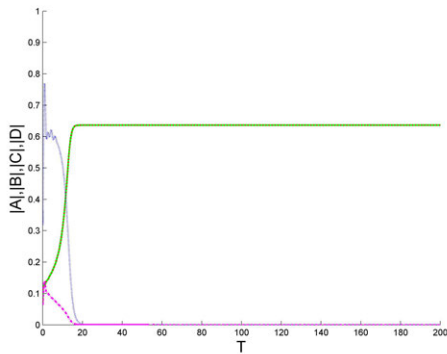


(a)

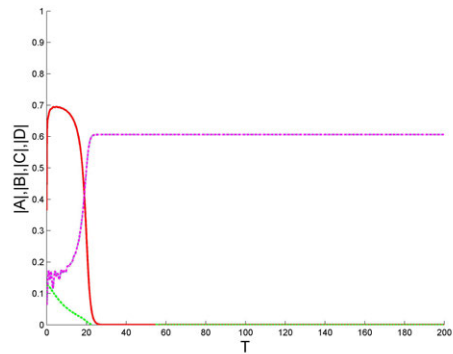


(b)

Figure 23: Steady rectangle solution observed when $\phi = 3\pi/20$ and $T = 199.9875$ in two (a) and three (b) dimensions.



(a) Time series for $n = 3$. The magnitude of the (A, B, C, D) amplitudes are $(0.6364, 0.6364, O(10^{-63}), O(10^{-64}))$.



(b) Time series for $n = 6$. The magnitude of the (A, B, C, D) amplitudes are $(0.6364, 0.6364, O(10^{-63}), O(10^{-64}))$.

Figure 24: A time series of the magnitude of the amplitudes at a specific spatial point when $\phi = n\pi/20$. The time series for the moduli of the amplitudes (A, B, C, D) is depicted as a solid red line, a dashed green line, a dotted blue line, and a dash-dot magenta line, respectively.

The similarity of the initial conditions may be the cause of this pattern being seen for $3\pi/20 \leq \phi \leq 5.8\pi/20$. We remark here that although the standing rectangles were not stable in the normal form, for the selection of parameters used in the runs, they can be stable solutions, though, in the Ginzburg Landau equations as observed numerically. For $\phi \geq 6\pi/20$, normal standing waves, Figure 25, were observed and the C and D amplitudes

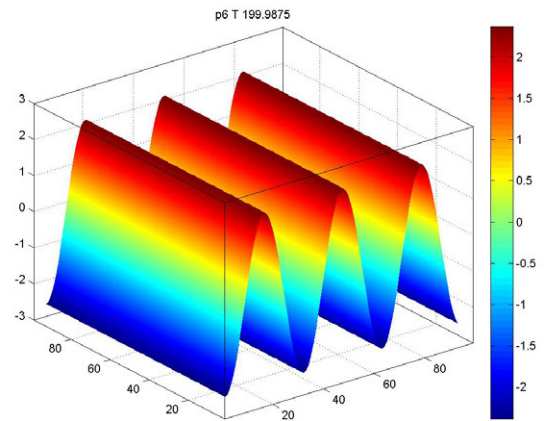
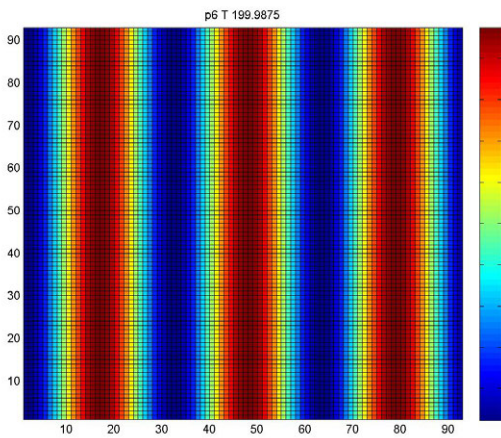
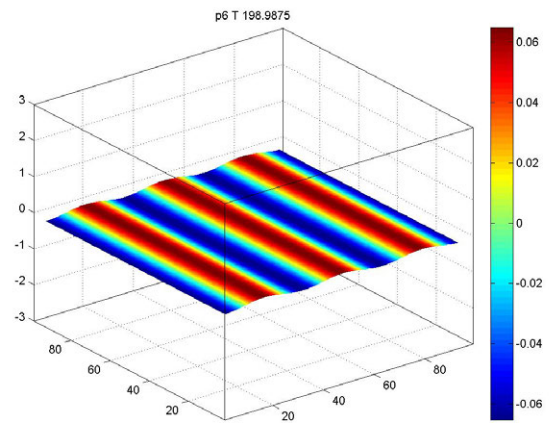
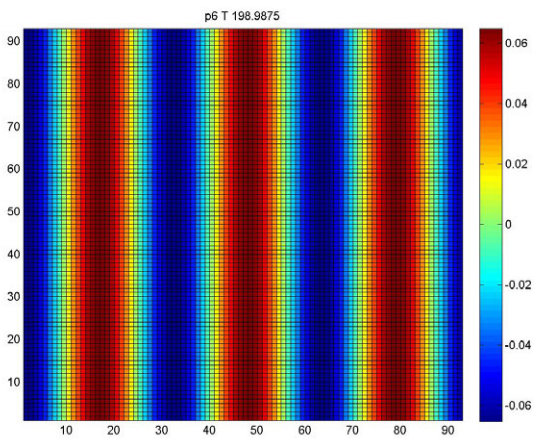
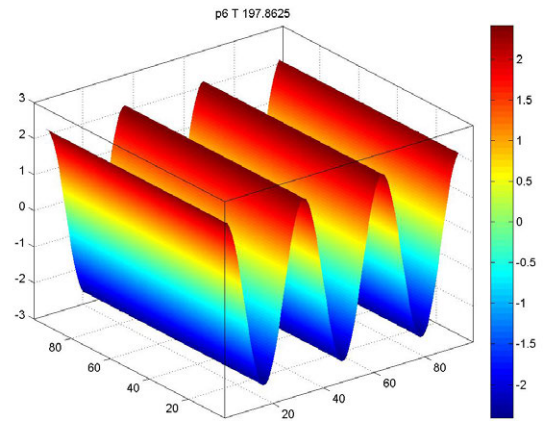
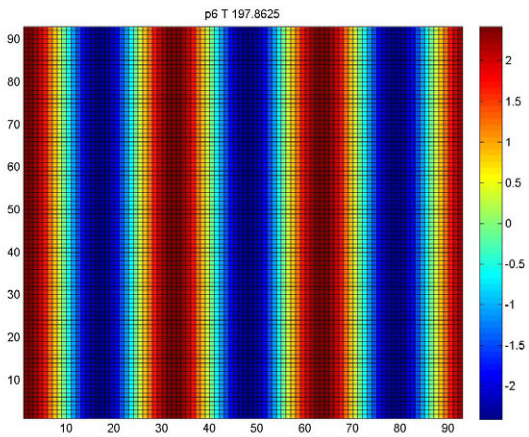
were equally dominant, Figure 24b. Thus, the standing wave is a superposition of the two normal traveling modes. Again, the pattern may be a result of the similarity of the initial conditions.

The proportionality multiples for the IC_4 and IC_5 initial conditions were $(1, -0.2, -0.2, -0.2)$ and $(-0.2, -0.2, 1, -0.2)$, respectively. For IC_4 , the transition from zag steady oblique rolls to the standing wave solution occurred between $\phi = 5.8\pi/20$ and $\phi = 6\pi/20$. Also, the magnitude of the A amplitude decreases from 0.9439 when $n = 3$ to 0.7829 at $n = 5.8$ and then drops to $O(10^{-10})$ for $n = 6$. For the other case, IC_5 , the transition from the steady rectangles solution to left traveling normal rolls occurred between $\phi = 3\pi/20$ and $\phi = 3.2\pi/20$. Also, the modulus of the C amplitude jumps from $O(10^{-30})$ when $n = 3$ to 0.6941 at $n = 3.2$ and then increases to 0.8995 for $n = 6$.

Over all the simulations, bistability of the steady oblique rolls and the normal traveling rolls was observed for

$$\phi_b = \{n\pi/20, n = 3.2, 3.4, 3.6, 3.8, 4, 4.2, 4.4, 4.6, 4.8, 5, 5.08, 5.2, 5.4, 5.6, 5.8\}. \quad (99)$$

The ϕ_b are within the theoretical expectation for where the bistability region would occur.



(a)

(b)

Figure 25: Standing wave solution observed when $\phi = 6\pi/20$ and $T = 197.8625$ to $T = 199.9875$ in two (a) and three (b) dimensions.

Table 3: Behavior of solutions for various ϕ values and different initial conditions. For the IC_j simulations, the (A, B, C, D) 's initial conditions were fixed to be proportional to the values seen in Figure 22. The proportionality multiples for IC_1, IC_2, IC_3, IC_4 , and IC_5 were $(1, -0.2, 1, -0.2)$, $(-0.2, 1, -0.2, 1)$, $(1, 1, -0.2, -0.2)$, $(1, -0.2, -0.2, -0.2)$, and $(-0.2, -0.2, 1, -0.2)$, respectively. Here OS are steady oblique rolls, NT are normal traveling rolls, RS are standing rectangles, and SW are normal standing waves.

$\phi = n\pi/20$		Initial Condition							$\phi = n\pi/20$		Initial Condition						
n	random			IC_1	IC_2	IC_3	IC_4	IC_5	n	random			IC_1	IC_2	IC_3	IC_4	IC_5
3	OS			OS	OS	RS	OS	RS	5.12		NT	NT					
3.2				OS	OS	RS	OS	NT	5.14		NT	NT					
3.4				OS	OS	RS	OS	NT	5.16		NT	NT					
3.6				OS	OS	RS	OS	NT	5.18		NT	NT					
3.8				OS	OS	RS	OS	NT	5.2	OS	NT	NT	NT	NT	RS	OS	NT
4	OS			OS	OS	RS	OS	NT	5.22			NT					
4.2				OS	OS	RS	OS	NT	5.24			NT					
4.4				NT	NT	RS	OS	NT	5.26			NT					
4.5		OS							5.28			NT					
4.6		OS		NT	NT	RS	OS	NT	5.3	NT	NT	NT	NT	NT	RS		
4.7		NT		NT	NT				5.32			NT					
4.8		NT	OS	NT	NT	RS	OS	NT	5.34			NT					
4.82			OS						5.36			NT					
4.86			NT						5.38			NT					
4.88			NT						5.4	NT	NT	NT	NT	NT	RS	OS	NT
4.9		NT	NT						5.5	NT	NT						
4.92			NT						5.6	NT			NT	NT	RS	OS	NT
4.94			NT						5.7	NT							
4.96			OS						5.8	NT			NT	NT	RS	OS	NT
4.98			NT						5.9	NT							
5	OS	NT	OS	NT	NT	RS	OS	NT	6	NT			NT	NT	SW		NT
5.02		NT	NT						6.2				NT	NT	SW	SW	
5.04		NT	NT						6.4				NT	NT	SW		
5.06		NT	NT						6.6				NT	NT	SW		
5.08		OS	NT						6.8				NT	NT	SW		
5.1	NT	NT		NT	NT	RS											

4.2.2 Case II: Theoretically Stable Mixed Mode Solution

In this case $(c, d) = (-0.5 + i, -0.5 + i)$ and the normal form analysis leads to the prediction that the steady oblique solution is stable for $-\pi/2 < \phi < 0.4636$, the normal traveling solution is stable for $1.1071 < \phi < \pi$, and a mixed mode solution is stable for $0.4636 < \phi < 1.1071$, Figure 26. The various solutions were observed where expected. Only individually generated random initial conditions were used for the simulations in this section.

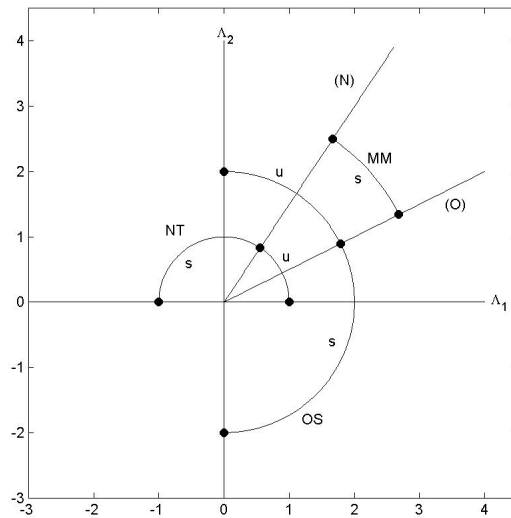


Figure 26: The theoretical stability diagram for the given the parameters.

The magnitude of the amplitudes (A, B, C, D) are shown in Figure 27. Changes in the magnitude of the amplitudes are gradual with no jumps. The magnitude of the larger of the (A, B) amplitudes peaks at $\phi \approx 0$, increasing from $\phi = -\pi/2$ until $\phi \approx 0$ and decreasing to zero for $\phi > 0$ until $\phi \approx 1.1$. The magnitude of the larger of the (C, D) amplitudes increases from zero at $\phi \approx 0.5$ until $\phi \approx 1.6$ and decreasing back to zero for $\phi > 1.6$ until $\phi \approx 1.1$. Near the bifurcation lines, $\phi = -\pi/2, \pi$, either the (A, B) or the (C, D) amplitudes are small but influence the resulting pattern. For $\phi = -\pi/2$ there are steady rectangles, Figure 23,

from a superposition of the (A, B) modes and a (C, D) mixed mode solution when $\phi = \pi$. There is a mixed mode solution consisting of three modes for ϕ near 0.5 and 1.1.

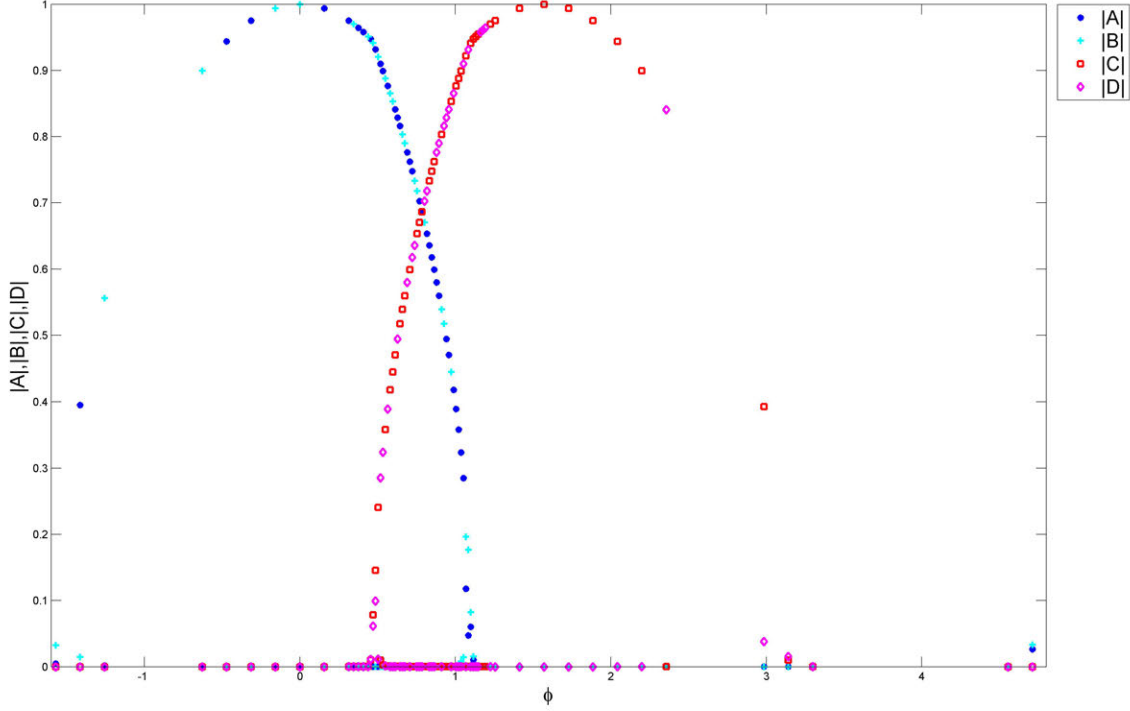


Figure 27: The magnitude of the amplitudes (A, B, C, D) for all simulations with the specified parameters.

For $-9\pi/20 \leq \phi \leq 2.9\pi/20$, stable zig or zag steady oblique rolls were observed, one such is depicted in Figure 28, and either the A or B amplitude is dominant, Figure 29. Again, there is no preferred direction for the steady oblique rolls and the only change between simulations other than ϕ is the initial conditions for the amplitudes. The pattern, U , has a stationary sinusoidal wave in the x - and y - directions.

For $7.1\pi/20 \leq \phi \leq 19\pi/20$, stable leftward and rightward traveling normal rolls were observed as seen in Figures 30 and 31, and either the C or D amplitude is dominant, Figure 32. Neither the left or the right traveling normal rolls were favored in the simulations. The pattern, U , has traveling sine wave in the x -direction and is uniform in the y -direction.

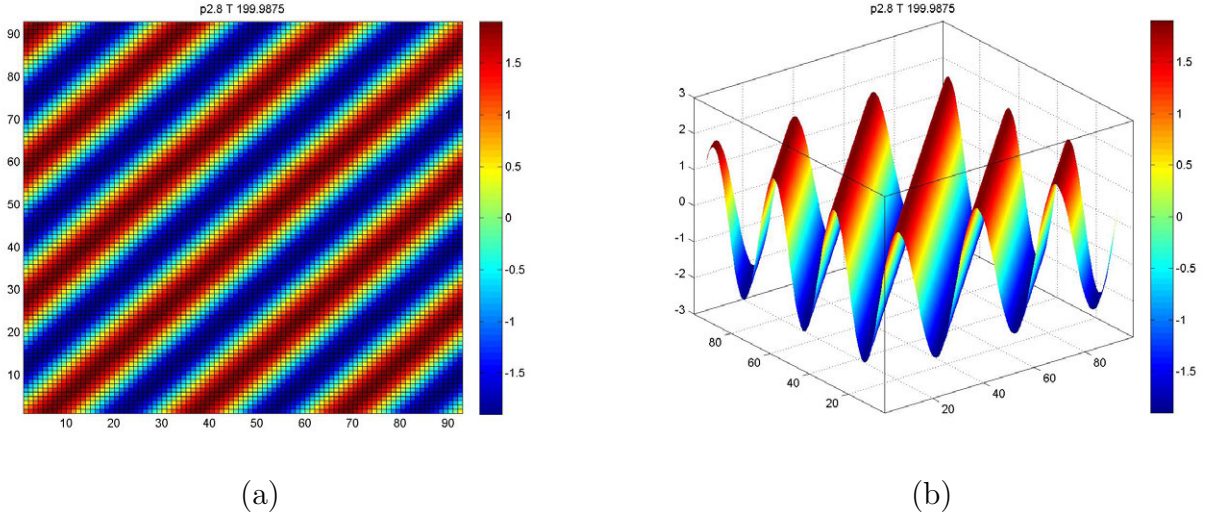


Figure 28: Zig steady oblique rolls $\phi = 2.8\pi/20$ and $T = 199.9875$ in two (a) and three (b) dimensional representations. The magnitude of the amplitudes (A, B, C, D) is $(O(10^{-11}), 0.9512, O(10^{-4}), O(10^{-4}))$.

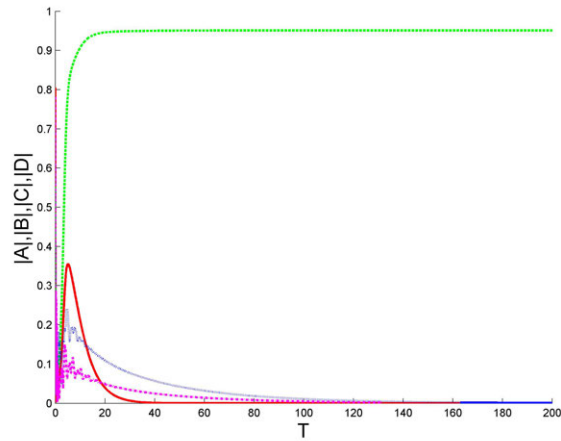


Figure 29: A time series of the magnitude of the amplitudes at a specific spatial point when $\phi = 2.8\pi/20$. The dominant amplitude is B . The time series for the moduli of the (A, B, C, D) amplitudes is depicted as a solid red line, a dashed green line, a dotted blue line, and a dash-dot magenta line, respectively.

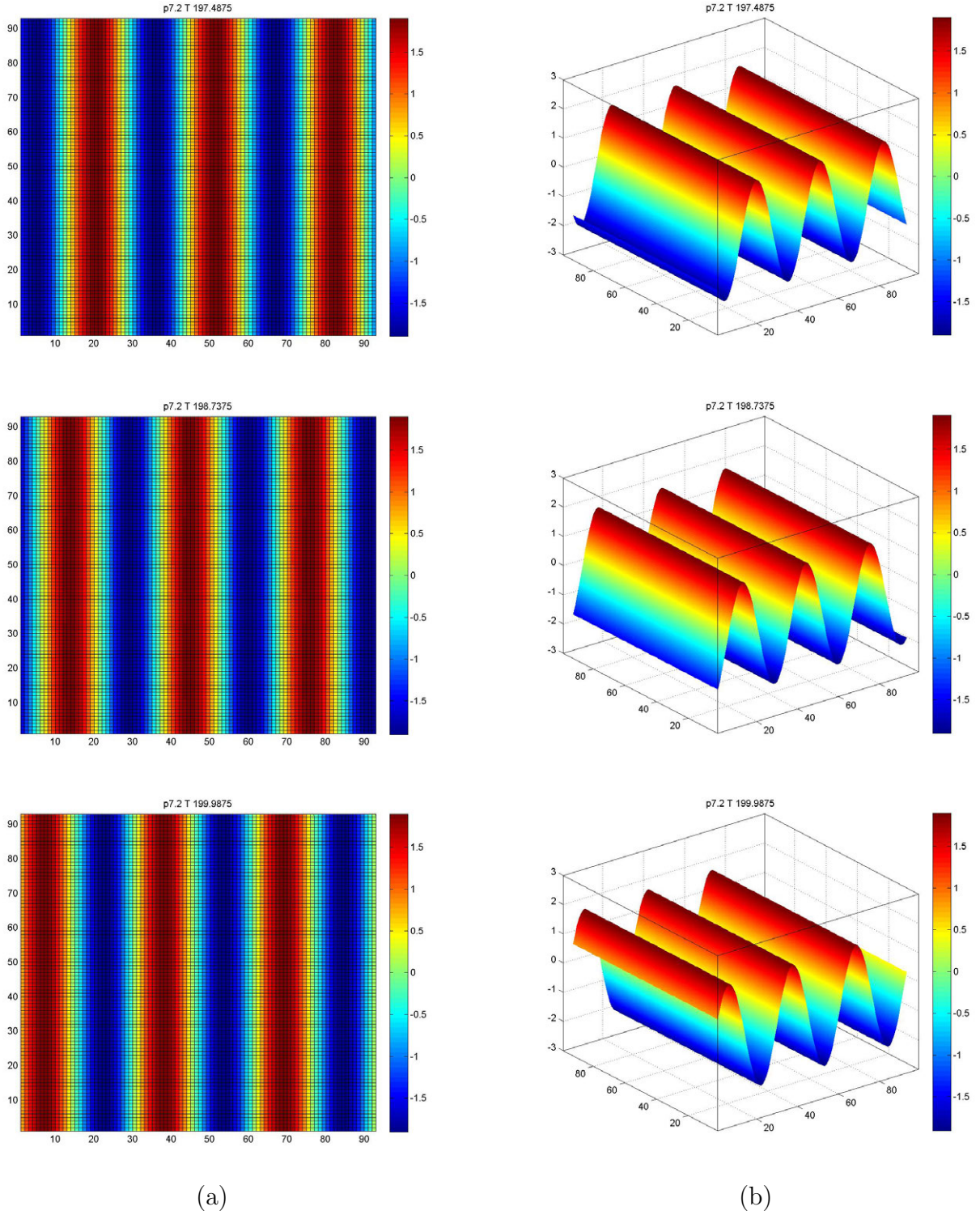


Figure 30: Left traveling normal rolls observed when $\phi = 7.2\pi/20$ and $T = 197.4875$ to $T = 199.9875$ in two (a) and three (b) dimensional representations. The C mode is dominant.

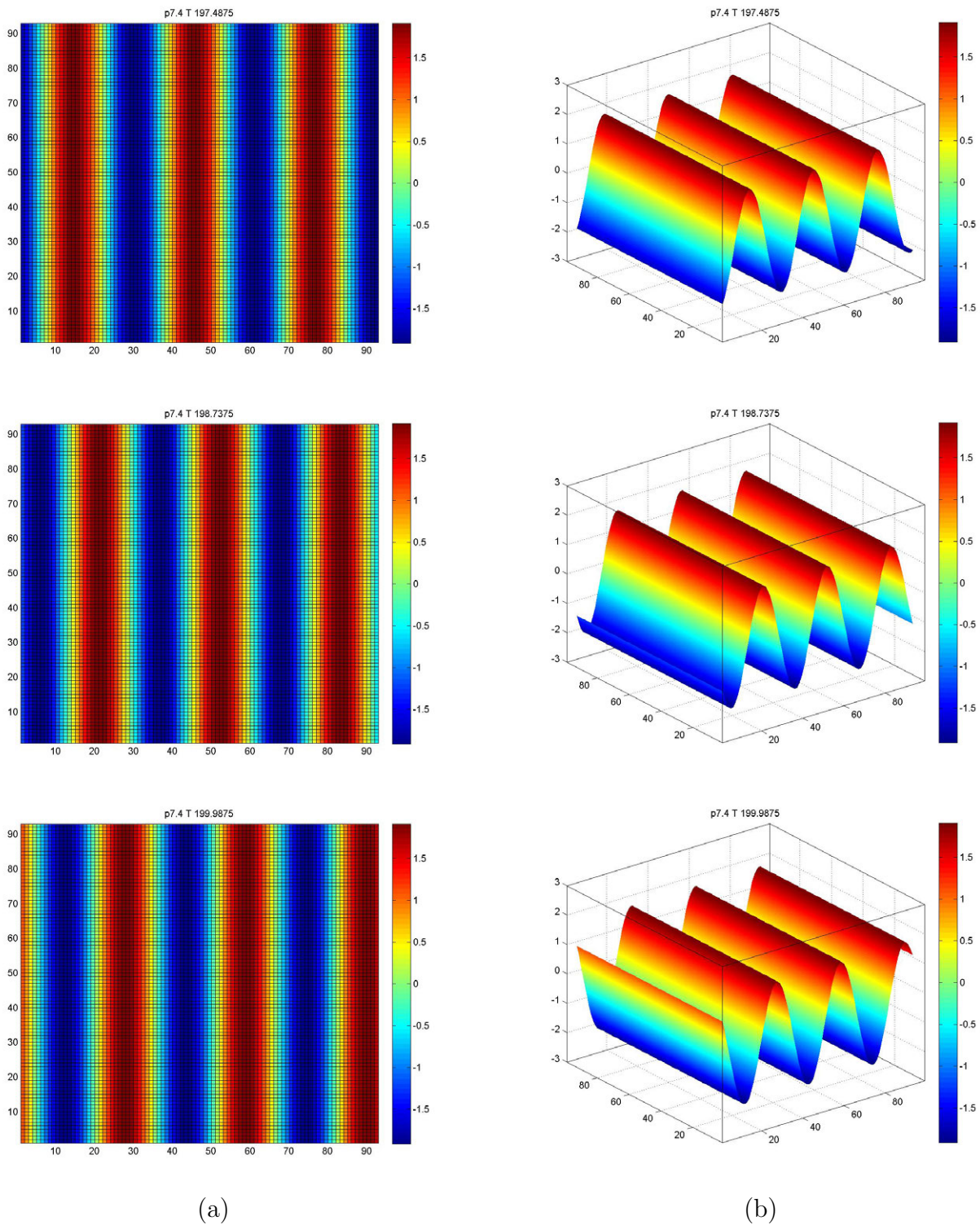
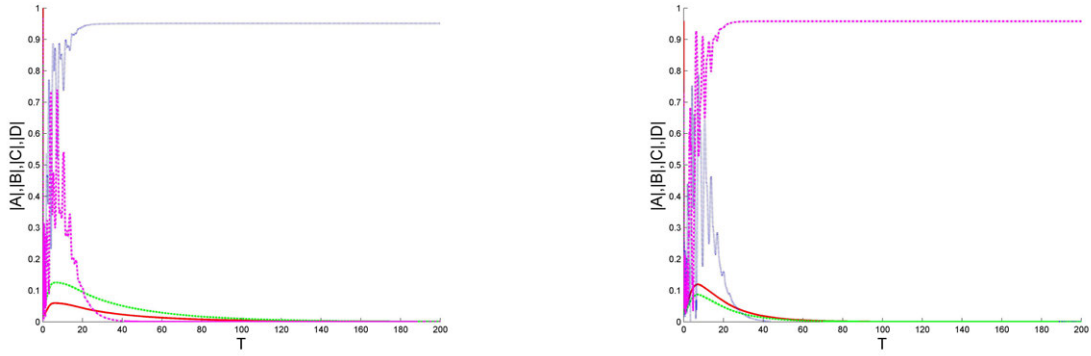


Figure 31: Right traveling normal rolls observed when $\phi = 7.4\pi/20$ and $T = 197.4875$ to $T = 199.9875$ in two (a) and three (b) dimensional representations. The D mode is dominant.



(a) Time series for $n = 7.2$. The magnitude of the amplitudes (A, B, C, D) is $(O(10^{-4}), O(10^{-4}), 0.9512, O(10^{-16}))$.

(b) Time series for $n = 7.4$. The magnitude of the amplitudes (A, B, C, D) is $(O(10^{-7}), O(10^{-7}), O(10^{-16}), 0.9580)$.

Figure 32: A time series of the magnitude of the amplitudes at a specific spatial point when $\phi = n\pi/20$. The time series for the moduli of the (A, B, C, D) amplitudes is depicted as a solid red line, a dashed green line, a dotted blue line, and a dash-dot magenta line, respectively.

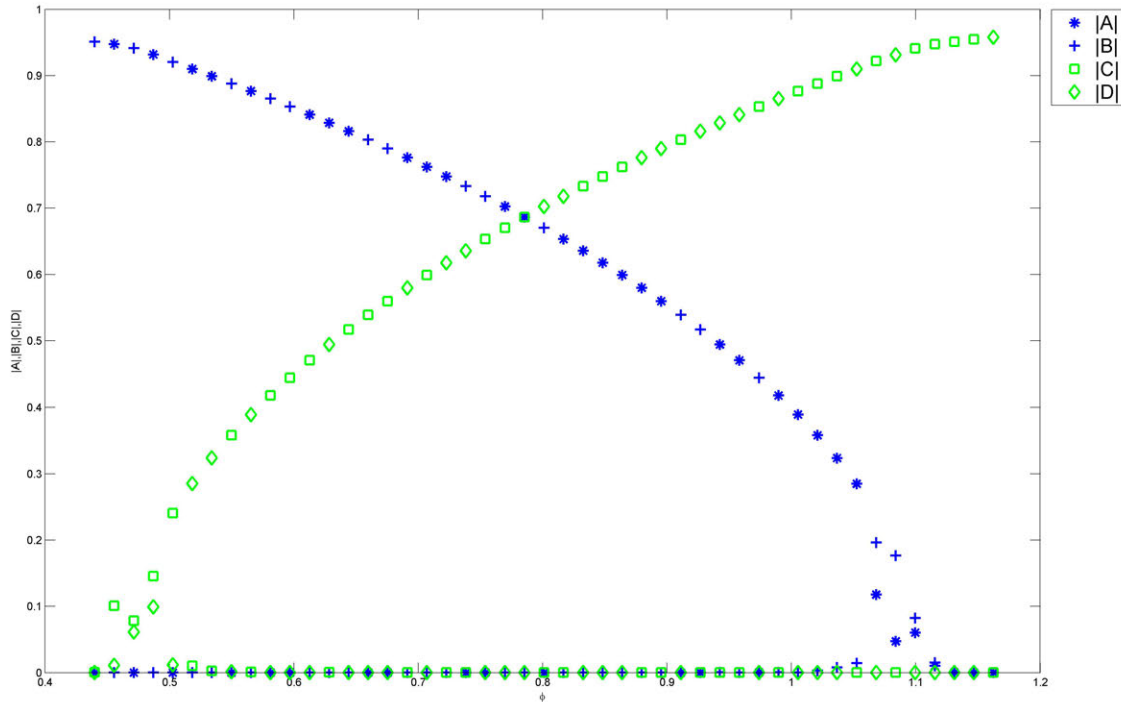


Figure 33: Magnitude of the amplitudes for $3\pi/20 \leq \phi \leq 7\pi/20$. As ϕ increases from $2.8\pi/20$ to $7.4\pi/20$ the modulus of the A and B amplitudes decreases and the modulus of the C and D amplitudes increases.

For $3\pi/20 \leq \phi \leq 7\pi/20$, a continuous deformation from the steady oblique rolls to the traveling normal rolls was observed as seen in Figures 34 through 54. In an exploration of this region, Figure 33 shows that as ϕ increases the moduli of a steady oblique amplitude decreases and the moduli of a normal traveling amplitude increases. When ϕ is near $3\pi/20$, the modulus of the C and D amplitudes both become larger than zero yet significantly smaller than the dominant steady oblique amplitude. This leads to (C, D) mixed mode component added to the steady oblique pattern created by the dominant amplitude. At the other end, for ϕ near $7\pi/20$ the magnitude of the A and B amplitudes both become larger than zero though smaller than the dominant normal traveling amplitude. The traveling normal rolls created by the dominant amplitude has a (A, B) mixed mode component added to it.

The individual stages which the transformation from steady oblique rolls to normal traveling rolls goes through as ϕ increases from $3\pi/20$ to $7\pi/20$, start with the pattern for $\phi = 3\pi/20$, seen in Figure 34, in which steady oblique rolls have shifting formations along the extrema of the steady oblique rolls. This pattern is a superposition of a steady oblique mode and both of the normal traveling modes, Figure 55a.

For $3.2\pi/20 \leq \phi \leq 3.6\pi/20$, the steady oblique rolls which have traveling formations along the extrema are observed (see Figures 35-37). The magnitude of the formations is less than half that of the magnitude of the steady oblique rolls. The pattern is a superposition of a steady oblique mode and a normal traveling mode (see Figures 55b-d) and has the characteristics of wavy patterns.

For $3.8\pi/20 \leq \phi \leq 4.8\pi/20$, the pattern represented in Figures 38-43, shows formations traveling along a steady oblique roll of decreasing amplitude. The formations have a magnitude of more than half of the amplitude of the steady oblique rolls. The pattern is a superposition of a steady oblique mode and a normal traveling mode with smaller magnitude, Figures 55e-56d.

Through the last three stages the magnitude of the dominant steady oblique amplitude has decreased while the larger of the normal traveling amplitudes has increased, until at

$\phi = 5\pi/20$ they have the same magnitude. This pattern shown in Figure 44, has formations traveling along oblique paths and is a superposition of steady oblique rolls and normal traveling rolls of equal magnitude, Figure 56e.

For $5.2\pi/20 \leq \phi \leq 6\pi/20$, Figures 45-49, there are formations traveling upward or downward along the extrema of normal traveling rolls of increasing amplitude, however the overall appearance is that of formations traveling along an oblique path. This pattern is a superposition of one normal traveling mode and one steady oblique mode with the magnitude of the normal traveling mode being roughly twice that of the magnitude of the steady oblique mode, Figures 56f-57d.

For $6.2\pi/20 \leq \phi \leq 6.6\pi/20$ the amplitude of the normal traveling rolls increases and the patterns have normal traveling rolls with formations traveling upward or downward along the extrema of the normal traveling rolls, as in Figures 50-52. This pattern is a superposition of one normal traveling mode and one steady oblique mode with the magnitude of the normal traveling mode being roughly twice that of the magnitude of the steady oblique mode, Figures 57e-58a.

In the last stage of the transformation before traveling normal rolls, for $6.8\pi/20 \leq \phi \leq 7\pi/20$, the patterns becomes normal traveling rolls with a standing wave pattern along the extrema, seen in Figures 53-54. The pattern, U , has a traveling sine wave in the x -direction and a standing wave in the y -direction. This pattern is a superposition of a normal traveling mode and both of the steady oblique modes, Figures 58b-58c.

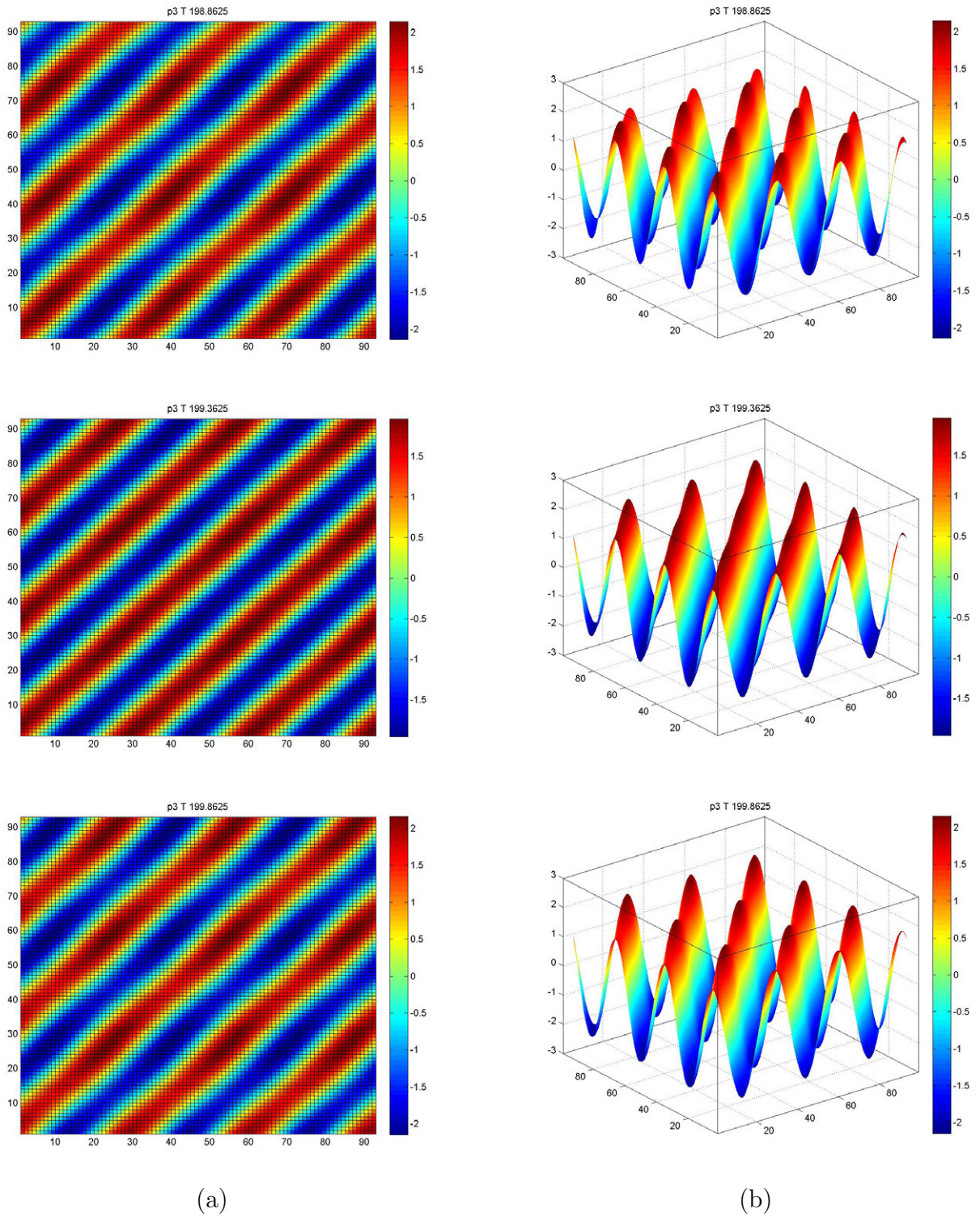


Figure 34: Zig steady oblique rolls with a standing wave pattern along the oblique's extrema observed when $\phi = 3\pi/20$ and $T = 198.8625$ to $T = 199.8625$ in two (a) and three (b) dimensional representations. The dominant amplitude is B , but there is some influence from C and D , Figure 55a.

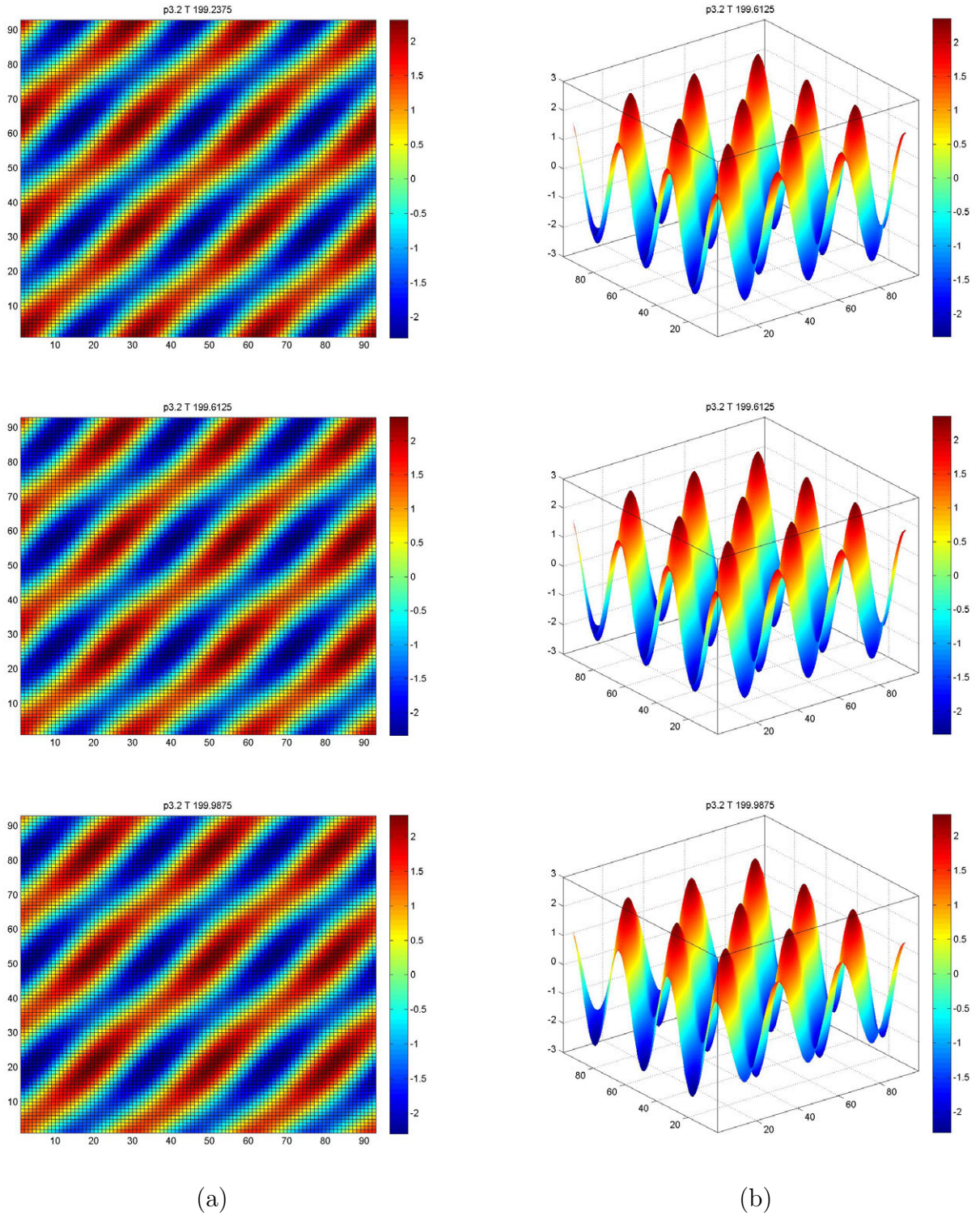


Figure 35: Zig steady oblique rolls with formations traveling downward along the oblique's extrema observed when $\phi = 3.2\pi/20$ and $T = 199.2375$ to $T = 199.9875$ in two (a) and three (b) dimensional representations. The dominant amplitudes are B and C , Figure 55b.

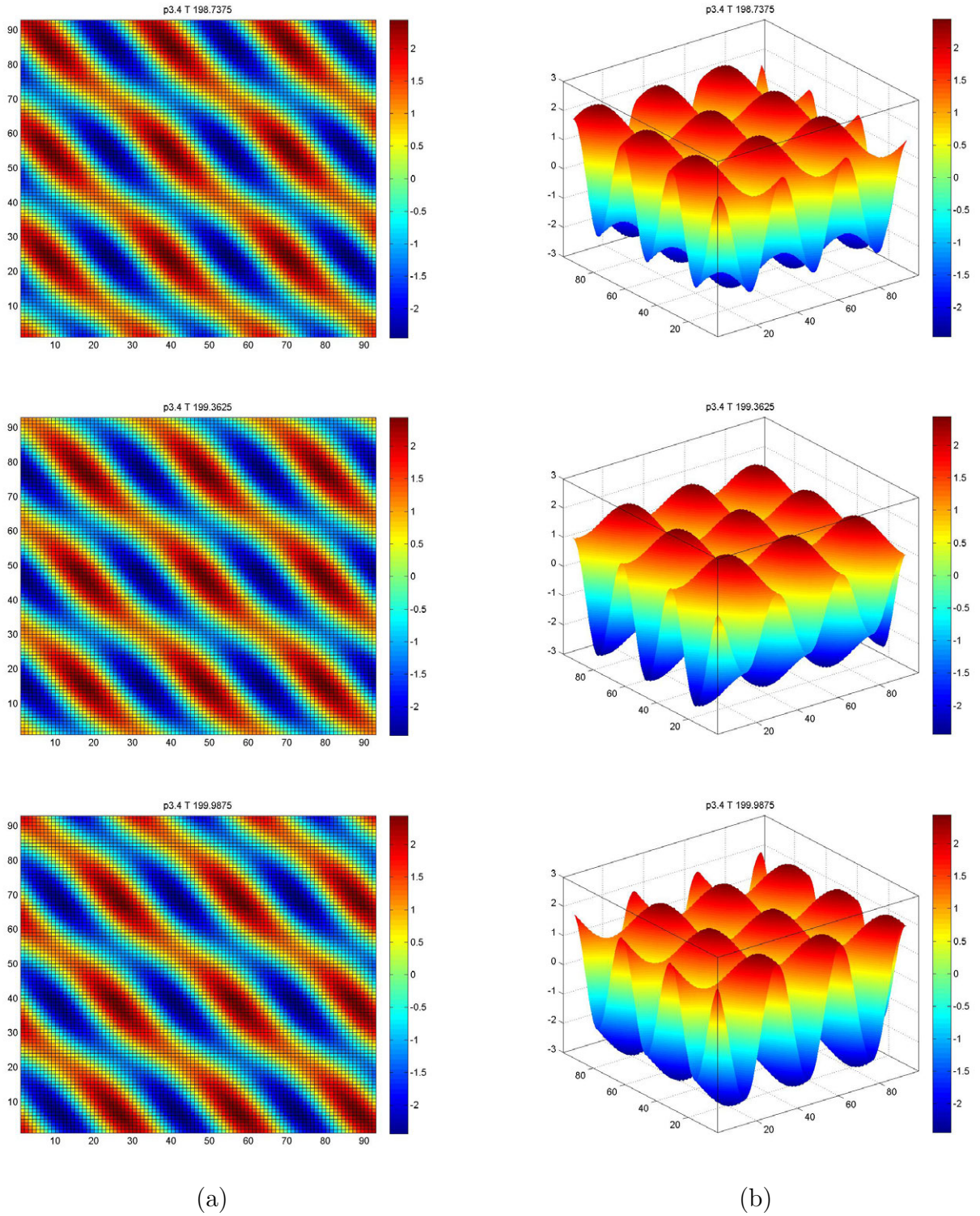


Figure 36: Zig steady oblique rolls with formations traveling downward along the oblique's extrema observed when $\phi = 3.4\pi/20$ and $T = 198.7375$ to $T = 199.9875$ in two (a) and three (b) dimensional representations. The dominant amplitudes are A and D , Figure 55c.

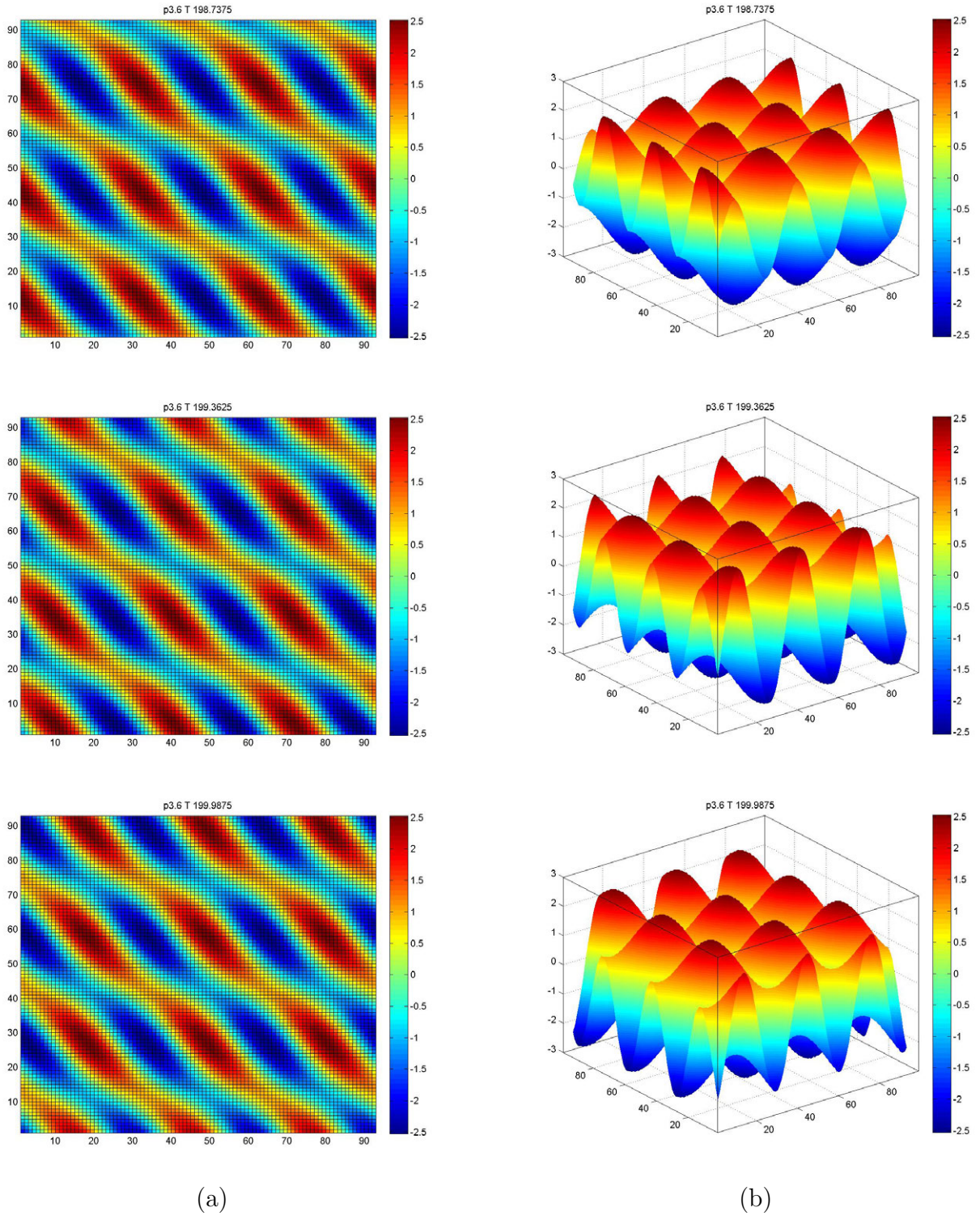
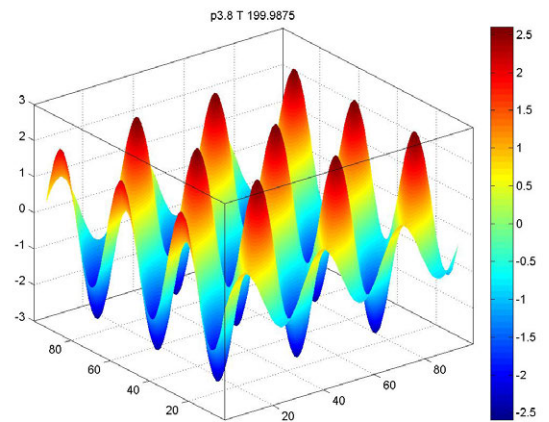
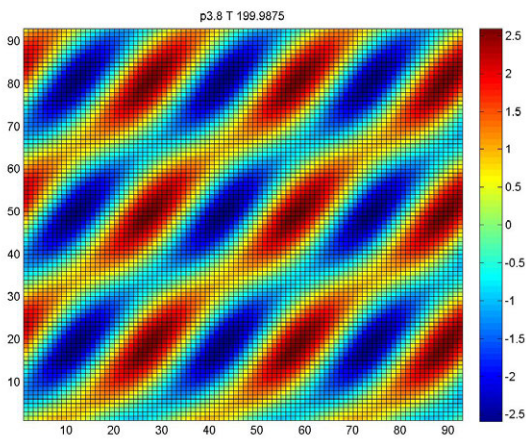
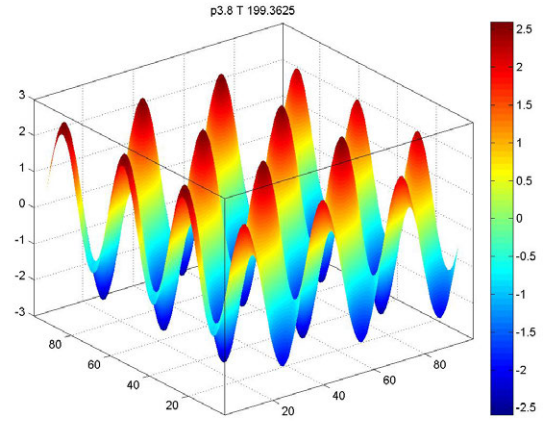
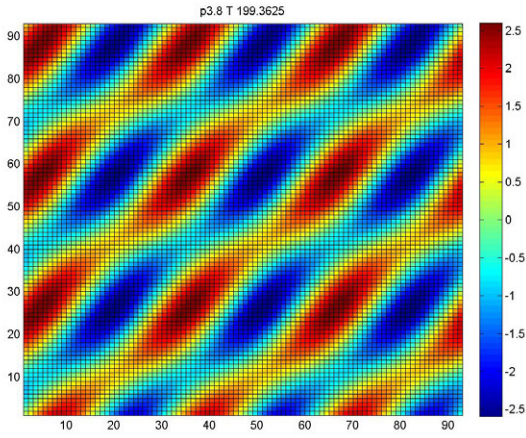
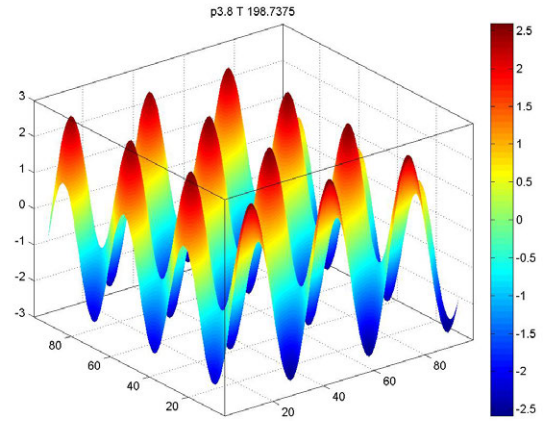
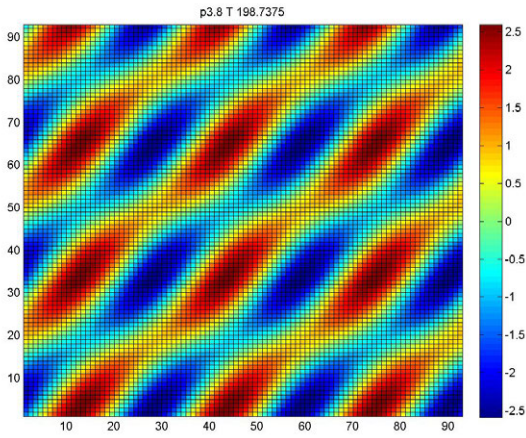


Figure 37: Zig steady oblique rolls with formations traveling downward along the oblique's extrema observed when $\phi = 3.6\pi/20$ and $T = 198.7375$ to $T = 199.9875$ in two (a) and three (b) dimensional representations. The dominant amplitudes are A and D , Figure 55d.



(a)

(b)

Figure 38: Formations travel downward along a zig oblique path observed when $\phi = 3.8\pi/20$ and $T = 198.7375$ to $T = 199.9875$ in two (a) and three (b) dimensional representations. The dominant amplitudes are B and C , Figure 55e.

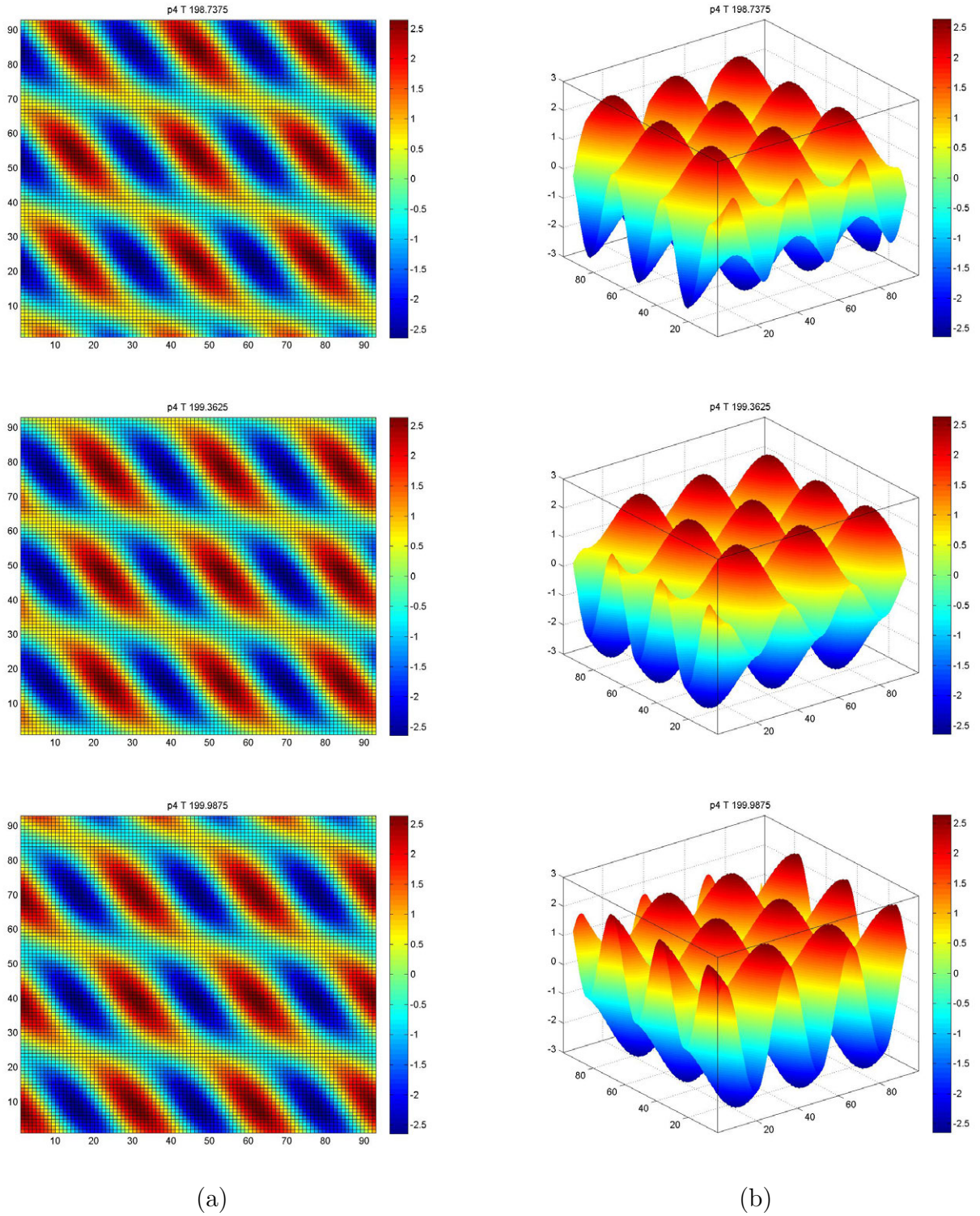
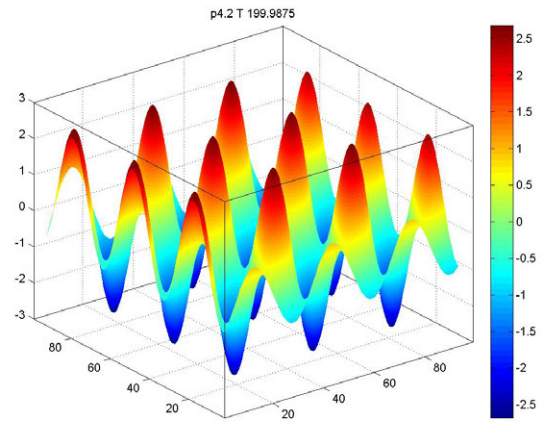
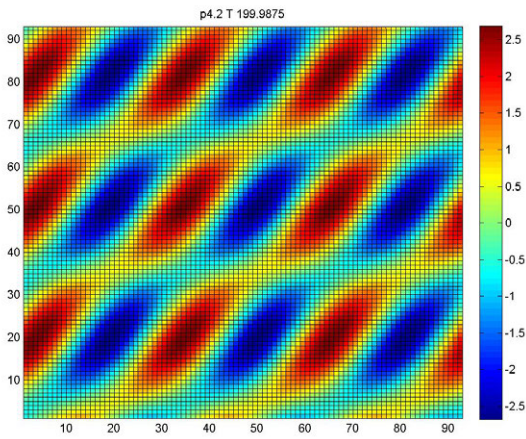
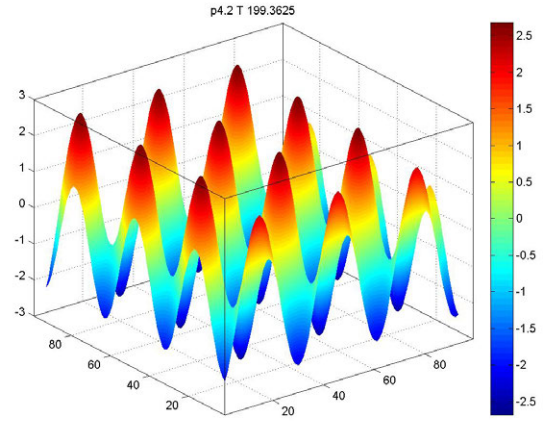
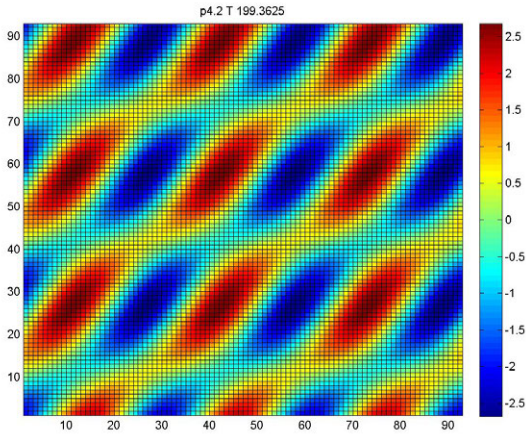
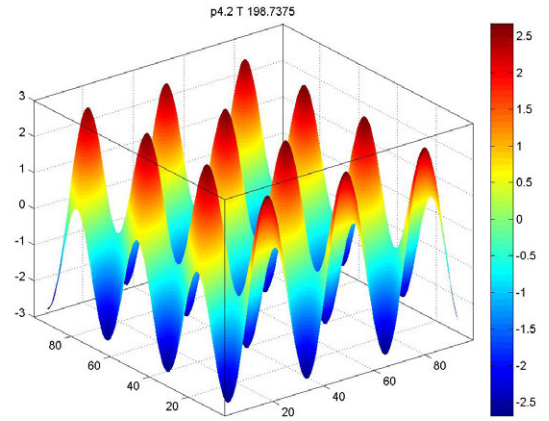
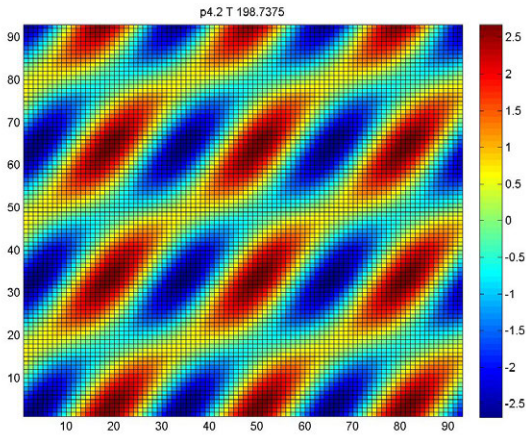


Figure 39: Formations travel downward along a zag oblique path observed when $\phi = 4\pi/20$ and $T = 198.7375$ to $T = 199.9875$ in two (a) and three (b) dimensional representations. The dominant amplitudes are A and D , Figure 55f.



(a)

(b)

Figure 40: Formations traveling downward along a zig oblique path observed when $\phi = 4.2\pi/20$ and $T = 198.7375$ to $T = 199.9875$ in two (a) and three (b) dimensional representations. The dominant amplitudes are B and C , Figure 56a.

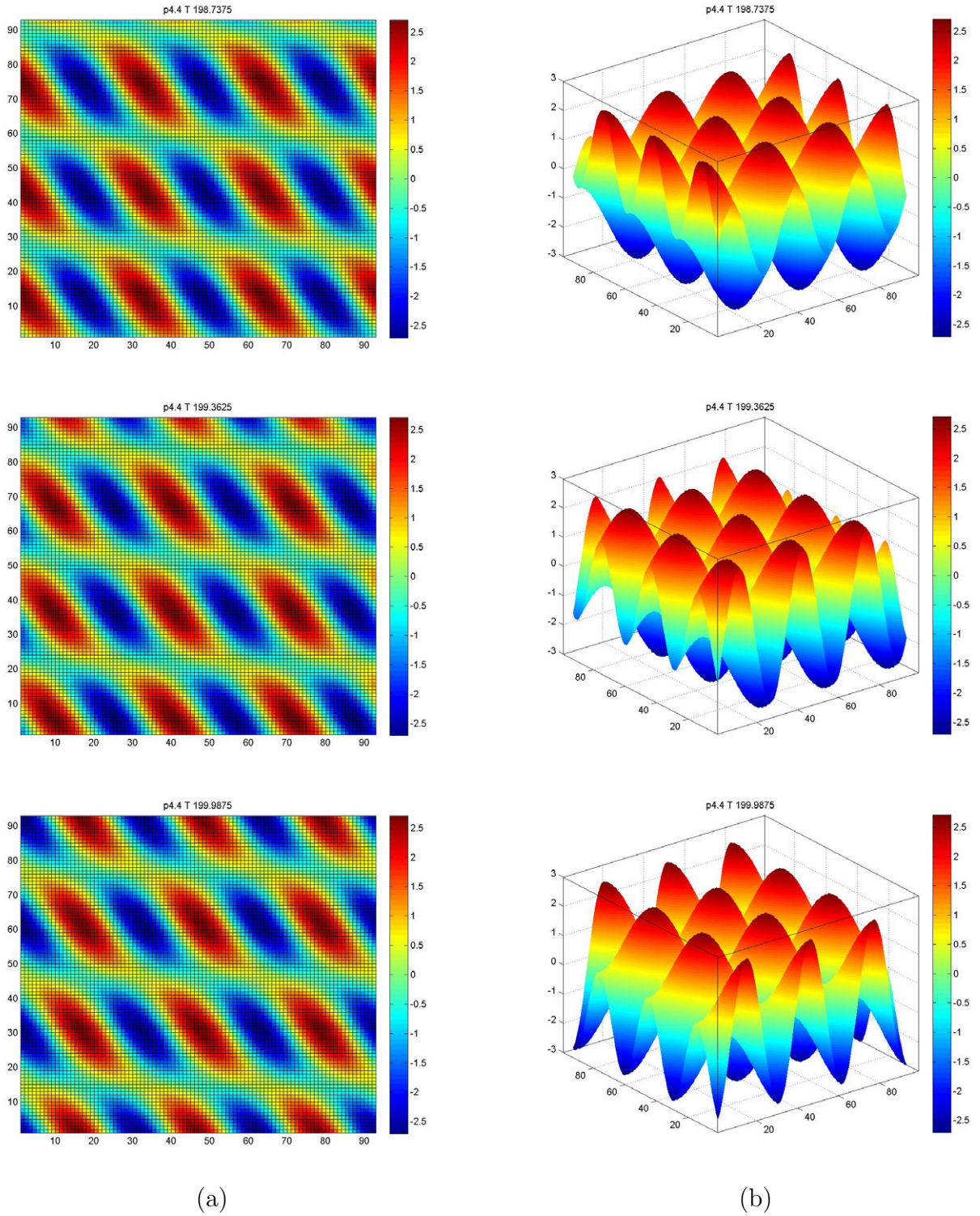


Figure 41: Formations traveling downward along a zig oblique path observed when $\phi = 4.4\pi/20$ and $T = 198.7375$ to $T = 199.9875$ in two (a) and three (b) dimensional representations. The dominant amplitudes are A and D , Figure 56b.

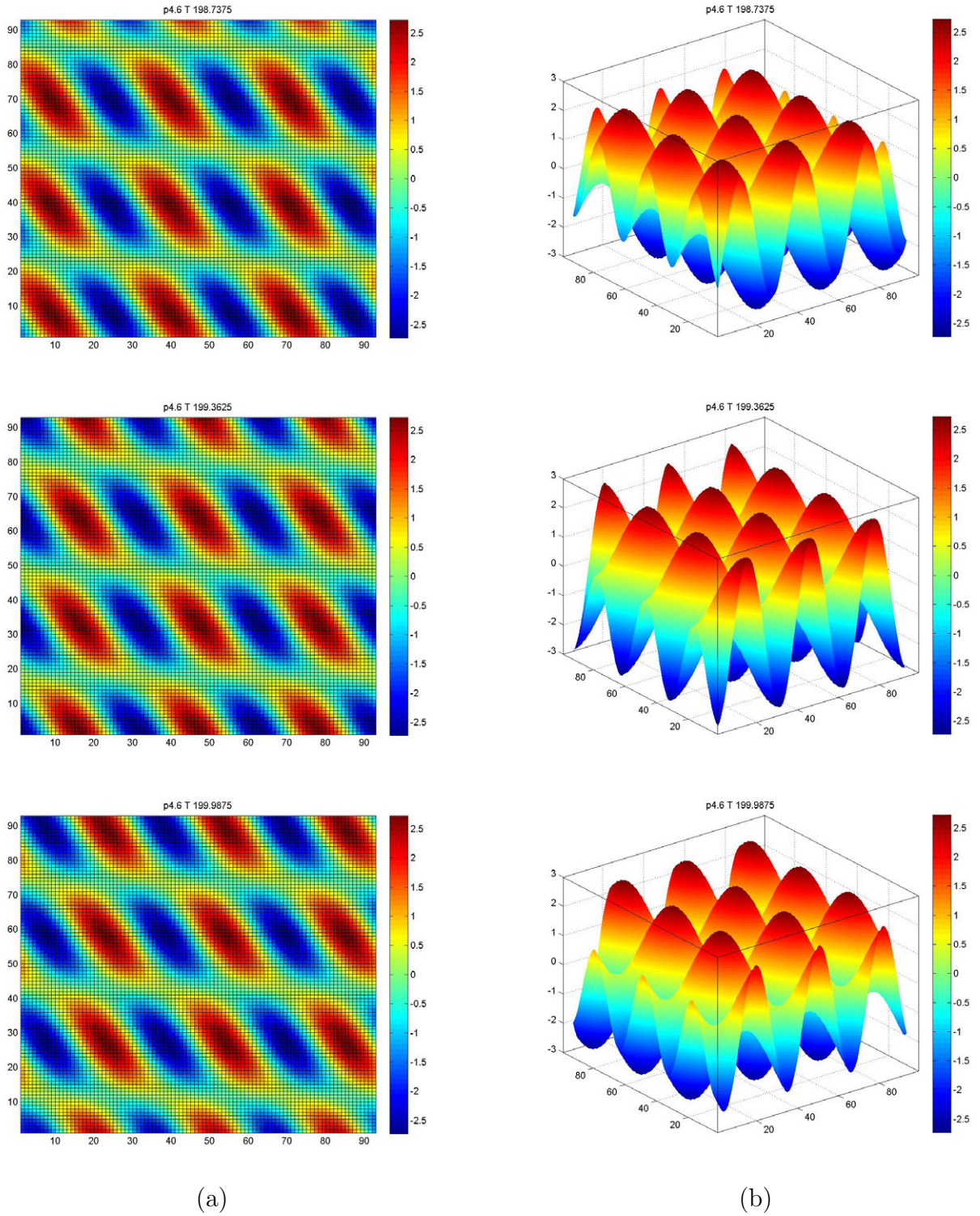


Figure 42: Formations traveling downward along a zig oblique path observed when $\phi = 4.6\pi/20$ and $T = 198.7375$ to $T = 199.9875$ in two (a) and three (b) dimensional representations. The A and D amplitudes are dominant, Figure 56c.

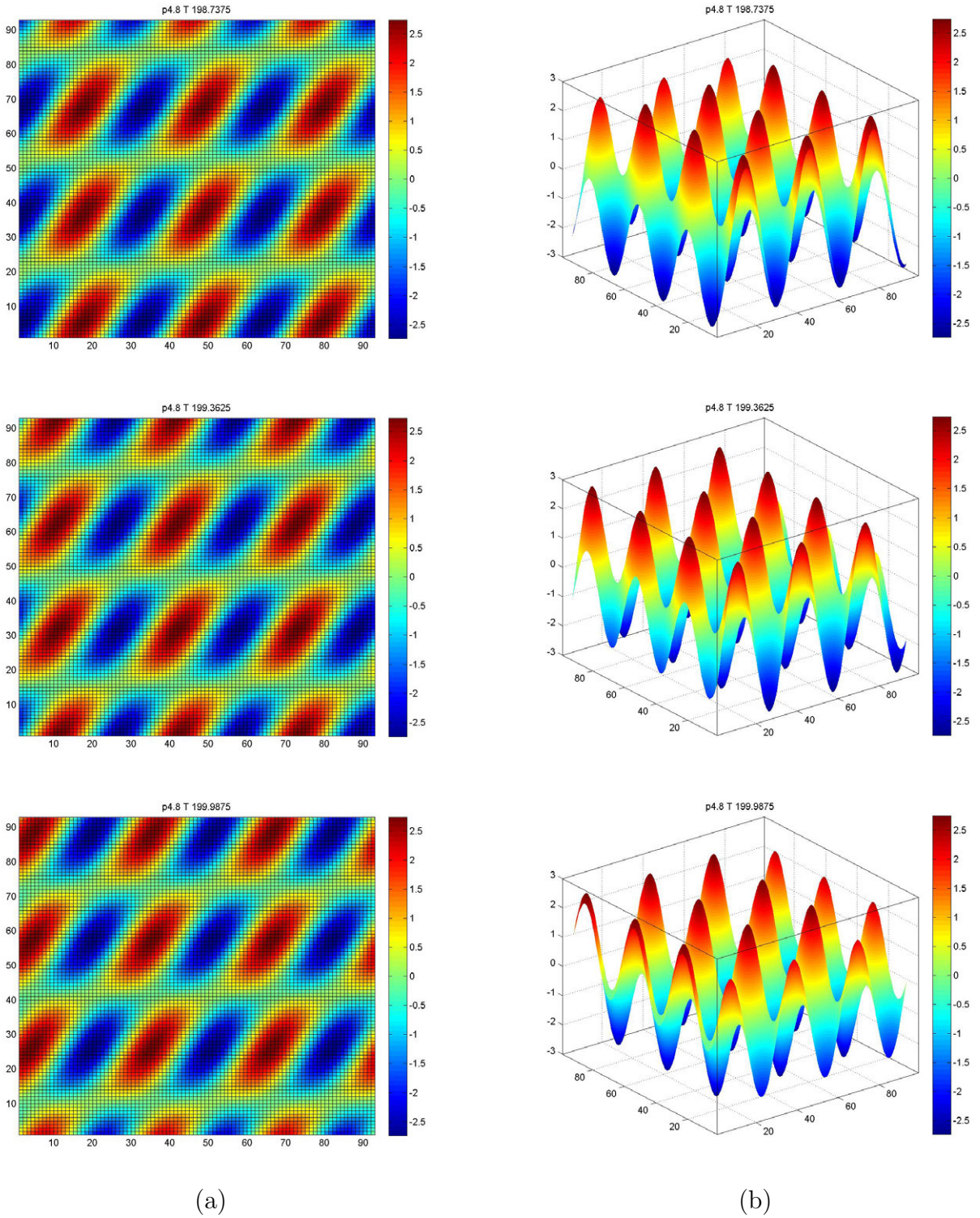


Figure 43: Formations traveling downward along a zig oblique path observed when $\phi = 4.8\pi/20$ and $T = 198.7375$ to $T = 199.9875$ in two (a) and three (b) dimensional representations. The B and C amplitudes are dominant, Figure 56d.

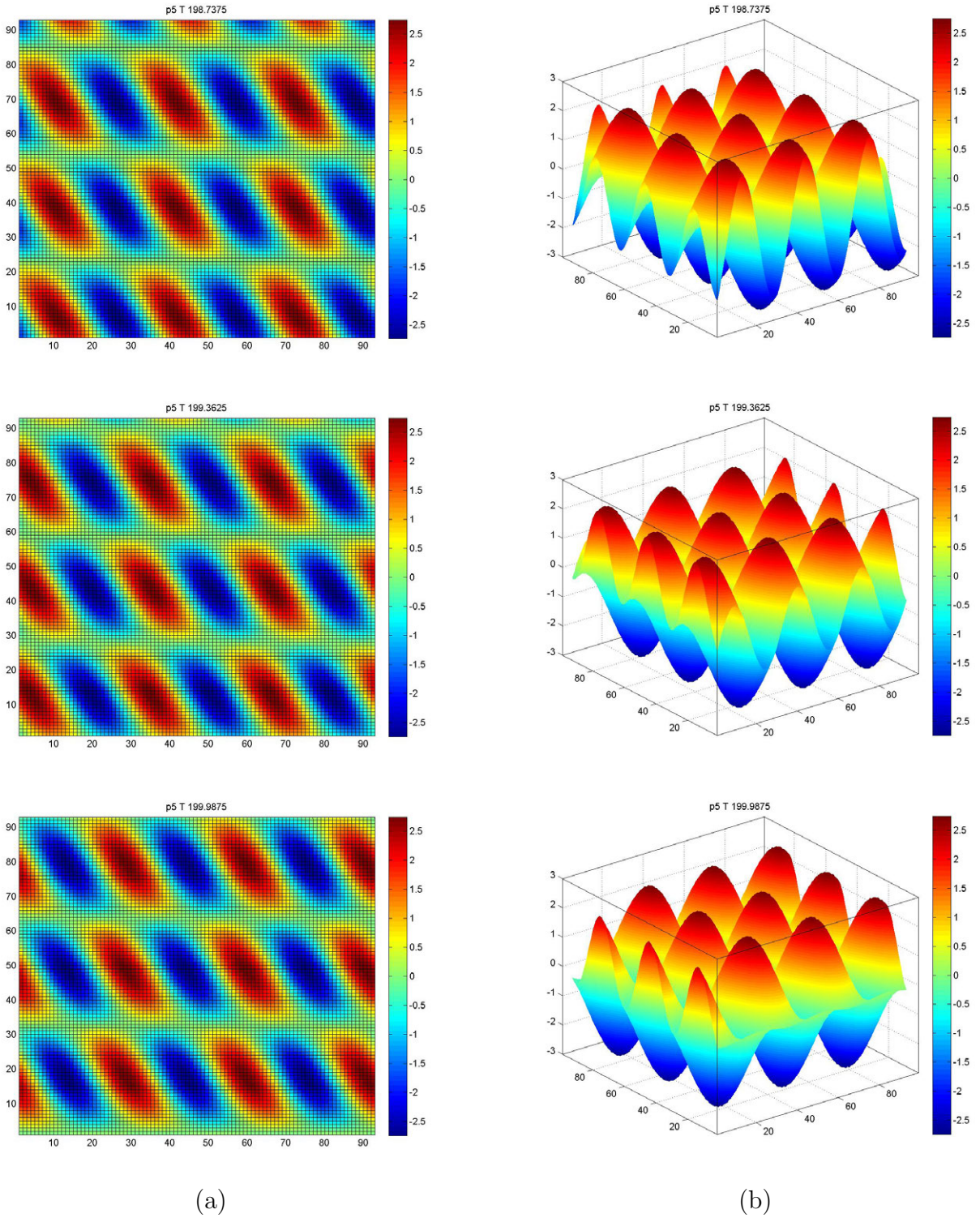
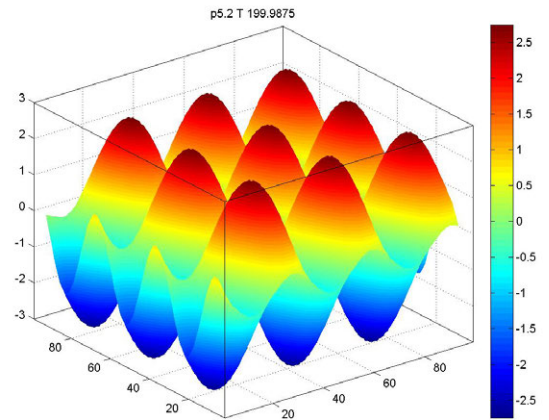
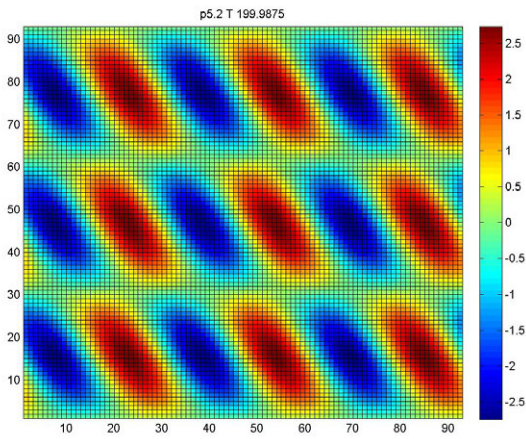
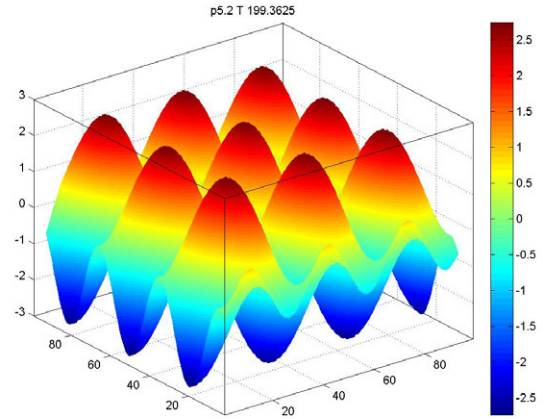
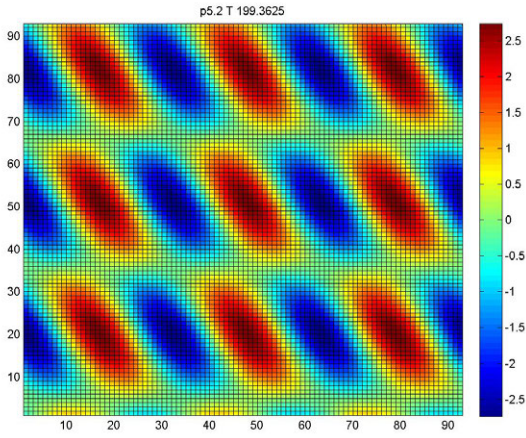
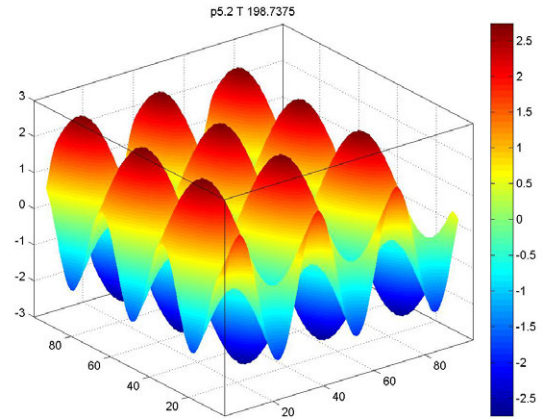
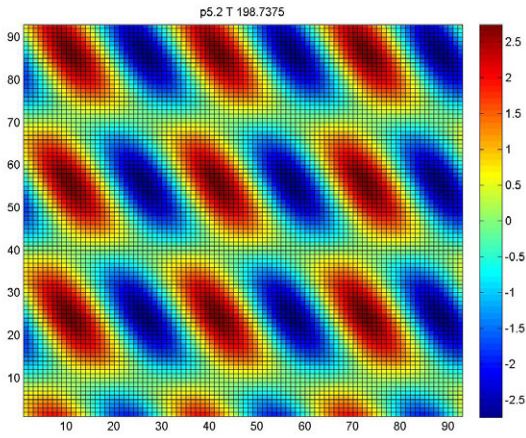


Figure 44: Formations traveling upward along a zag oblique path observed when $\phi = 5\pi/20$ and $T = 198.7375$ to $T = 199.9875$ in two (a) and three (b) dimensional representations. The dominant amplitudes are A and C , Figure 56e.



(a)

(b)

Figure 45: Formations traveling downward along a zag oblique path observed when $\phi = 5.2\pi/20$ and $T = 198.7375$ to $T = 199.9875$ in two (a) and three (b) dimensional representations. The A and D amplitudes are dominant, Figure 56f.

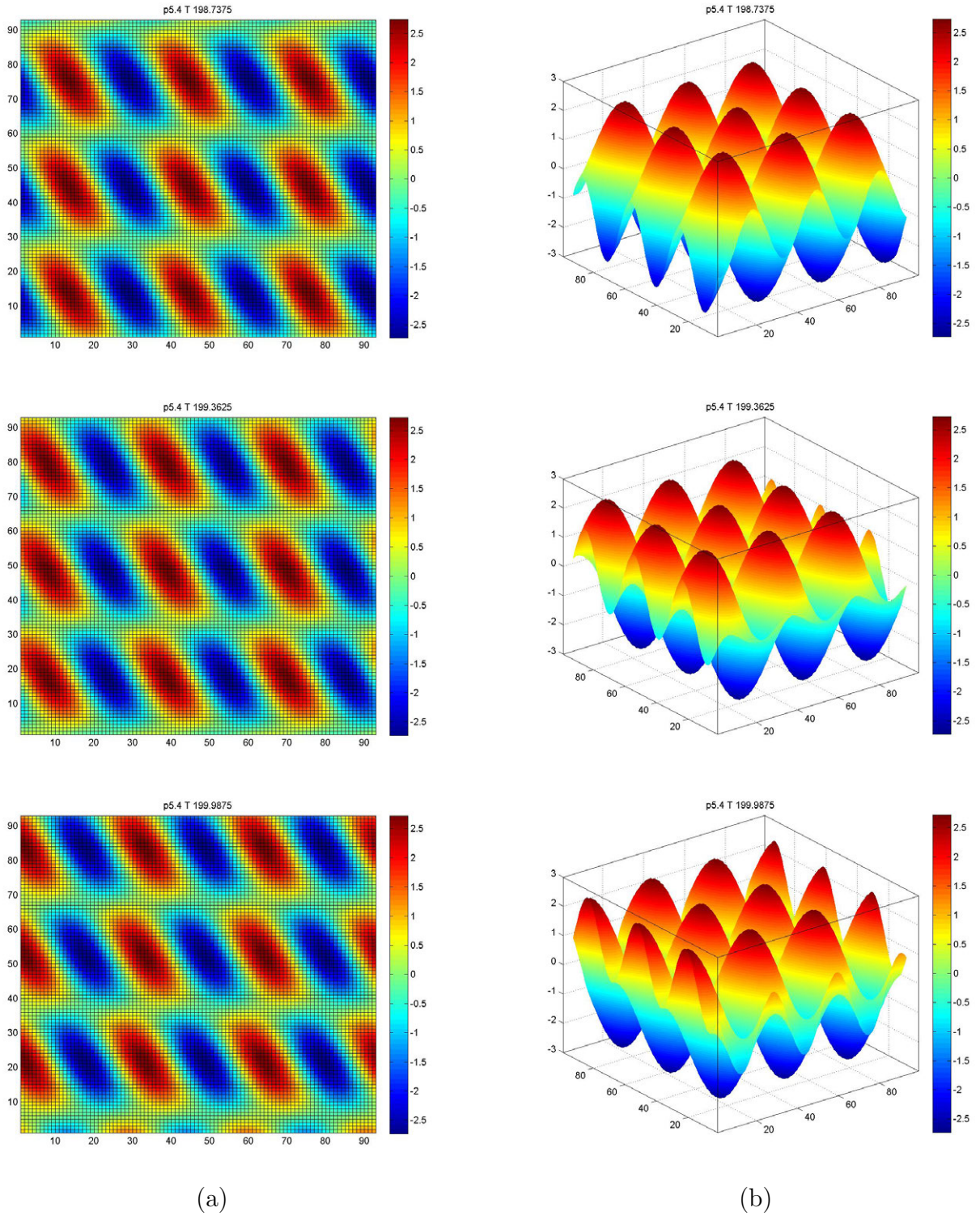
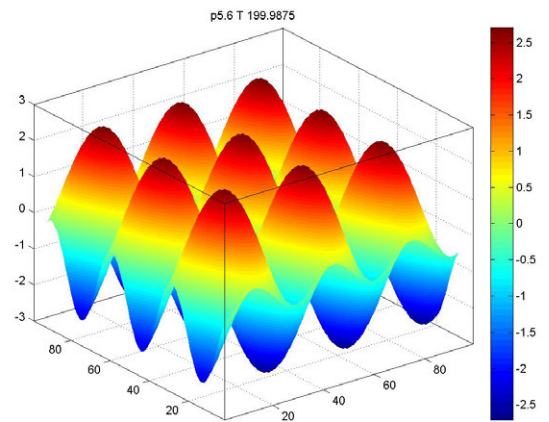
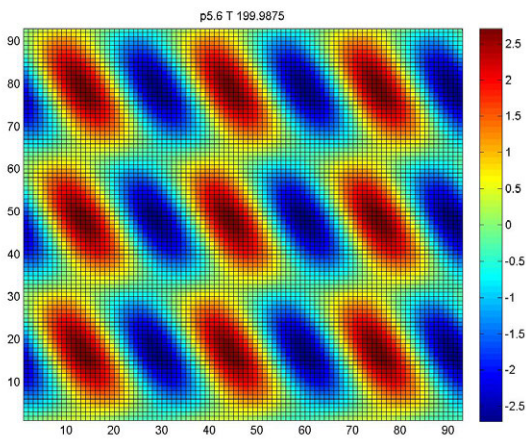
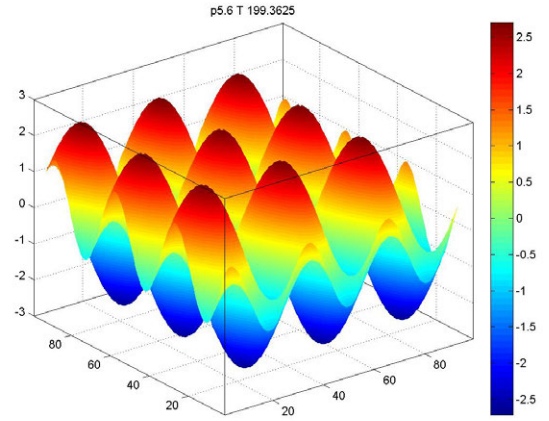
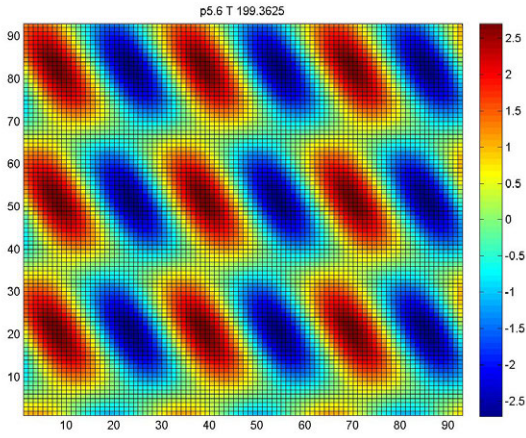
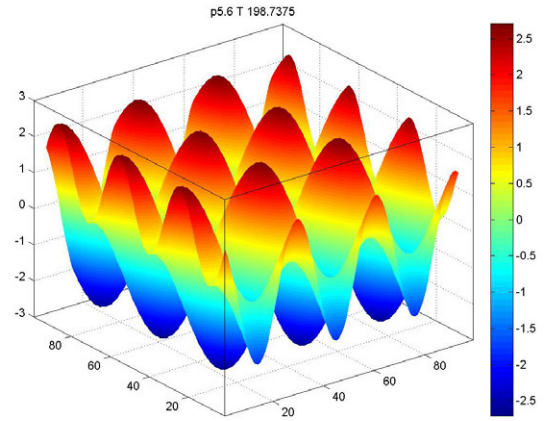
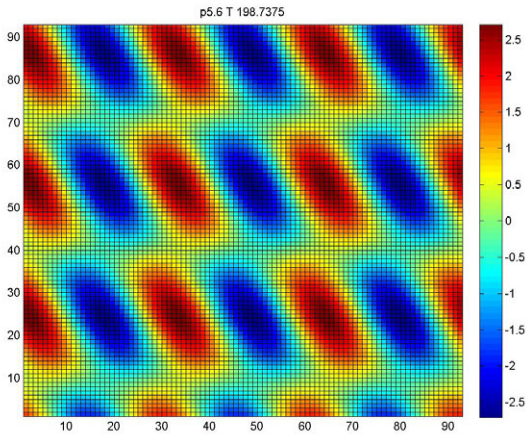


Figure 46: Formations traveling upward along a zag oblique path observed when $\phi = 5.4\pi/20$ and $T = 198.7375$ to $T = 199.9875$ in two (a) and three (b) dimensional representations. The A and C amplitudes are dominant, Figure 57a.



(a)

(b)

Figure 47: Formations traveling downward along a zag oblique path observed when $\phi = 5.6\pi/20$ and $T = 198.7375$ to $T = 199.9875$ in two (a) and three (b) dimensional representations. The dominant amplitudes are A and D , Figure 57b.

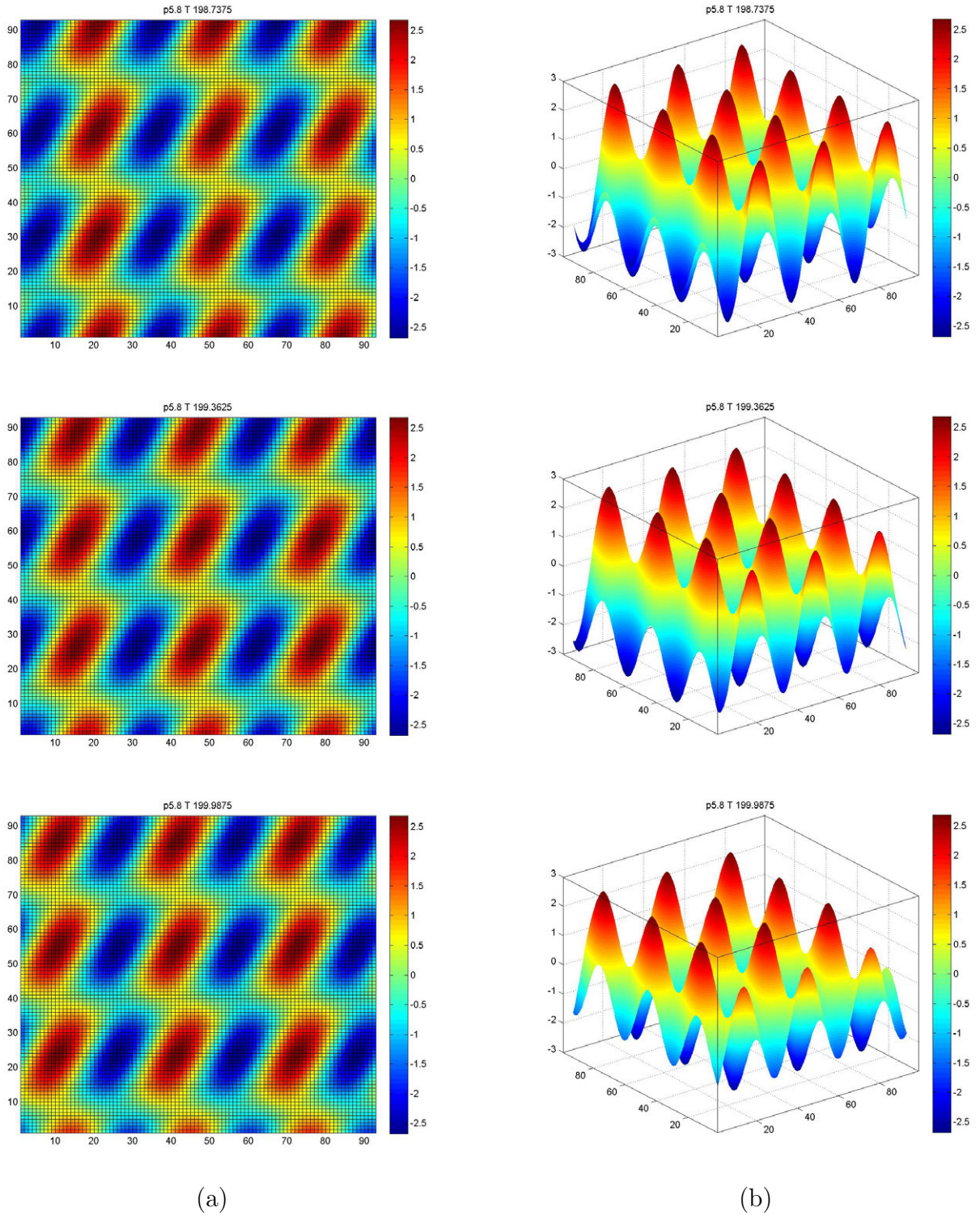


Figure 48: Left traveling normal rolls with a downward moving formation on the extrema observed when $\phi = 5.8\pi/20$ and $T = 198.7375$ to $T = 199.9875$ in two (a) and three (b) dimensional representations. The B and C amplitudes are dominant, Figure 57c.

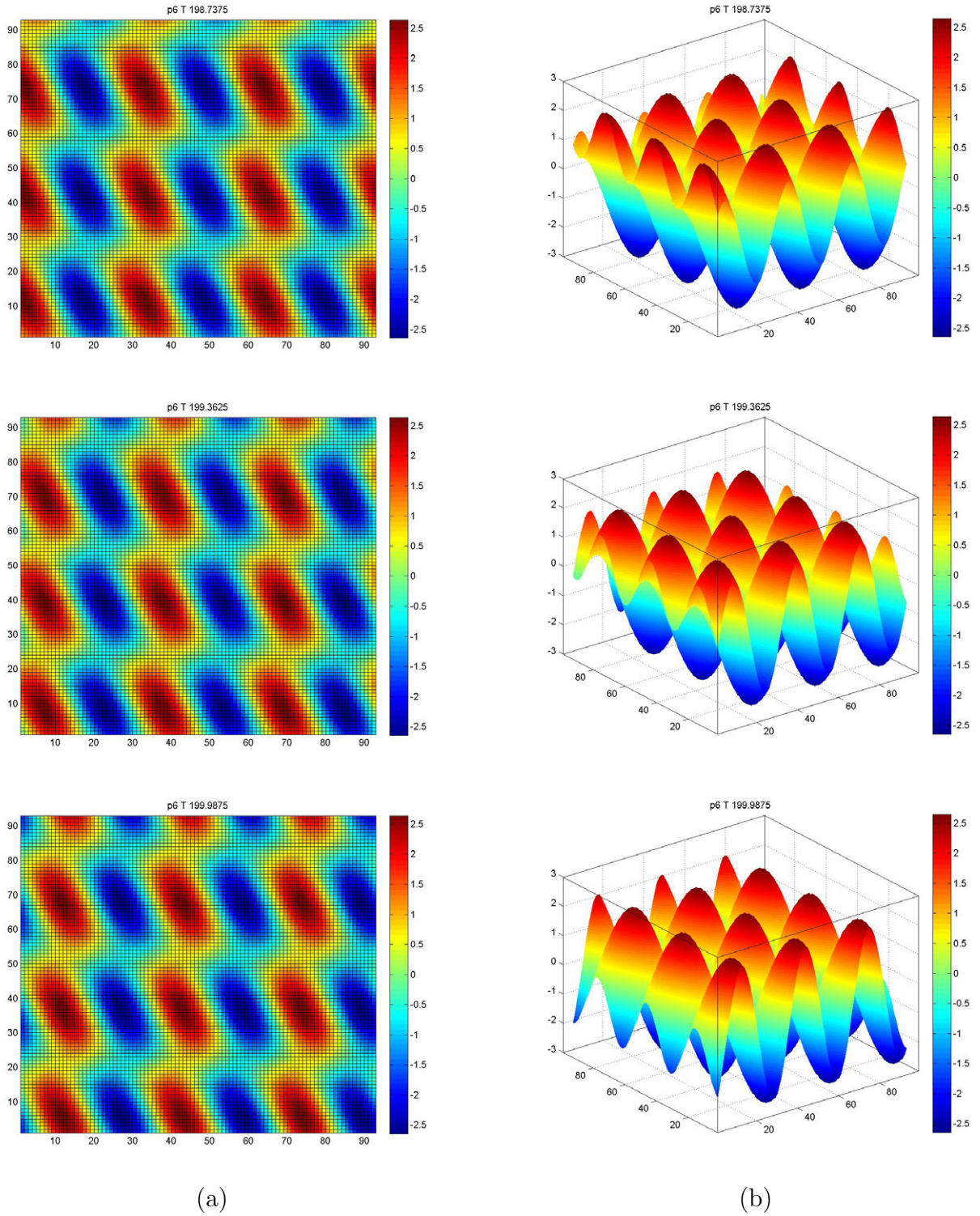


Figure 49: Right traveling normal rolls with a downward moving formation on the extrema observed when $\phi = 6\pi/20$ and $T = 198.7375$ to $T = 199.9875$ in two (a) and three (b) dimensional representations. The dominant amplitudes are A and D , Figure 57d.

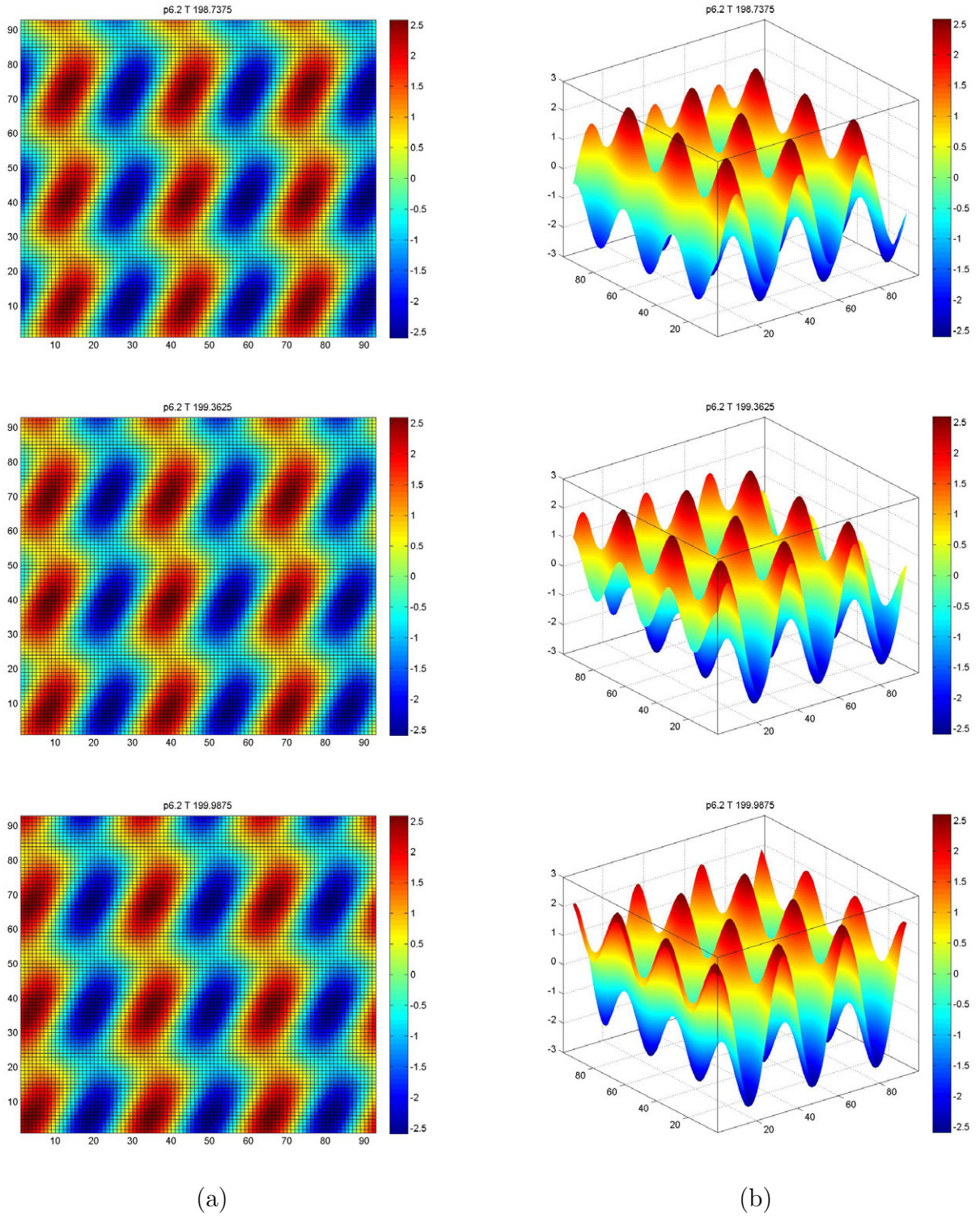


Figure 50: Left traveling normal rolls with a downward moving formation on the extrema observed when $\phi = 6.2\pi/20$ and $T = 198.7375$ to $T = 199.9875$ in two (a) and three (b) dimensional representations. The B and C amplitudes are dominant, Figure 57e.

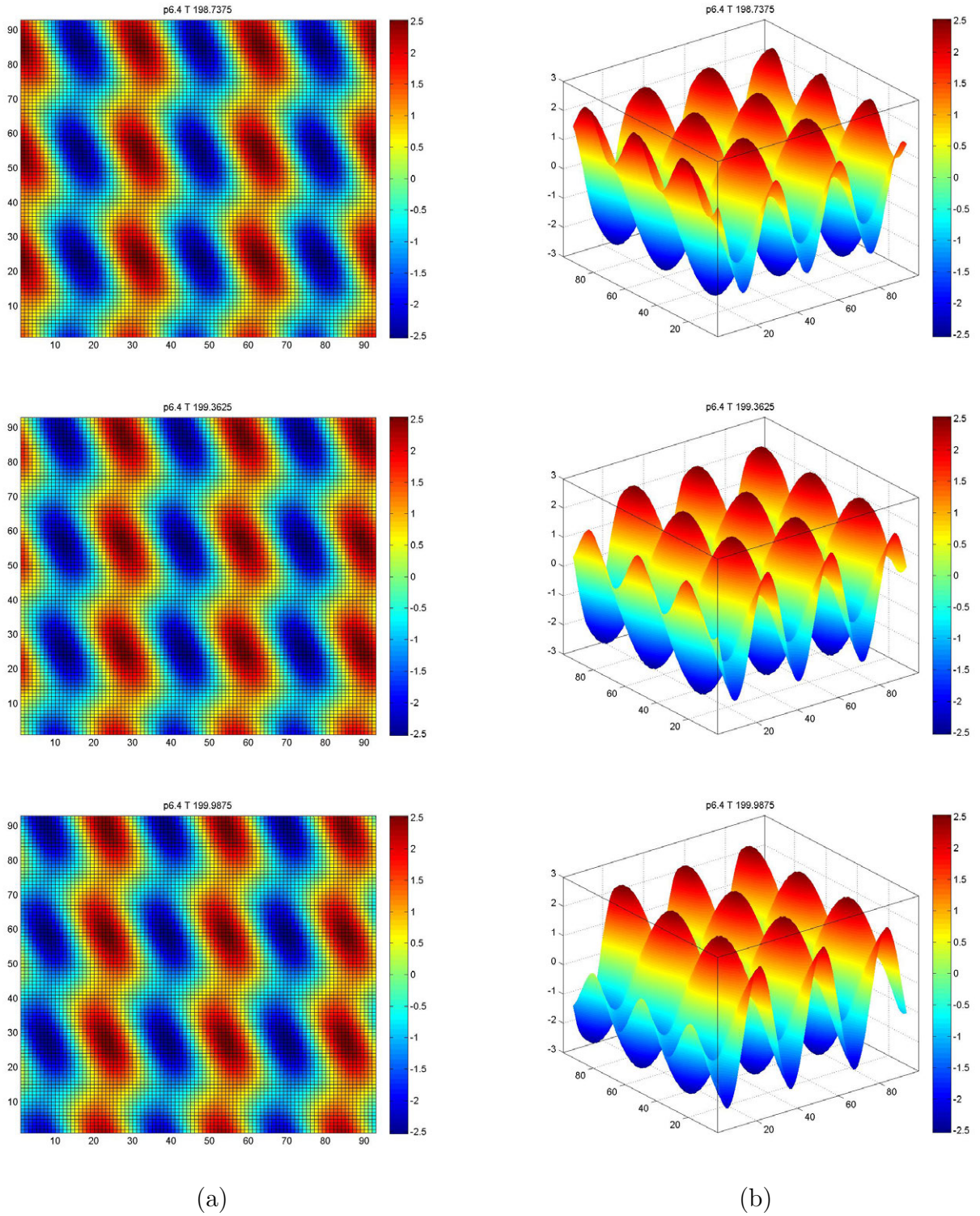


Figure 51: Left traveling normal rolls with an upward moving formation on the extrema observed when $\phi = 6.4\pi/20$ and $T = 198.7375$ to $T = 199.9875$ in two (a) and three (b) dimensional representations. The dominant amplitudes are A and C , Figure 57f.

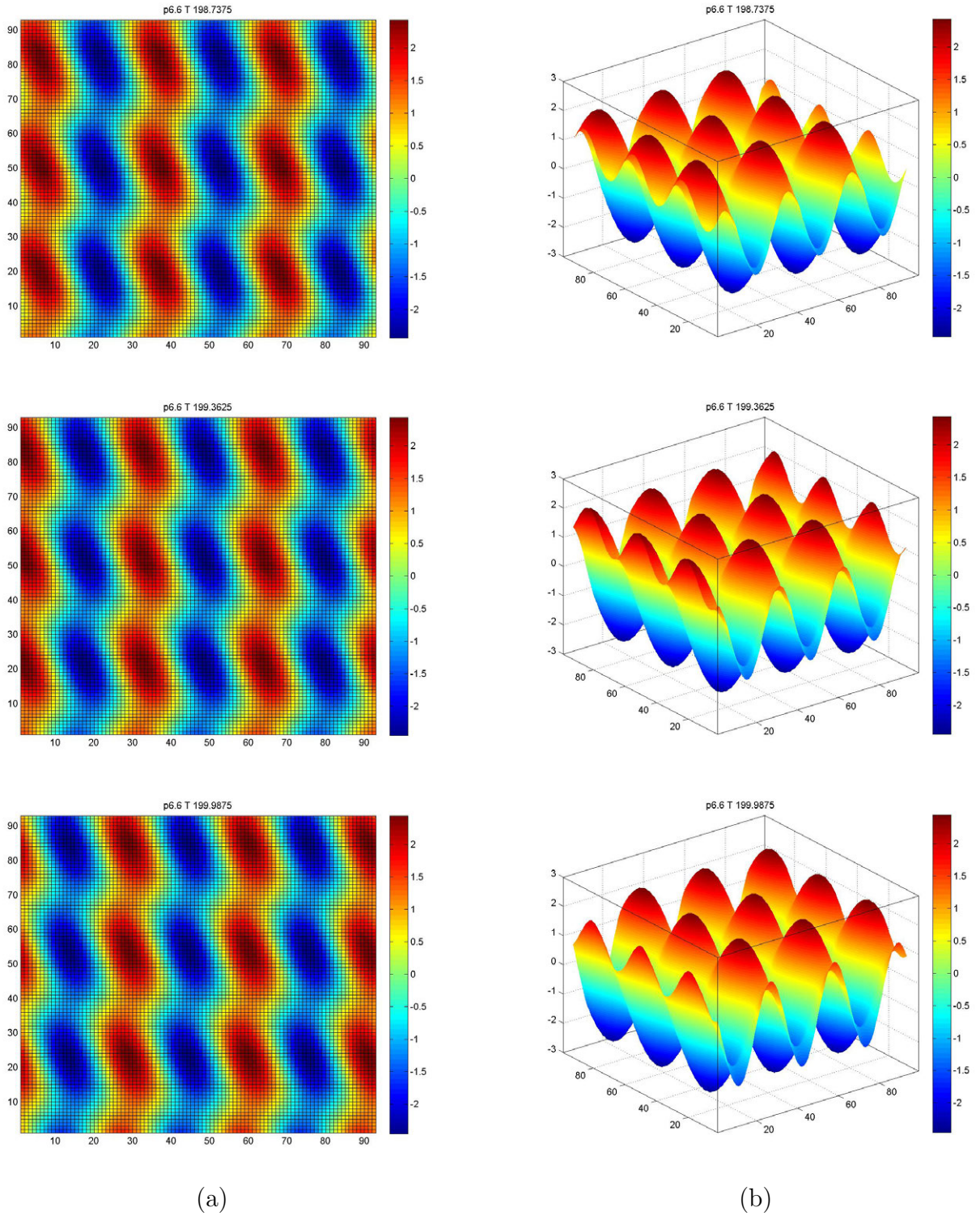


Figure 52: Left traveling normal rolls with an upward moving formation on the extrema observed when $\phi = 6.6\pi/20$ and $T = 198.7375$ to $T = 199.9875$ in two (a) and three (b) dimensional representations. The A and C amplitudes are dominant, Figure 58a.

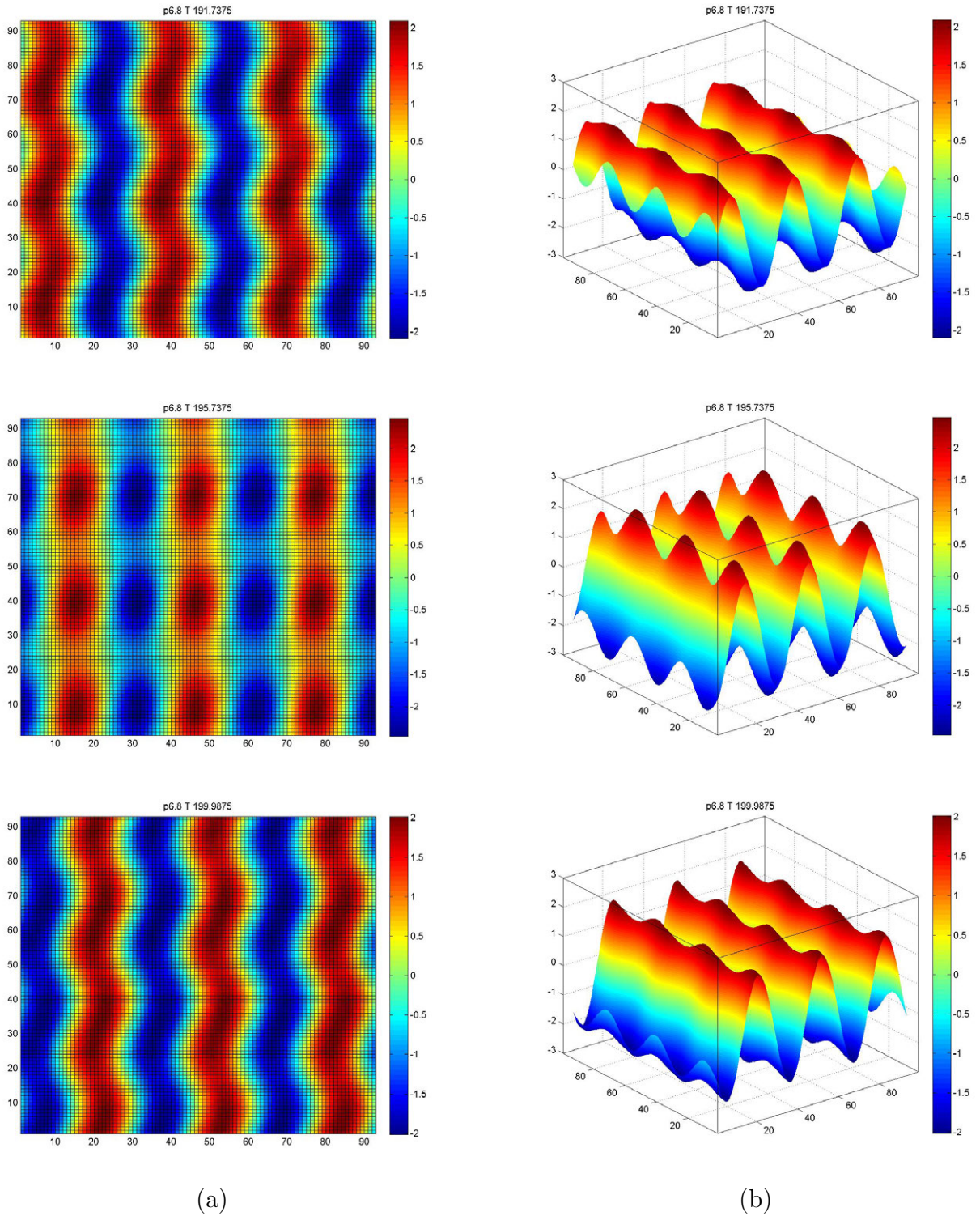


Figure 53: Left traveling normal rolls with a formation on the extrema observed when $\phi = 6.8\pi/20$ and $T = 191.7375$ to $T = 199.9875$ in two (a) and three (b) dimensional representations. The C amplitude is dominant, but there is some influence from the A and B amplitudes, Figure 58b.

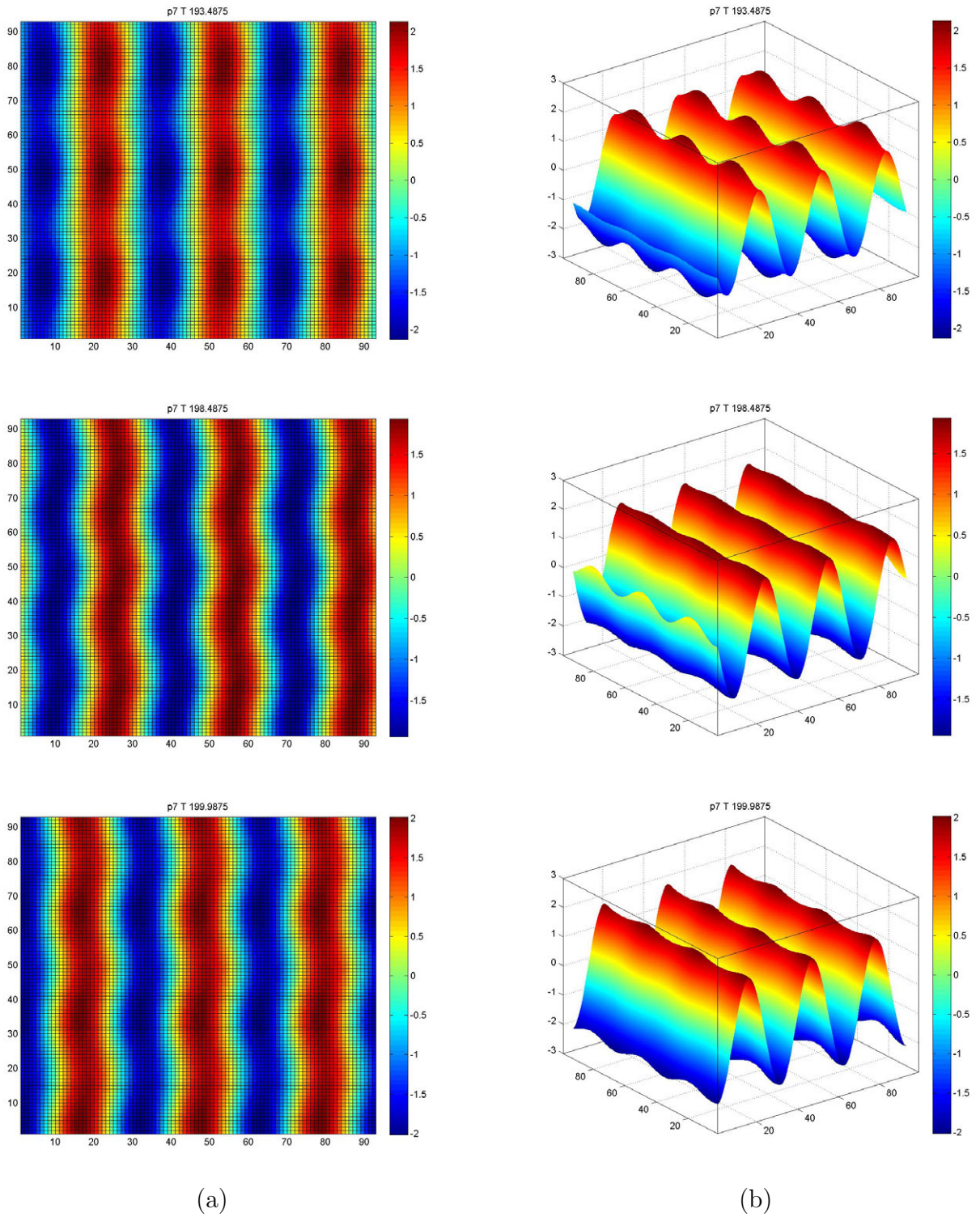
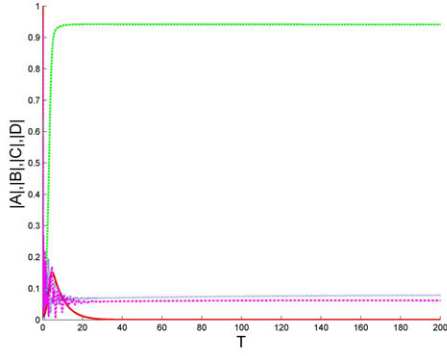
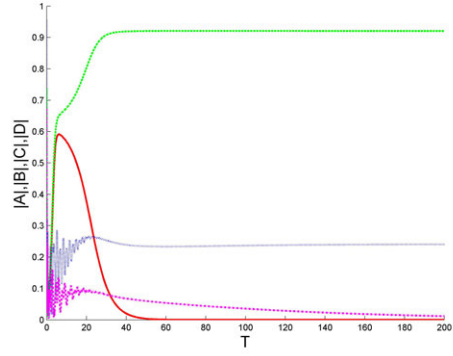


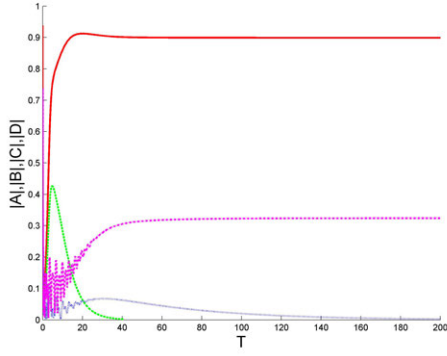
Figure 54: Left traveling normal rolls with a formation on the extrema observed when $\phi = 7\pi/20$ and $T = 193.4875$ to $T = 199.9875$ in two (a) and three (b) dimensional representations. The C amplitude is dominant, but there is some influence from the A and B amplitudes, Figure 58c.



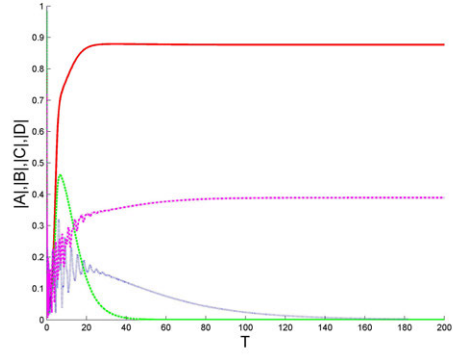
(a) Time series for $n = 3$. The magnitude of the amplitudes (A, B, C, D) are $(O(10^{-11}), 0.9413, 0.0783, 0.0616)$.



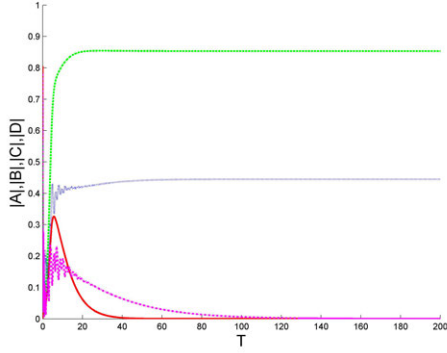
(b) Time series for $n = 3.2$. The magnitude of the amplitudes (A, B, C, D) are $(O(10^{-11}), 0.9205, 0.2406, 0.0117)$.



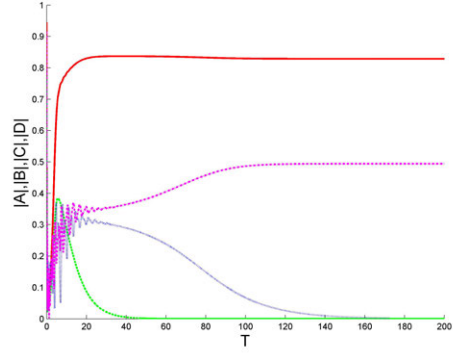
(c) Time series for $n = 3.4$. The magnitude of the amplitudes (A, B, C, D) are $(0.8991, O(10^{-14}), 0.0025, 0.3239)$.



(d) Time series for $n = 3.6$. The magnitude of the amplitudes (A, B, C, D) are $(0.8767, O(10^{-13}), 0.0012, 0.3893)$.

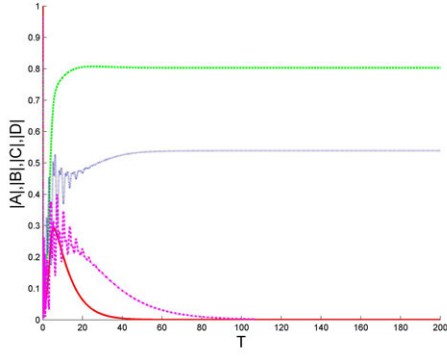


(e) Time series for $n = 3.8$. The magnitude of the amplitudes (A, B, C, D) are $(O(10^{-11}), 0.8533, 0.4450, O(10^{-4}))$.

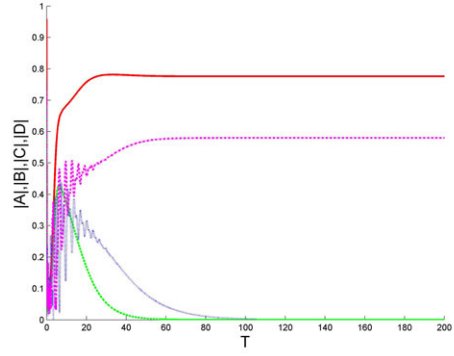


(f) Time series for $n = 4$. The magnitude of the amplitudes (A, B, C, D) are $(0.8288, O(10^{-12}), O(10^{-4}), 0.4943)$.

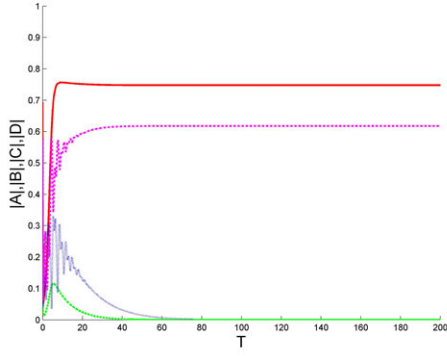
Figure 55: A time series of the magnitude of the amplitudes at a specific spatial point when $\phi = n\pi/20$. The time series for the moduli of the (A, B, C, D) amplitudes is depicted as a solid red line, a dashed green line, a dotted blue line, and a dash-dot magenta line, respectively.



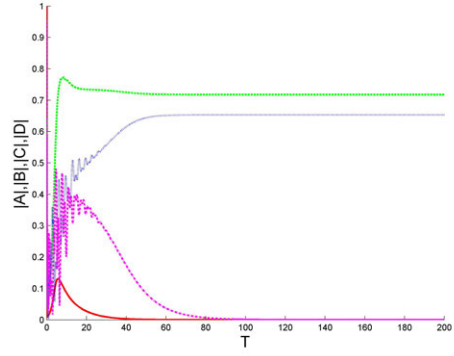
(a) Time series for $n = 4.2$. The magnitude of the amplitudes (A, B, C, D) are $(O(10^{10}), 0.8031, 0.5389, O(10^6))$.



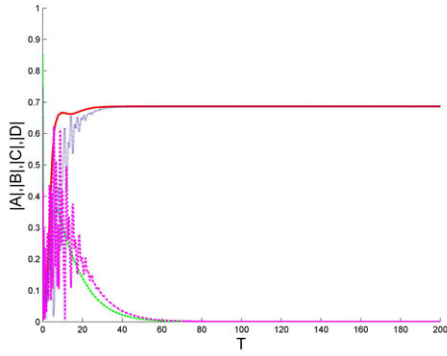
(b) Time series for $n = 4.4$. The magnitude of the amplitudes (A, B, C, D) are $(0.7761, O(10^{-11}), O(10^{-6}), 0.5798)$.



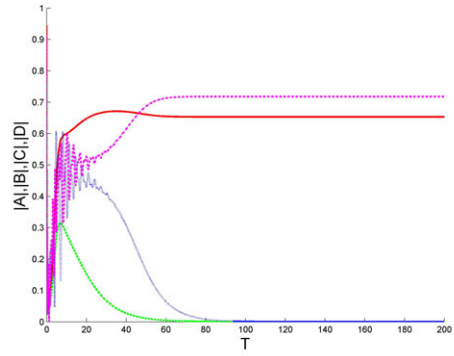
(c) Time series for $n = 4.6$. The magnitude of (A, B, C, D) are $(0.7478, O(10^{-11}), O(10^{-7}), 0.6178)$.



(d) Time series for $n = 4.8$. The magnitude of the amplitudes (A, B, C, D) are $(O(10^{-10}), 0.7180, 0.6533, O(10^{-7}))$.

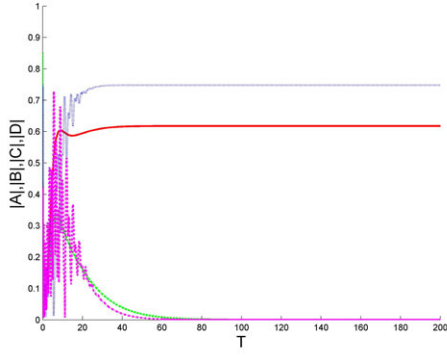


(e) Time series for $n = 5$. The magnitude of the (A, B, C, D) are $(0.6866, O(10^{-9}), 0.6866, O(10^{-9}))$.

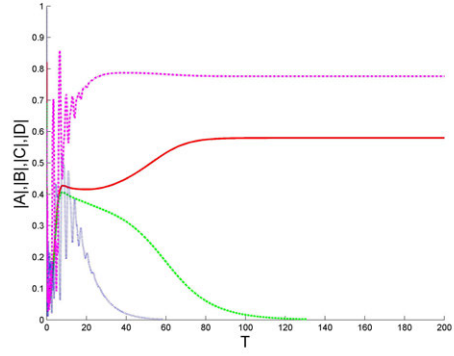


(f) Time series for $n = 5.2$. The magnitude of the (A, B, C, D) are $(0.6533, O(10^{-8}), O(10^{-8}), 0.7180)$.

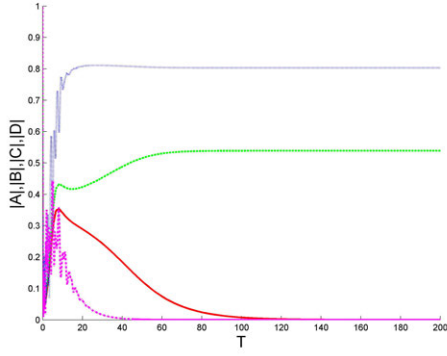
Figure 56: A time series of the magnitude of the amplitudes at a specific spatial point when $\phi = n\pi/20$. The time series for the moduli of the (A, B, C, D) amplitudes is depicted as a solid red line, a dashed green line, a dotted blue line, and a dash-dot magenta line, respectively.



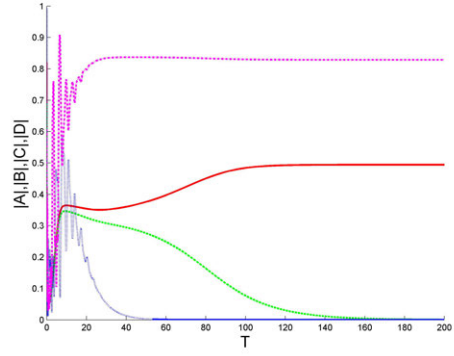
(a) Time series for $n = 5.4$. The magnitude of the (A, B, C, D) are $(0.6178, O(10^{-7}), 0.7478, O(10^{-10}))$.



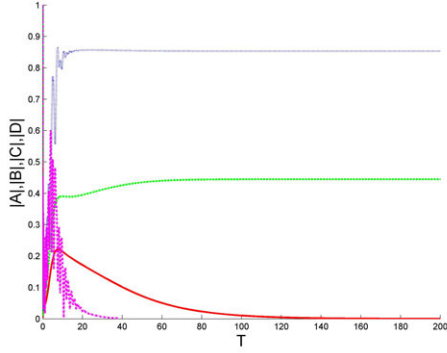
(b) Time series for $n = 5.6$. The magnitude of the (A, B, C, D) are $(0.5798, O(10^{-5}), O(10^{-11}), 0.7761)$.



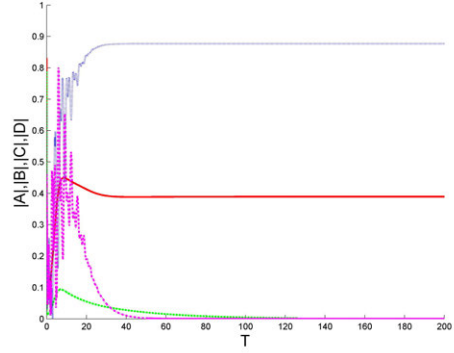
(c) Time series for $n = 5.8$. The magnitude of the amplitudes (A, B, C, D) are $(O(10^{-5}), 0.5389, 0.8031, O(10^{-12}))$.



(d) Time series for $n = 6$. The magnitude of the (A, B, C, D) are $(0.4943, O(10^{-4}), O(10^{-12}), 0.8288)$.

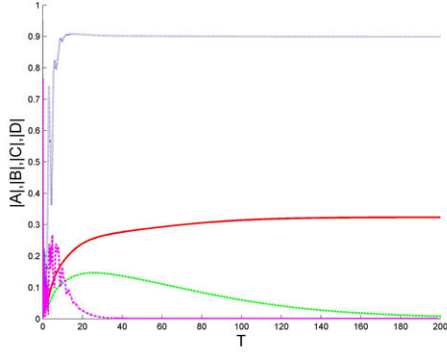


(e) Time series for $n = 6.2$. The magnitude of the (A, B, C, D) are $(O(10^{-4}), 0.4450, 0.8533, O(10^{-13}))$.

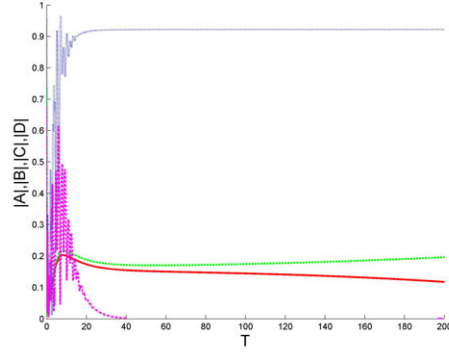


(f) Time series for $n = 6.4$. The magnitudes of the (A, B, C, D) amplitudes being $(0.3893, O(10^{-4}), 0.8767, O(10^{-13}))$.

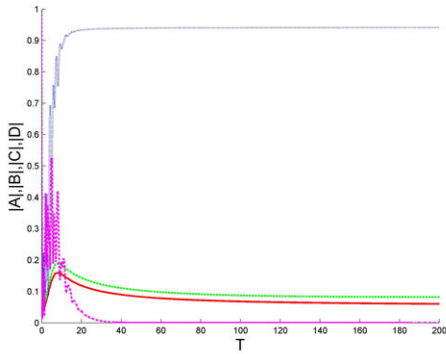
Figure 57: A time series of the magnitude of the amplitudes at a specific spatial point when $\phi = n\pi/20$. The time series for the moduli of the (A, B, C, D) amplitudes is depicted as a solid red line, a dashed green line, a dotted blue line, and a dash-dot magenta line, respectively.



(a) Time series for $n = 6.6$. The magnitude of the (A, B, C, D) are $(0.3237, 0.0080, 0.8991, O(10^{-15}))$.



(b) Time series for $n = 6.8$. The magnitudes of (A, B, C, D) are $(0.1177, 0.1964, 0.9220, O(10^{-15}))$.



(c) Time series for $n = 7$. The magnitude of the (A, B, C, D) amplitudes are $(0.0604, 0.0823, 0.9412, O(10^{-16}))$.

Figure 58: A time series of the magnitude of the amplitudes at a specific spatial point when $\phi = n\pi/20$. The time series for the moduli of the (A, B, C, D) amplitudes is depicted as a solid red line, a dashed green line, a dotted blue line, and a dash-dot magenta line, respectively.

4.3 Bifurcation Diagram in the (c_r, ϕ) plane

In order to explore the behavior of the solutions in the $c_r - \phi$ plane, the parameters

$$(a, b_1, b_2, c_i, d, \Omega) = (1.2, 1 + 1.2i, 1.2 + i, 1, -0.5 + i, 5), \quad (100)$$

the diffusion coefficients

$$(\delta, \alpha, \beta) = (0.1, 0.02 + 0.2i, 0.02 - 0.4i), \quad (101)$$

and $p_c = q_c = w_c = k_c = v_c = 1.00$ were fixed and (c_r, ϕ) was allowed to vary. The parameter c_r was cycled through the set $\{n/2, n = -9, -8, \dots, 4\}$ and ϕ was cycled through the set $\{n\pi/20, n = -10, -9, \dots, 30\}$.

The behavior of the numerical solutions in the c_r, ϕ -plane is shown in Figure 59. The

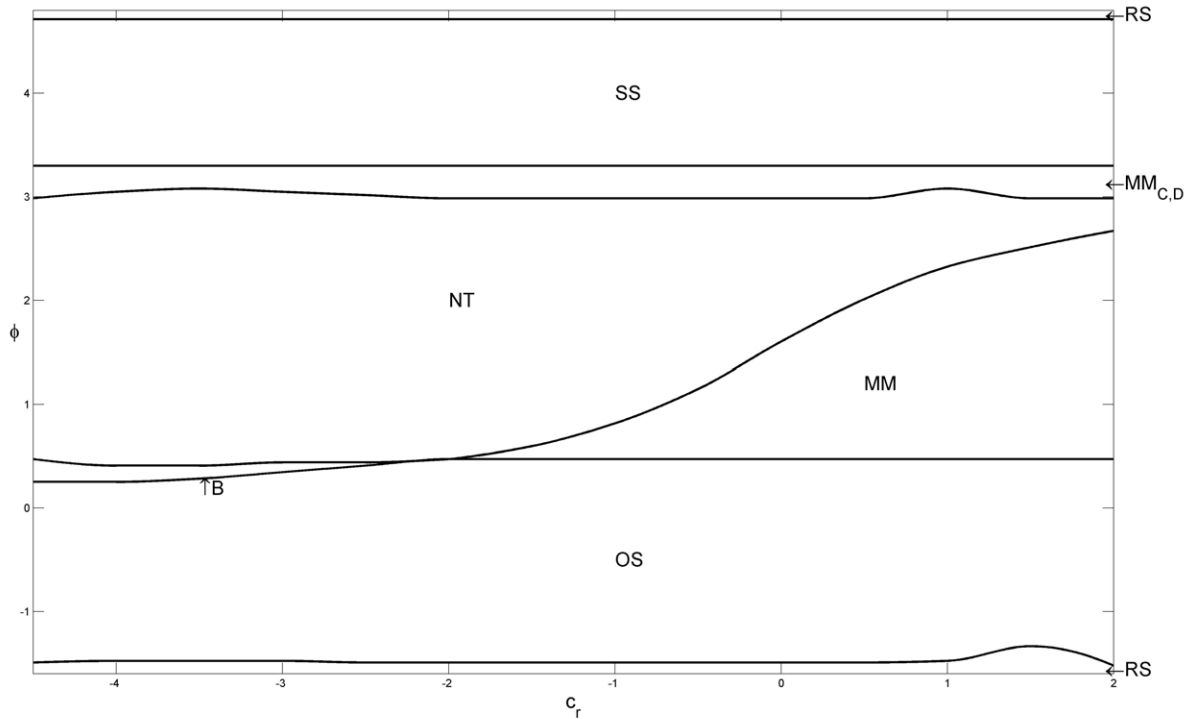


Figure 59: Bifurcation diagram in the (c_r, ϕ) plane.

steady state solutions (SS) occur in the region where $\pi < \phi < 3\pi/2$ as seen in Figure 59. Also, Figure 59 shows regions of stable steady oblique rolls (OS), normal traveling rolls (NT), and mixed mode solutions (MM). For $c_r \in \{n/2, n = -4, -3, \dots, 4\}$ the mixed mode solutions are stable and for $c_r \in \{n/2, n = -9, -8, \dots, -5\}$ bistability of the normal traveling and the steady oblique rolls exists.

The behavior designated with *RS* occurring at and slightly above $\phi = -\pi/2$ and at $\phi = 3\pi/2$ are steady rectangles, Figure 23, resulting from a superposition of the two steady oblique modes. The region designated by $MM_{C,D}$ has (C, D) mixed mode solutions and further investigation is needed to quantify these solutions. The last region of stable mixed mode solutions, designated by *MM* and occurring for $-2 \leq c_r \leq 1.5$ is composed of (A, C) , (A, D) , (B, C) , and (B, D) mixed mode solutions. The solution is a superposition of one steady oblique mode and one normal traveling mode. The region denoted by *B* where $-4.5 \leq c_r \leq -2$ is where bistability of the steady oblique rolls and the normal traveling rolls has been observed.

On the border between the regions of the *MM* solutions and the *OS* solutions there are mixed mode solutions consisting of a superposition of three modes, one steady oblique mode and both normal traveling modes. At the other border of the *MM* region, between the *MM* and the *NT* solutions, there is another region of mixed modes combining three different modes, this time the (A, B) modes and either the *C* or *D* mode.

The ‘pure’ mixed modes and the combinations of three modes were interesting mixed mode structures and require further investigation.

4.4 Consistency of Numerical and Theoretical Results

The behavior of the numerical simulations has been consistent with the normal form analysis except for near the theoretical bifurcation lines, $\phi = -\pi/2$ and $\phi = \pi$, where stable ‘pure’ mixed mode solutions were observed. These mixed mode solutions were unstable in the normal form analysis. For all values of c_r used, at $\phi = -\pi/2$ a steady rectangles solution

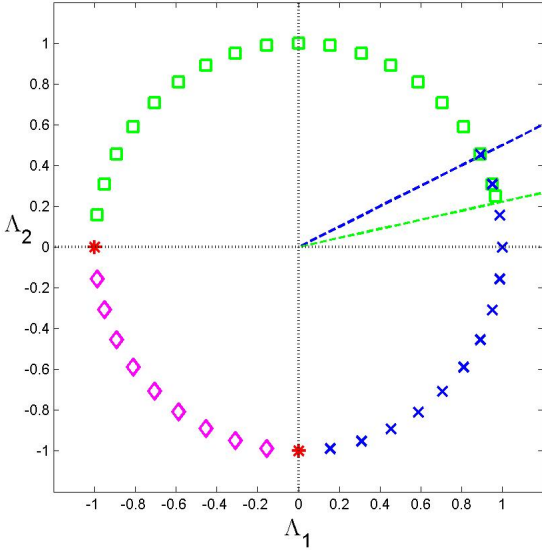
with amplitude of $O(10^{-2})$ was seen and for $\phi = \pi$ a (C, D) mixed mode solution with amplitude of $O(10^{-1})$ was observed.

In all cases, Figures 60a - 63b, the steady oblique rolls, normal traveling rolls, and steady state solution are only observed within the regions where the theory indicates that they are stable.

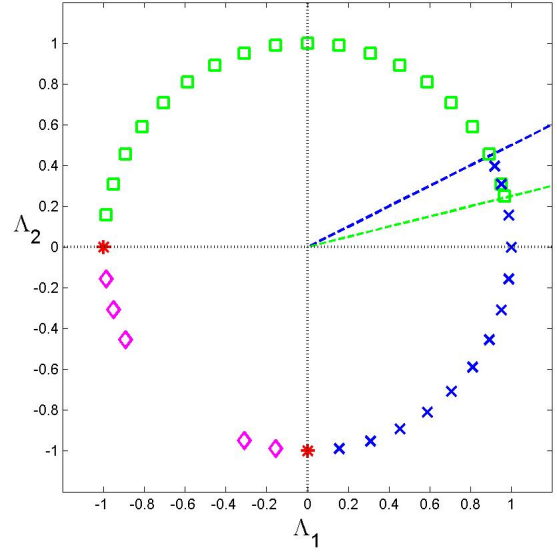
The bistability regions found numerically in Figures 60a - 61a agree with the predictions from the normal form analysis. Bistability of the steady oblique and normal traveling rolls has yet to be found at the theoretical limits. As $c_r < -2$ decreases the bistability of the steady oblique and normal traveling solutions are observed for a larger number of ϕ values.

The steady oblique-normal traveling mixed mode solutions were observed where predicted, Figures 61b - 63b, and usually from one theoretical bifurcation line to the other of the expected region. For $c_r = -2$, the theoretical bifurcation half-lines, (O) and (N), overlap. An (A, C) , (A, D) , (B, C) , or (B, D) mixed mode solution was observed in the ‘wedge’ in the parameter plane where the normal form has the mixed mode solution. As $c_r > -2$ increases the mixed mode solution is observed for a larger number of ϕ values.

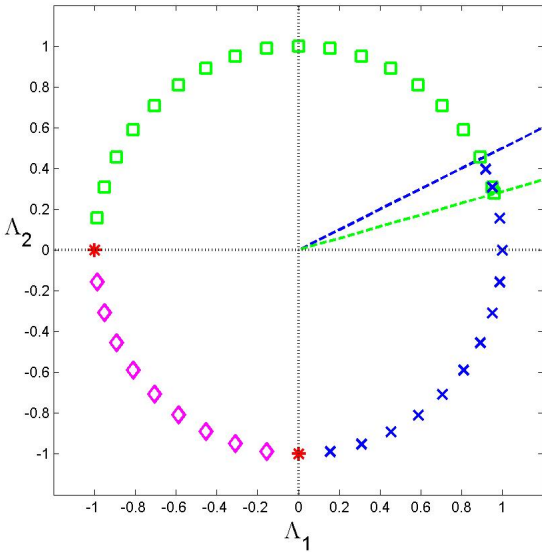
There are stable mixed mode solutions consisting of three non-zero amplitudes along the theoretical bifurcation half-lines (O) and (N) for $c_r \in \{-1.5, -1, -0.5, 0, 0.5, 1, 1.5, 2\}$. These solutions consist of either the A or B mode and the (C, D) modes near the (O) half-line and either the C or D mode and the (A, B) modes near the (N) half-line.



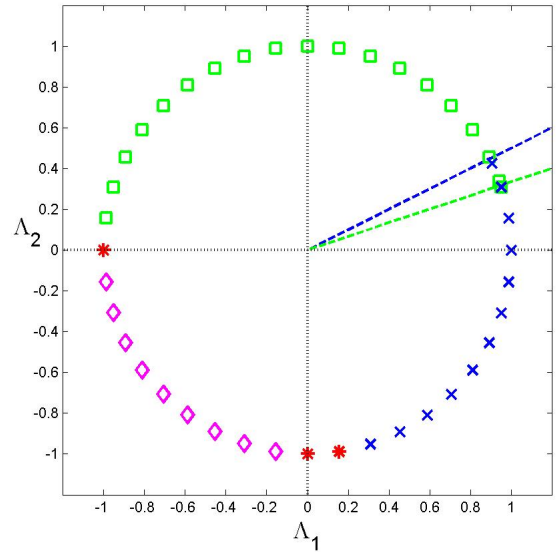
(a) $c_r = -4.5$



(b) $c_r = -4$

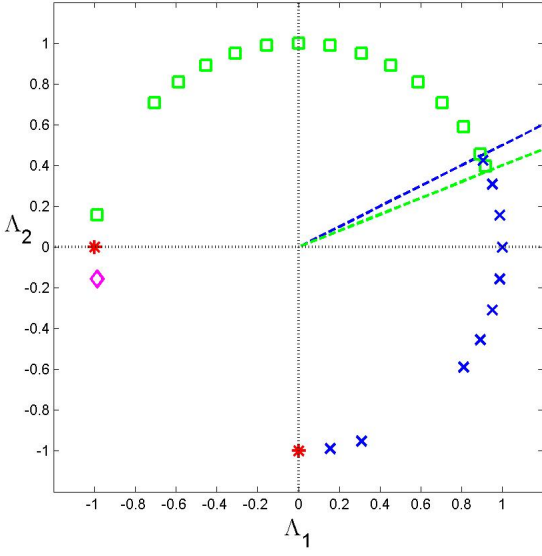


(c) $c_r = -3.5$

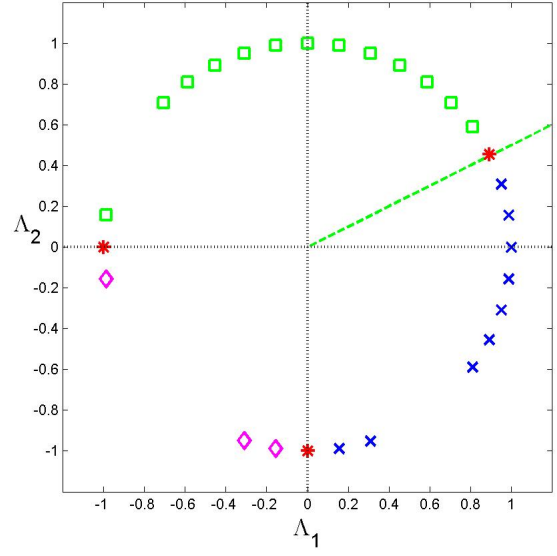


(d) $c_r = -3$

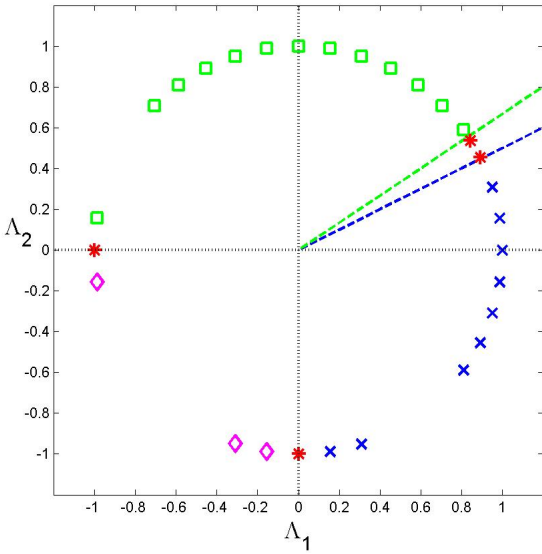
Figure 60: Numerically found behavior of solutions at $T = 200$ at $c_r \in \{-4.5, -4, -3.5, -3\}$ and $\phi \in \{n\pi/20, n = -10, \dots, 30\}$ and the theoretical bifurcation boundaries, where the blue half-line is the theoretical boundary for a stable steady oblique solution. The green half-line is the theoretical boundary for a stable normal traveling solution. The green squares are the numerically observed normal traveling behavior. The blue 'X's are the numerically observed steady oblique behavior. The magenta diamonds are where the steady state solution was observed numerically. The red asterisks are where mixed mode solutions were observed numerically.



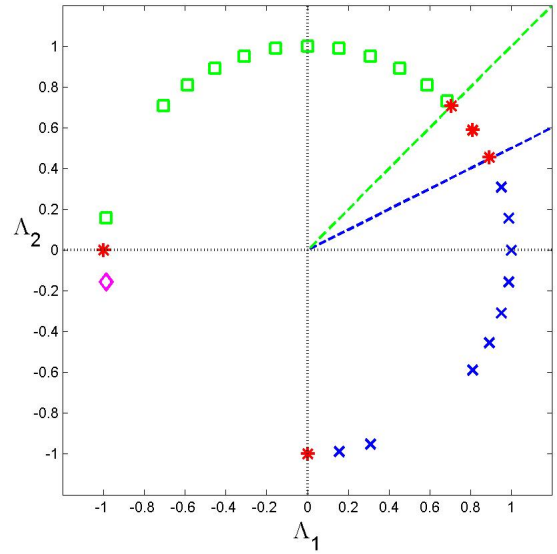
(a) $c_r = -2.5$



(b) $c_r = -2$

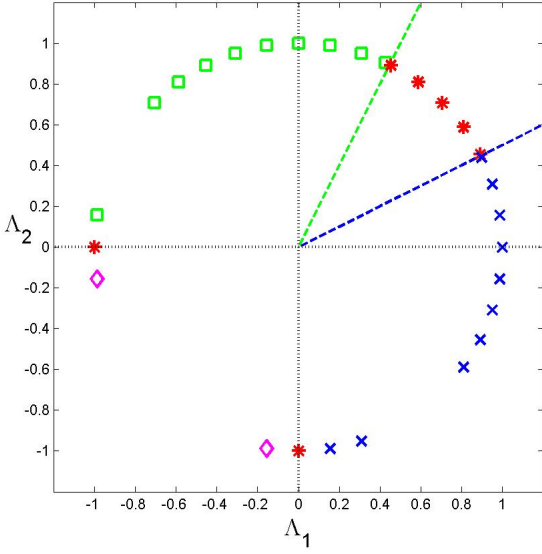


(c) $c_r = -1.5$

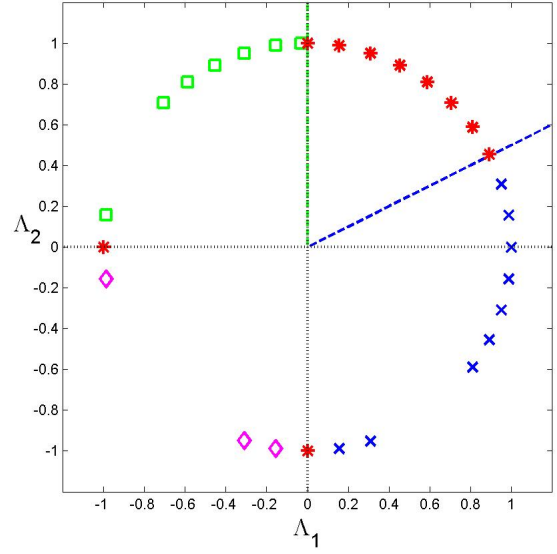


(d) $c_r = -1$

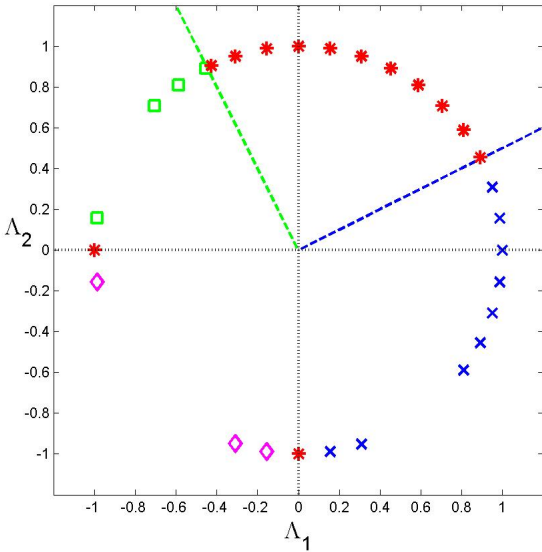
Figure 61: Numerically found behavior of solutions at $T = 200$ at $c_r \in \{-2.5, -2, -1.5, -1\}$ and $\phi \in \{n\pi/20, n = -10, \dots, 30\}$ and the theoretical bifurcation boundaries, where the blue half-line is the theoretical boundary for a stable steady oblique solution. The green half-line is the theoretical boundary for a stable normal traveling solution. The green squares are the numerically observed normal traveling behavior. The blue 'X's are the numerically observed steady oblique behavior. The magenta diamonds are where the steady state solution was observed numerically. The red asterisks are where mixed mode solutions were observed numerically.



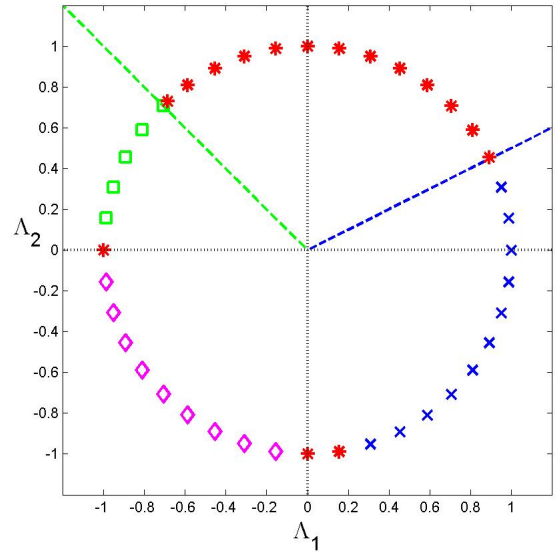
(a) $c_r = -0.5$



(b) $c_r = 0$

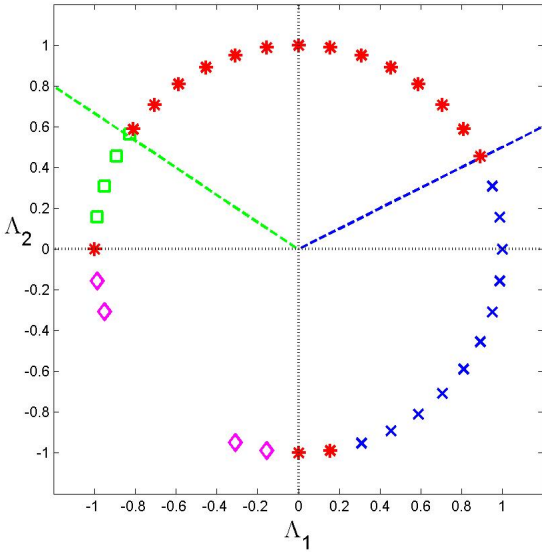


(c) $c_r = 0.5$

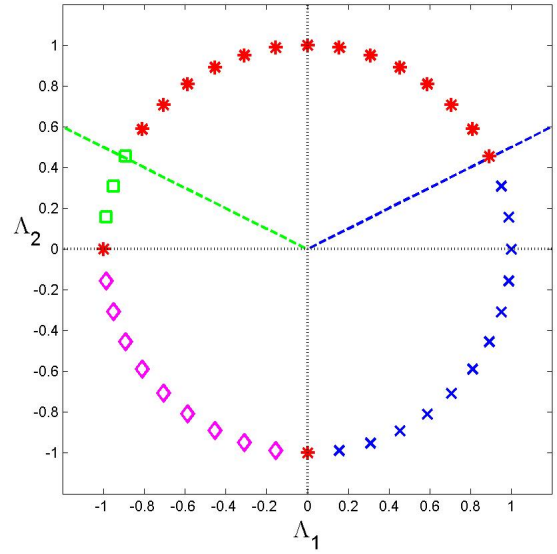


(d) $c_r = 1$

Figure 62: Numerically found behavior of solutions at $T = 200$ at $c_r \in \{-0.5, 0, 0.5, 1\}$ and $\phi \in \{n\pi/20, n = -10, \dots, 30\}$ and the theoretical bifurcation boundaries, where the blue half-line is the theoretical boundary for a stable steady oblique solution. The green half-line is the theoretical boundary for a stable normal traveling solution. The green squares are the numerically observed normal traveling behavior. The blue 'X's are the numerically observed steady oblique behavior. The magenta diamonds are where the steady state solution was observed numerically. The red asterisks are where mixed mode solutions were observed numerically.



(a) $c_r = 1.5$



(b) $c_r = 2$

Figure 63: Numerically found behavior of solutions at $T = 200$ at $c_r \in \{-2.5, -2, -1.5, -1\}$ and $\phi \in \{n\pi/20, n = -10, \dots, 30\}$ and the theoretical bifurcation boundaries, where the blue half-line is the theoretical boundary for a stable steady oblique solution. The green half-line is the theoretical boundary for a stable normal traveling solution. The green squares are the numerically observed normal traveling behavior. The blue 'X's are the numerically observed steady oblique behavior. The magenta diamonds are where the steady state solution was observed numerically. The red asterisks are where mixed mode solutions were observed numerically.

5 Conclusions and Further Work

A system of globally coupled Ginzburg Landau equations was set up to model the experimentally observed interaction of steady oblique rolls and normal traveling rolls which nematic electroconvection experiments have displayed near onset. From a qualitative theoretical study, the system of equations dictates the actions of slowly varying spatiotemporal envelopes of ideal roll patterns for anisotropic systems close to the experimentally observed codimension-two point. The equations predict steady and traveling, oblique and normal rolls and are experimentally supported as the “correct theoretical description governing the spatiotemporal dynamics of nematic electroconvection,” according to [1].

Through a normal form analysis of the globally coupled Ginzburg Landau equations the primary solution branches and their stability regions were found analytically. A region where the primary solutions interact (resulting in mixed mode solutions or bistability) was identified. The mixed mode solutions in this region of the (Λ_1, Λ_2) plane are either stable or unstable solutions of the normal form depending on the parameters b_{1r} , c_r , and d_r . When the mixed mode solutions are unstable, the analysis states that the region has bistability of the primary solutions (steady oblique rolls and normal traveling rolls).

When the mixed mode solution is stable in the normal form, we have numerically confirmed the presence of a continuous transition between the steady oblique rolls and the normal traveling rolls. Two regions of more complicated behavior were found near the bifurcation half-lines which define the region of stable mixed mode solutions. Near the (O) half-line (70), the solutions were a combination of either an A or B amplitude and both the C, D amplitudes. The three amplitudes involved in the patterns near the (N) half-line (73) were the A, B amplitudes and either a C or D amplitude. The effect of the initial conditions on the stable mixed mode region was not studied here.

The existence of the bistability region found analytically was also numerically confirmed. The parameters and the initial conditions appear to determine the ϕ at which the pattern

changes between steady oblique rolls and normal traveling rolls. The steady rectangles solutions and the standing wave solution were observed within this region only when similar initial conditions were used. Thus, further study is needed to determine the conditions under which these mixed mode solutions are stable.

Given the parameters, the normal form analysis predicted that the steady rectangles and standing wave solutions would be unstable. Stable steady rectangles, consisting of both of the steady oblique amplitudes, occurred at the bifurcation between the steady state region and the steady oblique region. At the bifurcation between the steady state solution and the normal traveling rolls is a mixed mode solution region where both of the normal traveling amplitudes are combined. Both of these regions appear to be transitional regions for the respective bifurcations from the steady state solution to either the steady oblique or the normal traveling solutions. A further study of these mixed mode solution regions is needed to identify the extent of the regions and other factors which contribute to this behavior.

One direct extension of the results found here would be expanding the numerical bifurcation diagram to $c_r > 2$ and $c_r < -4.5$. Another extension would be numerically finding the bifurcation diagrams in the (d_r, ϕ) and (b_{1r}, ϕ) planes and studying the results of variations of the parameters (c_r, d_r, b_{1r}, ϕ) .

References

- [1] G. Acharya, G. Dangelmayr, J.T. Gleeson, and I. Oprea. Steady state-Hopf mode interactions at the onset of electroconvection in the nematic liquid crystal Phase V. *International Journal of Molecular Sciences*, 12:4488–4503, 2011.
- [2] G. Ahlers. Experiments with Rayleigh-Bénard convection. In I. Mutabazi, J. Wesfreid, and E. Guyon, editors, *Dynamics of Spatio-Temporal Cellular Structures*, volume 207, pages 67–94. Springer, 2006.
- [3] Robert Almgren. Numerical methods for PDEs. Technical report, University of Toronto, 2003.
- [4] U. Behn and W. Pesch. Electrohydrodynamic convection in nematics. In F.H. Busse and S. Müller, editors, *Evolution of Spontaneous Structures in Dissipative Continuous Systems*, pages 335–383. Springer-Verlang, Berlin, 1998.
- [5] A. Buka, N. Éber, and W. Pesch. Convective patterns in liquid crystals driven by electric field. *Liquid Crystal Commun*, 60:1–21, 2005.
- [6] S. Chandrasekhar. *Liquid Crystals*. University Press, Cambridge, 1977.
- [7] S. Chandrasekhar. *Hydrodynamic and Hydromagnetic Stability*. Dover Publications, 1981.
- [8] P. Chossat and G. Iooss. *The Couette-Taylor Problem*. Springer-Verlag, New York, 1994.
- [9] P. Chossat and R. Lauterbach. *Methods in Equivariant Bifurcations and Dynamical Systems*. World Scientific, 2000.
- [10] M. Cross and P. C. Hohenberg. Pattern formation outside equilibrium. *Rev. Mod. Phys.*, 65:851–1123, 1993.

- [11] G. Dangelmayr. Steady-state mode interactions in the presence of $O(2)$ -symmetry. *Dynamics and Stability of Systems*, 1(2):159–185, 1986.
- [12] G. Dangelmayr, G. Acharya, J. T. Gleeson, I. Oprea, and J. Ladd. Diagnosis of spatiotemporal chaos in wave envelopes of a nematic electroconvection pattern. *Physical Review E*, 79:046215, 2009.
- [13] G. Dangelmayr and I. Oprea. A bifurcation study of wave patterns for electroconvection in nematic liquid crystals. *Mol. Cryst. Liq. Cryst*, 413:2441, 2004.
- [14] G. Dangelmayr and I. Oprea. Modulational stability of traveling waves in 2d anisotropic systems. *J. Nonlinear Sci.*, 18:1–56, 2008.
- [15] G. Dangelmayr and M. Wegelin. Hopf bifurcations in anisotropic systems. In M. Golubitsky, D. Luss, and S. Strogatz, editors, *Pattern Formation in Continuous and Coupled Systems*, pages 33–48. Springer, IMA Vol. in Math. and Appl. 115, 1999.
- [16] J.H.P. Dawes. A Hopf/steady-state mode interaction in rotating convection: bursts and heteroclinic cycles in a square periodic domain. *Physica D*, 149:197–209, 2001.
- [17] M. Dennin, G. Ahlers, and D.S. Cannell. Spatiotemporal chaos in electroconvection. *Science*, 272:388, 1996.
- [18] M. Dennin, D.S. Canel, and G. Ahlers. Patterns in electroconvection in the nematic liquid crystal I52. *Mollec. Cryst. Liq. Cryst.*, 261:337, 1995.
- [19] M. Dennin, D.S. Cannell, and G. Ahlers. Patterns of electroconvection in a nematic liquid crystal. *Physical Review E*, 57:638–649, 1998.
- [20] Steven Fauve. *Pattern Forming Instabilities*. Cambridge University Press, 1998.
- [21] K. Fujimura and Y. Renardy. The 2:1 steady/Hopf mode interaction in the two-layer Bénard problem. *Physica D*, 85:25, 1995.

- [22] M. Golubitsky and I. Stewart. *The Symmetry Perspective: From equilibrium to chaos in phase space and physical space*. Berkhauser Verlag, Boston, 2000.
- [23] M. Golubitsky, I. Stewart, and D.G. Schaeffer. *Singularities and Groups in Bifurcation Theory II*. Springer, New York, 1988.
- [24] P. Guba and M. Grae Worster. Interactions between steady and oscillatory convection in mushy layers. *J. Fluid Mech*, 645:411, 2010.
- [25] M. Higuera, H. Riecke, and M. Silber. Near-resonant steady mode interactions: Periodic, quasi-periodic, and localized patterns. *SIAM J. Applied Dynamical Systems*, 3(4):463–502, 2004.
- [26] Y. Hu, R.E. Ecke, and G. Ahlers. Time and length scales in rotating Rayleigh-Bénard convection. *Physical Review Letters*, 74:5040–5043, 1995.
- [27] E. Knobloch and J. DeLuca. Amplitude equations for traveling wave convection. *Nonlinearity*, 3:975–980, 1990.
- [28] L. Kramer and W. Pesch. Convection instabilities in nematic liquid crystals. In T. Vogt-mann H. Hoffmann, M. Schwoerer, editor, *Macromolecular Systems: Microscopic Interactions and Macroscopic Properties*, pages 250–294. Wiley, 2000.
- [29] J. Ladd. Heteroclinic cycles in an eight dimensional vector field derived from nematic electroconvection. Master’s thesis, Colorado State University, 2004.
- [30] S.W. Morris, E. Bodenschatz, D.S. Cannell, and G. Ahlers. Sprial defect chaos in large aspect ratio Rayleigh-Bénard convection. *Physical Review Letters*, 71:2026–2029, 1993.
- [31] I.V. Morshneva and S.N. Ovchinnikova. Resonance regimes in the neighborhood of bifurcation points of codimension 2 in the Couette-Taylor problem. *Fluid Dynamics*, 44:813–822, 2009.

- [32] I. Oprea and G. Dangelmayr. Dynamics and bifurcations in the weak electrolyte model for electroconvection of nematic liquid crystals: a Ginzburg-Landau approach. *European Journal of Mechanics B/Fluids*, 2008.
- [33] I. Oprea, I. Triandaf, D. Dangelmayr, and I. Schwartz. Quantitative and qualitative characterization of zigzag spatiotemporal chaos in a system of amplitude equations for nematic electroconvection. *Chaos*, 17:Note(s): 023101.1–023101.12, 2007.
- [34] S.N. Ovchinnikova and I.V. Morshneva. A numerical study of resonant regimes near the points of codimension-2 bifurcation in the Couette-Taylor problem, 2007.
- [35] S. Rasnet, G. Hartung, B.L. Winkler, and I. Rehberg. The shadowgraph method in convection experiments. *Experiments in Fluids*, 7:412, 1989.
- [36] M. Renardy, Y. Renardy, R. Sureshkumar, and A.N. Beris. Hopf-Hopf and steady-Hopf mode interactions in Taylor-Couette flow of an upper convected maxwell liquid. *J. Non-Newtonian Fluid Mech.*, 63:1–31, 1996.
- [37] D. Ruelle. Bifurcations in the presence of a symmetry group. *Arch. Rat. Anal.*, 51:136, 1973.
- [38] M. Silber, H. Riecke, and L. Kramer. Symmetry breaking Hopf bifurcation in anisotropic systems. *Physica D*, 61:260, 1992.
- [39] S.H. Strogatz. *Nonlinear Dynamics and Chaos*. Westview, Cambridge, MA, 1994.
- [40] M. Treiber and L. Kramer. Coupled complex Ginzburg-Landau equations for the weak electrolyte model of electroconvection. *Physical Review E*, 58:1973, 1998.
- [41] A.M. Turing. The chemical basis of morphogenesis. *Philosophical Transactions of the Royal Society of London. Series B, Biological Sciences*, 237:37–72, 1952.
- [42] M. Wegelin. *Nichtlineare Dynamik raumzeitlicher Muster in hierarchischen Systemen*. PhD thesis, University of Tübingen, Department of Physics, 1993.

- [43] T. Wildey. A pseudospectral method for the globally coupled Ginzburg Landau equations in 2d. Master's thesis, Colorado State University, 2004.
- [44] Yisong Yang. Convergence of the pseudospectral method for the Ginzburg-Landau equation. *Journal of Mathematical Analysis and Applications*, 147:556–568, 1990.

Appendix A Coutte-Taylor Example

For the interaction of an axisymmetric and a nonaxisymmetric mode, at criticality there needs to be one eigenvalue at zero and a pair $\pm i\omega_0$ on the imaginary axis [8]. The procedure of center manifold reduction and normal form transformation [8] allows the reduction of the original PDEs (1) to a system of normal form differential equations for the coordinates in the center eigenspace, which is six dimensional since the eigenvalues are doubled. The normal form is equivariant under the action of the group $\Gamma = O(2) \times SO(2)$ restricted to the center eigenspace, where $O(2)$ is generated by translations $\mathcal{T}_\psi : z \rightarrow z + \psi$ and the reflection $\mathcal{S} : z \rightarrow -z$, and $SO(2)$ is generated by rotations $\mathcal{R}_\varphi : \theta \rightarrow \theta + \varphi$ of the cylindrical coordinates (r, θ, z) . Let the zero eigenvalue have eigenvectors ζ_0 and $\bar{\zeta}_0$ and the eigenvalue $i\omega_0$ have eigenvectors ζ_1 and ζ_2 , such that $\zeta_2 = \mathcal{S}\zeta_1$. The group Γ acts on ζ_0 via the operations

$$\mathcal{T}_\psi \zeta = e^{in\psi} \zeta, \quad \mathcal{S} \zeta = \bar{\zeta}, \quad \mathcal{R}_\varphi \zeta = \zeta \quad \forall \psi \text{ and } \varphi \in \mathbb{R}, \quad (102)$$

and on ζ_1 and ζ_2 according to the matrix operations

$$\mathcal{T}_\psi = \begin{pmatrix} e^{in\psi} & 0 \\ 0 & e^{-in\psi} \end{pmatrix}, \quad \mathcal{S} = \begin{pmatrix} 0 & 1 \\ 1 & 0 \end{pmatrix}, \quad \mathcal{R}_\varphi = e^{i\varphi} \begin{pmatrix} 1 & 0 \\ 0 & 1 \end{pmatrix}. \quad (103)$$

Let elements in the eigenspace, \mathcal{V} , be written as

$$X = \sum_{j=0}^2 A_j \zeta_j + \bar{A}_j \bar{\zeta}_j. \quad (104)$$

Thus the group Γ acts on the coordinates according to

$$\begin{aligned}
\mathcal{T}_\psi A_j &= e^{im\psi} A_j \quad (j = 0, 1) \quad \text{and} \quad \mathcal{T}_\psi A_2 = e^{-im\psi} A_2, \\
A_2 &= \mathcal{S}A_1 \quad \text{and} \quad \bar{A}_0 = \mathcal{S}A_0, \\
\mathcal{R}_\varphi A_j &= e^{ij\varphi} A_j \quad (j = 0, 1) \quad \text{and} \quad \mathcal{R}_\varphi A_2 = e^{i\varphi} A_2.
\end{aligned} \tag{105}$$

Next, the structure of the Γ -equivariant maps in \mathcal{V} need to be computed. Let the difference between the Reynolds number, \mathbf{R} , and the critical Reynolds number, \mathbf{R}_c , be denoted as $\mu = \mathbf{R} - \mathbf{R}_c$, $\nu = \Omega - \Omega^{(0)}$, and

$$F(\mu, \nu, X) = \sum_{j=0}^2 F_j(\mu, \nu, X) \zeta_j + \overline{F_j(\mu, \nu, X)} \bar{\zeta}_j. \tag{106}$$

Thus the amplitude equations are

$$\frac{dA_j}{dt} = F_j(\mu, \nu, X) \quad (j = 0, 1, 2). \tag{107}$$

The F_j 's have the relations

$$\begin{aligned}
F_0(\mu, \nu, \mathcal{R}_\varphi X) &= F_0(\mu, \nu, X), \\
F_0(\mu, \nu, \mathcal{T}_\psi X) &= e^{im\psi} F_0(\mu, \nu, X), \\
F_0(\mu, \nu, \mathcal{S}X) &= \overline{F_0(\mu, \nu, X)}, \\
F_1(\mu, \nu, \mathcal{R}_\varphi X) &= e^{i\varphi} F_1(\mu, \nu, X), \\
F_1(\mu, \nu, \mathcal{T}_\psi X) &= e^{im\psi} F_1(\mu, \nu, X), \\
F_2(\mu, \nu, X) &= F_0(\mu, \nu, \mathcal{S}X)
\end{aligned} \tag{108}$$

through the equations (105). Therefore, to write the differential system in \mathcal{V} in terms of coordinates the following lemma is helpful.

Lemma 1 *Any polynomial map $F(X)$ satisfying the relations (108) has the following structure: let us set $A_j = \rho_j e^{i\psi_j}$, $u_j = \rho_j^2$, and $v = A_0^2 \bar{A}_1 A_2$. Then*

$$\begin{aligned} F_0 &= A_0 g_0(u_0, u_1, u_2, v) + \bar{A}_0 A_1 \bar{A}_2 h_0(u_0, u_1, u_2, \bar{v}), \\ F_1 &= A_1 g_1(u_0, u_1, u_2, \bar{v}) + A_0^2 A_2 h_1(u_0, u_1, u_2, v), \\ F_2 &= A_2 g_1(u_0, u_2, u_1, v) + \bar{A}_0^2 A_1 h_1(u_0, u_2, u_1, \bar{v}), \end{aligned} \quad (109)$$

where g_j and h_j are complex polynomials and g_0, h_0 satisfy the relation $f(x, y, z, \bar{t}) = \overline{f(x, y, z, t)}$.

By expanding $F(\mu, \nu, X)$ in a Taylor series helps rewrite the differential system in \mathcal{V} in terms of coordinates resulting in

$$\begin{aligned} \frac{dA_0}{dt} &= A_0(\alpha_0 \mu + \beta_0 \nu + c_0 \rho_0^2 + d_0 \rho_1^2 + \bar{d}_0 \rho_2^2) + f_0 \bar{A}_0 A_1 \bar{A}_2 + h.o.t., \\ \frac{dA_1}{dt} &= A_1(i\omega_0 + \alpha_1 \mu + \beta_1 \nu + c_1 \rho_0^2 + d_1 \rho_1^2 + e_1 \rho_2^2) + f_1 A_0^2 A_2 + h.o.t., \\ \frac{dA_2}{dt} &= A_2(i\omega_0 + \alpha_1 \mu + \beta_1 \nu + c_1 \rho_0^2 + e_1 \rho_1^2 + d_1 \rho_2^2) + f_1 \bar{A}_0^2 A_1 + h.o.t., \end{aligned} \quad (110)$$

with $\alpha_0, \beta_0, c_0, f_0 \in \mathbb{R}$. However, while equations (110) are useful, they can be rewritten in a global way which takes into account all orders according to the following lemma.

Lemma 2 *The six dimensional vector field satisfying relations (108) can be written as*

$$\frac{dA_j}{dt} = e^{i\psi_j} f_j(\mu, \nu, \rho_0, \rho_1, \rho_2, \theta), \quad j = 0, 1, 2, \quad (111)$$

where $A_j = \rho_j e^{i\psi_j}$, f_j are 2π -periodic in $\theta = 2\psi_0 - \psi_1 + \psi_2$, and f_0 is odd in ρ_0 , even in (ρ_1, ρ_2) , while f_1 and f_2 are even in ρ_0 , odd in (ρ_1, ρ_2) . Moreover,

$$\begin{aligned} f_0(\mu, \nu, \rho_0, \rho_2, \rho_1, -\theta) &= \bar{f}_0(\mu, \nu, \rho_0, \rho_1, \rho_2, \theta), \\ f_2(\mu, \nu, \rho_0, \rho_2, \rho_1, -\theta) &= f_1(\mu, \nu, \rho_0, \rho_1, \rho_2, \theta) \end{aligned} \quad (112)$$

and if one of the ρ_j 's is 0, then f_k is independent of θ and odd in ρ_k , even in ρ_l for $k \neq j$, $l \neq j$, $k \neq l$.

Due to the symmetry of the problem, there are subspaces that are invariant under the vector field F and therefore under the equations (107). Due to the equivariance of F , if such a subspace is transformed by the action of an element γ of the group Γ , then the resulting subspace is also invariant under the system. Also, any trajectory is isometrically transformed by γ to another trajectory. Thus, one only needs to know one representative of each equivalence class of the flow-invariant subspaces [8]. The invariant subspaces in the following lemma.

Lemma 3 *For any $\psi \in \mathbb{T}^1$ the following subspaces of \mathcal{V} are invariant under the system (107):*

$$(i) \ e^{i\psi} A_0 \ (A_0 \in \mathbb{R}), \ A_1 = A_2 = 0;$$

$$(ii) \ A_0 = A_2 = 0;$$

$$(iii) \ A_0 = A_1 = 0;$$

$$(iv) \ A_0 = 0, \ A_2 = e^{i\psi} A_1;$$

$$(v) \ A_0 = 0, \ A_1 A_2 \neq 0;$$

$$(vi) \ e^{i\psi} A_0 \ (A_0 \in \mathbb{R}), \ A_1 = -e^{2i\psi} A_2;$$

$$(vii) \ e^{i\psi} A_0 \ (A_0 \in \mathbb{R}), \ A_1 = e^{2i\psi} A_2.$$

Subspaces (i), (ii), and (iii) from Lemma 3 are the lowest dimensional, nontrivial subspaces which correspond to pure mode solutions (only pure stationary or pure Hopf bifurcations). The Taylor vortices are found in subspace (i). In subspace (ii), spiral flow is found. Through the actions of \mathcal{S} , the symmetric solutions to that found in subspace (ii) are found in subspace (iii). The ribbons are found in subspace (iv). In subspace (v), both spiral flow and ribbons are found [8].

From Lemma 1 (or Lemma 2) and system (110), the principal part of the differential system in the subspace (vi) of Lemma 3 is

$$\frac{dA_0}{dt} = A_0 [\alpha_0\mu + \beta_0\nu + c_0\rho_0^2 + (2d_{0r} - f_0)\rho_1^2 + O(|\mu| + |\nu| + \rho_0^2 + \rho_1^2)^2], \quad (113)$$

$$\begin{aligned} \frac{dA_1}{dt} &= A_1 [i\omega_0 + \alpha_1\mu + \beta_1\nu + (c_1 - f_1)\rho_0^2 + (d_1 + e_1)\rho_1^2 \\ &\quad + O(|\mu| + |\nu| + \rho_0^2 + \rho_1^2)^2], \end{aligned} \quad (114)$$

with an the equation for A_2 being similar to (114). This system decouples into phase and modulus equations and the equations for the moduli take the form

$$\begin{aligned} \frac{d\rho_0}{dt} &= \rho_0 [\alpha_0\mu + \beta_0\nu + c_0\rho_0^2 + (2d_{0r} - f_0)\rho_1^2 + O(|\mu| + |\nu| + \rho_0^2 + \rho_1^2)^2], \\ \frac{d\rho_1}{dt} &= \rho_1 [\alpha_{1r}\mu + \beta_{1r}\nu + (c_{1r} - f_{1r})\rho_0^2 + (d_{1r} + e_{1r})\rho_1^2 \\ &\quad + O(|\mu| + |\nu| + \rho_0^2 + \rho_1^2)^2]. \end{aligned} \quad (115)$$

There are three cases for equilibria of the moduli system:

- (i) $A_1 = 0$, which shows Taylor vortices;
- (ii) $A_0 = 0$, which shows ribbons; and
- (iii) $A_1 A_0 \neq 0$, which simplifies the principal part of the system to be

$$\begin{aligned} \alpha_0\mu + \beta_0\nu + c_0\rho_0^2 + (2d_{0r} - f_0)\rho_1^2 &= 0 \\ \alpha_{1r}\mu + \beta_{1r}\nu + (c_{1r} - f_{1r})\rho_0^2 + (d_{1r} + e_{1r})\rho_1^2 &= 0. \end{aligned} \quad (116)$$

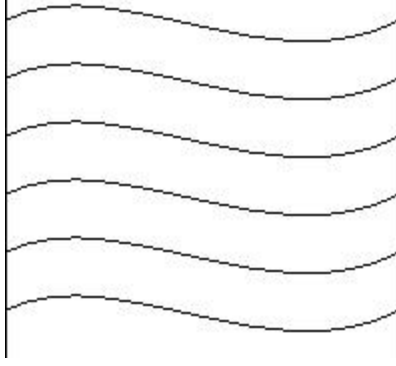


Figure 64: Wavy vortex flow.

Continuing with the third case, let $D = c_0(d_{1r} + e_{1r}) - (2d_{0r} - f_0)(c_{1r} - f_{1r})$. For $D \neq 0$, nontrivial solutions of the system (116) exist and the leading terms of the branch are

$$\begin{aligned}\rho_0^2 &= \frac{\alpha_{1r}(2d_{0r} - f_0) - \alpha_0(d_{1r} + e_{1r})}{D}\mu + \frac{\beta_{1r}(2d_{0r} - f_0) - \beta_0(d_{1r} + e_{1r})}{D}\nu, \\ \rho_1^2 &= \frac{\alpha_0(c_{1r} - f_{1r}) - \alpha_{1r}c_0}{D}\mu + \frac{\beta_0(c_{1r} - f_{1r}) - \beta_{1r}c_0}{D}\nu.\end{aligned}\quad (117)$$

The corresponding wavy vortex flow solutions of (113)-(114) is a mix of the stationary and time-periodic modes and are rotating waves, depicted in Figure 64 [8].

In subspace (vii), similar to that of subspace (vi), the principal part of the system becomes

$$\begin{aligned}\frac{dA_0}{dt} &= A_0 [\alpha_0\mu + \beta_0\nu + c_0\rho_0^2 + (2d_{0r} + f_0)\rho_1^2 + O(|\mu| + |\nu| + \rho_0^2 + \rho_1^2)^2], \\ \frac{dA_1}{dt} &= A_1 [i\omega_0 + \alpha_1\mu + \beta_1\nu + (c_1 + f_1)\rho_0^2 + (d_1 + e_1)\rho_1^2 \\ &\quad + O(|\mu| + |\nu| + \rho_0^2 + \rho_1^2)^2],\end{aligned}\quad (118)$$

with the equation for A_2 being similar to (119). Eliminating the primary solutions, Taylor vortices and ribbons, leaves the mixed mode branch. On this branch, the solution of the amplitude equations for the equilibria gives

$$\begin{aligned}\rho_0^2 &= \frac{\alpha_{1r}(2d_{0r} + f_0) - \alpha_0(d_{1r} + e_{1r})}{D}\mu + \frac{\beta_{1r}(2d_{0r} + f_0) - \beta_0(d_{1r} + e_{1r})}{D}\nu, \\ \rho_1^2 &= \frac{\alpha_0(c_{1r} + f_{1r}) - \alpha_{1r}c_0}{D}\mu + \frac{\beta_0(c_{1r} + f_{1r}) - \beta_{1r}c_0}{D}\nu.\end{aligned}\quad (120)$$

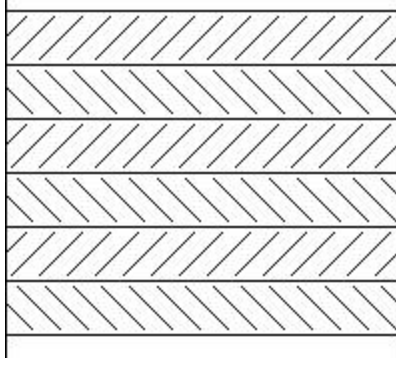


Figure 65: Twisted vortices.

with $D = c_0(d_{1r} + e_{1r}) - (2d_{0r} + f_0)(c_{1r} + f_{1r})$. The twisted vortices solutions, depicted in Figure 65, are rotating waves which have a “2-torus group orbit by rotations (or time evolution) and translations” [8].